Theses and Dissertations--Mechanical Engineering

Mechanical Engineering

2022

IN-SITU CHARACTERIZATION OF SURFACE QUALITY IN **γ**-TiAl AEROSPACE ALLOY MACHINING

David Adeniji
University of Kentucky, doad224@uky.edu
Author ORCID Identifier:
 https://orcid.org/0000-0002-5110-7276
Digital Object Identifier: https://doi.org/10.13023/etd.2022.112

Right click to open a feedback form in a new tab to let us know how this document benefits you.

STUDENT AGREEMENT:

I represent that my thesis or dissertation and abstract are my original work. Proper attribution has been given to all outside sources. I understand that I am solely responsible for obtaining any needed copyright permissions. I have obtained needed written permission statement(s) from the owner(s) of each third-party copyrighted matter to be included in my work, allowing electronic distribution (if such use is not permitted by the fair use doctrine) which will be submitted to UKnowledge as Additional File.

I hereby grant to The University of Kentucky and its agents the irrevocable, non-exclusive, and royalty-free license to archive and make accessible my work in whole or in part in all forms of media, now or hereafter known. I agree that the document mentioned above may be made available immediately for worldwide access unless an embargo applies.

I retain all other ownership rights to the copyright of my work. I also retain the right to use in future works (such as articles or books) all or part of my work. I understand that I am free to register the copyright to my work.

REVIEW, APPROVAL AND ACCEPTANCE

The document mentioned above has been reviewed and accepted by the student's advisor, on behalf of the advisory committee, and by the Director of Graduate Studies (DGS), on behalf of the program; we verify that this is the final, approved version of the student's thesis including all changes required by the advisory committee. The undersigned agree to abide by the statements above.

David Adeniji, Student

Dr. J. M. Schoop, Major Professor

Dr. J. B. Hoagg, Director of Graduate Studies

IN-SITU CHARACTERIZATION OF SURFACE QUALITY IN γ-*TiAl* AEROSPACE
ALLOY MACHINING

––––––––––––––––––––––––––––––

DISSERTATION

––––––––––––––––––––––––––––––

A dissertation submitted in partial fulfillment of the
requirements for the degree of Doctor of Philosophy in the
College of Engineering at the University of Kentucky

By

David Omotayo Adeniji

Lexington, Kentucky

Co-Directors: Dr. J. M. Schoop, Professor of Mechanical Engineering and

Dr. I. S. Jawahir, Professor of Mechanical Engineering

Lexington, Kentucky

2022

ABSTRACT OF DISSERTATION

IN-SITU CHARACTERIZATION OF SURFACE QUALITY IN γ-*TiAl* AEROSPACE ALLOY MACHINING

The functional performance of critical aerospace components such as low-pressure turbine blades is highly dependent on both the material property and machining induced surface integrity. Many resources have been invested in developing novel metallic, ceramic, and composite materials, such as gamma-titanium aluminide (γ-*TiAl*), capable of improved product and process performance. However, while γ-*TiAl* is known for its excellent performance in high-temperature operating environments, it lacks the manufacturing science necessary to process them efficiently under manufacturing-specific thermomechanical regimes. Current finish machining efforts have resulted in poor surface integrity of the machined component with defects such as surface cracks, deformed lamellae, and strain hardening.

This study adopted a novel in-situ high-speed characterization testbed to investigate the finish machining of titanium aluminide alloys under a dry cutting condition to address these challenges. The research findings provided insight into material response, good cutting parameter boundaries, process physics, crack initiation, and crack propagation mechanism. The workpiece sub-surface deformations were observed using a high-speed camera and optical microscope setup, providing insights into chip formation and surface morphology. Post-mortem analysis of the surface cracking modes and fracture depths estimation were recorded with the use of an upright microscope and scanning white light interferometry,

In addition, a non-destructive evaluation (NDE) quality monitoring technique based on acoustic emission (AE) signals, wavelet transform, and deep neural networks (DNN) was developed to achieve a real-time total volume crack monitoring capability. This approach showed good classification accuracy of 80.83% using scalogram images, in-situ experimental data, and a VGG-19 pre-trained neural network, thereby establishing the significant potential for real-time quality monitoring in manufacturing processes.

The findings from this present study set the tone for creating a digital process twin (DPT) framework capable of obtaining more aggressive yet reliable manufacturing parameters and monitoring techniques for processing turbine alloys and improving industry manufacturing performance and energy efficiency.

KEYWORDS: Machining, Characterization, In-situ, Titanium Aluminide, Surface Integrity, NDE

David Omotayo Adeniji

May, 6th, 2022

IN-SITU CHARACTERIZATION OF SURFACE QUALITY IN γ-*TiAl* AEROSPACE
ALLOY MACHINING

By

David Omotayo Adeniji

Dr. J.M. Schoop
Co-Director of Dissertation

Dr. I. S. Jawahir
Co-Director of Dissertation

Dr. J. B. Hoagg
Director of Graduate Studies

May, 6th, 2022

DEDICATION

To the memories of my late guardian, Prince E.K. Olurebi. I am forever grateful for your counsel, love, and selflessness.

ACKNOWLEDGMENTS

Thanks be to God for using my years in graduate school to further the salvation of my soul and for leading me on the path of life.

First, I would like to express my sincere gratitude to my advisor, Dr. Julius Schoop, for his guidance, mentorship, and support throughout my graduate program. I vividly remember the first day I walked into your office and how eager you were to have me join your group. I have received nothing short of this support ever since and have seen you extend the same to every student. I have learned from your unparalleled work ethic and multi-disciplinary expertise demonstrated during the initial laboratory setup and the development of the novel in-situ characterization testbed. I cannot forget how you, Ian, and I would climb on the granite plate to drill holes in it. Thank you for the mentorship and opportunity to go for my 2021 summer internship at Intel Corporation. This dissertation would not have been possible without you. It is an honor to have you as my advisor and mentor.

I appreciate the support and guidance from Dr. I.S Jawahir on my research and graduate studies. You are an exemplary role model to both students and faculty, and your achievements speak for themselves any day. It is a privilege to be trained by you and to have you as my Ph.D. co-director. Thank you to Dr. Nathan Jacobs for agreeing to be part of my committee. I was impressed with your knowledge in machine learning and how you managed to blend both theoretical and practical approaches in your CS460G class, which is perhaps the best graduate class I have taken. Also, I appreciate Dr. Scott Stephens and Dr. David Murrugarra for their support and for serving on my committee.

I want to thank all my group members; Ian Brown, Shehan Gunawardena, Guher Toker, E-Lexus Thornton (my roommate), Mehedi Hassan, Avery Hartley, Hamzah Zannoun, and Dan Caudil. Also, special thanks to Charles Adams for his support in running experiments in the machining laboratory. My gratitude goes to the U.S. Department of Energy's Office of Energy Efficiency and Renewable Energy (EERE) under the 2020 Advanced Manufacturing Office's (AMO) Award DE-FOA-0001980 for funding my research.

CHAPTER 1.

INTRODUCTION

1.1 MOTIVATION AND SIGNIFICANCE

Turbines are widely used in the energy and transportation sectors, accounting for 15.7 quadrillion BTUs of annual energy consumption, which is approximately $370 billion in fuel cost alone. According to the U.S. Energy Information Administration, this figure represents 16.1% of the total energy consumed in the U.S., which is 43% larger than all renewable energy within the current energy portfolio (Ghosh et al., 1998). As a result, there is significant interest in realizing even slight improvements in the efficiency of turbines, including platforms for power generation and jet engines for transportation. OEMs invest significant resources to improve turbine performance with new metallic, ceramic, and composite turbine materials. These novel materials, such as advanced nickel-based superalloys and gamma-titanium-aluminide (γ-*TiAl*), are capable of operating at increasingly higher temperatures, which allows for more efficient turbine operation. However, while there have been tremendous advances in the Materials Science of turbine materials that operate at elevated temperatures and extreme loading conditions, the Manufacturing Science necessary to process them efficiently under manufacturing-specific thermomechanical regimes has been lacking (credit: Prof. J. Schoop, 2019).

A significant percentage of aerospace components are manufactured using at least one conventional metal machining operation. Reports showed that 5% of annual gross domestic product across developing nations is due to machining expenditure, resulting in a global financial impact of more than 250 billion USD (Arrazola et al., 2013). Machining operations are expected to manufacture products at a reduced cost, required tolerance, surface finish, and quality standards across different industrial sectors, especially in a critical space such as the aerospace industry. Machining is typically done in two steps with varied cutting parameters, yielding varying outcomes. Roughing, typically the first step is followed by a second step known as finishing or precision machining. Roughing operations in machining are primarily used to remove bulk material and roughly shape the workpiece to the desired shape, making subsequent processing more convenient and efficient. The

objective of rough machining is to remove the blank allowance as rapidly as possible. A high feed rate and cutting depth are usually chosen to remove as many chips as feasible in a short period. As a result, rough machined components frequently have low precision, a rough surface, and high productivity. This work is focused on finishing passes or precision machining since this step is responsible for the final surface integrity of the machined component.

Much research has gone into machining process predictive models; however, industrial practices remain empirical and anecdotal due to the lack of efficient and reliable analytical or numerical models. Current industry practice for improving turbine component manufacturing processes is fundamentally empirical, primarily due to a lack of efficient and reliable models to predict the complex interactions between process parameters (feeds, speeds, tool condition) and process-induced structure (surface integrity, e.g., residual stresses and near-surface microstructure), and the resultant process performance (energy efficiency, productivity/profitability). While significant advances have been made to promote model-based Integrated Computational Materials Engineering (ICME) in alloy design, as well as in primary and secondary processing, there are currently no industrially-viable models for predicting the process-induced surface integrity, which significantly affects overall functional performance and life-cycle embodied energy of components operating in harsh service conditions (e.g., turbine components). Also, considering the complex nature of machining processes and the critical dependence of reliable predictive models on realistic inputs, the development of accurate and robust models would undoubtedly hinge on a proper understanding of process physics and a realistic characterization of model inputs.

Accurate characterization of the process physics and mechanics governing machining processes is a fundamental topic many researchers have investigated. Characterizing chip formation processes, surface integrity evolution, and tool/chip/workpiece interactions is crucial to developing, calibrating, and validating robust process models and implementing effective process control measures. Moreover, a closer interweaving of advanced experimental techniques, such as high-speed in-situ microscopy and digital image correlation analysis, with advanced analytical and numerical process simulations is envisioned as a significant steppingstone towards faster, more reliable, and

more industrially-applicable process models. Early efforts toward so-called in-situ characterization of machining processes can be dated to Schwerd (1935), who was among the first to study the process of chip formation during cutting. Subsequently, Stevenson and Oxley (1969) adopted more advanced characterization techniques, such as explosive quick stop device setup. The deformation to the square grids printed on the workpiece was observed after an abrupt process stop. However, most of these approaches did rely on significant post-processing and an oversimplified assumption of instantaneous 'freezing' of a steady-state deformation, as Childs (1971) later established. Since achieving an efficient and realistic process or material, characterization is critical for developing (and calibrating) robust and accurate process models; several publications have been on this topic, including (2015; 2018; Lee et al.). Most efforts in the in-situ study of machining processes have been constrained to a low cutting speed range (~5 mm/s) and high chip thickness (~0.5mm) due to imaging and experimental setup limitations however, this is not representative of a typical machining process and industrially-relevant finish machining parameters (~2 m/s speed, ~microns uncut chip thickness).

More recently, (Schoop et al., 2019) developed a state-of-the-art high-speed in-situ characterization testbed consisting of a custom video microscope with coaxial illumination and a custom-built LED liquid light guide-fed light source (patents: (Schoop, 2020a; Schoop, 2020b)). This setup is capable of sub-surface material deformation characterization at a high cutting speed of up to 250 m/min cutting speed, micron-level chip thickness, and camera frame rate of about 2,000,000 fps. As highlighted by (Schoop et al., 2019) and several authors (Arriola et al., 2011; Efe et al., 2012; Guo et al., 2015; Guo et al., 2012; Lee et al., 2006) the development of such a novel characterization testbed would help better understand process physics, drive the development of robust and computationally efficient predictive models and ultimately help in establishing a digital twin for machining processes.

1.2 CASE STUDY FOR TITANIUM ALUMINIDE TURBINE ALLOYS AND PROJECT SCOPE

Titanium intermetallic alloys are currently gaining ground in the aerospace and automotive industry due to their lightweight, suitability for high-temperature applications, good oxidation, and creep resistance (Lapin, 2009). For instance, $\gamma - TiAl$ alloys feature a

highly ordered structure which is responsible for their unique physical and mechanical properties: high melting point, low density, high strength, resistance to oxidation, and corrosion. Compared to other aerospace alloys such as conventional titanium, steel, and nickel, γ-*TiAl*'s low density offers an improved strength-to-weight ratio in high-temperature applications. These unique properties have made γ-*TiAl* an ideal material for manufacturing low-pressure turbine blades. However, γ-*TiAl* is also a brittle material with low fracture toughness (damage tolerance) at room temperature. This downside makes machining of *TiAl* extremely difficult. While γ-*TiAl* material research has been active over the last 30 years, its application in commercial aerospace engines is still limited to low-pressure turbine blades in GE's latest generation "GENx" engine (Bewlay et al., 2016). According to Zhang et al. (2001), γ-*TiAl* has lower thermal expansion and specific heat than comparable turbine materials. The orientation and lamellae boundary micro-cracks along grain boundaries also contribute to the machining fracture mode. Aspinwall et al. (2005) conducted a comprehensive review of γ-*TiAl* intermetallic alloy performance during machining operations such as grinding, drilling, milling, and turning. While a grinding operation produced a crack-free workpiece surface, they reported poor surface integrity such as deformed lamellae, strain hardening, grain pull-outs/cracking, and poor tool-life in milling and turning operations. However, all of the research published has been confined to post-mortem defect analysis, making them of little use in real-time process monitoring and optimization. Subsequently, industrial attempts to develop machining methods for *TiAl* alloys have been restricted to empirical studies which have yet to resolve the problem of machining-induced surface and surb-surface deformation during production.

The low-pressure turbine blade's manufacturing process can be abstracted into five steps, as shown in Figure 1-1. Material extraction, casting, and electrochemical machining are the first three (3) phases, representing diverse pre-machining activities. Finish machining and a non-destructive evaluation/quality inspection of the machined product are the final two phases. If the product fails the quality inspections, the next step is to send it for rework, and if that is not feasible, it is discarded as scrap. The product is returned to the manufacturing line for re-checking after rework; however, depending on the production status, it may have to wait before rejoining the line (referred to as 'queuing'). Depending on the second quality check outcome, the product is re-checked against quality standards

and might be reworked or disposed of as scrap. Industry experts identified the finish machining step as the significant bottleneck since all reported surface finish challenges occur after this process.
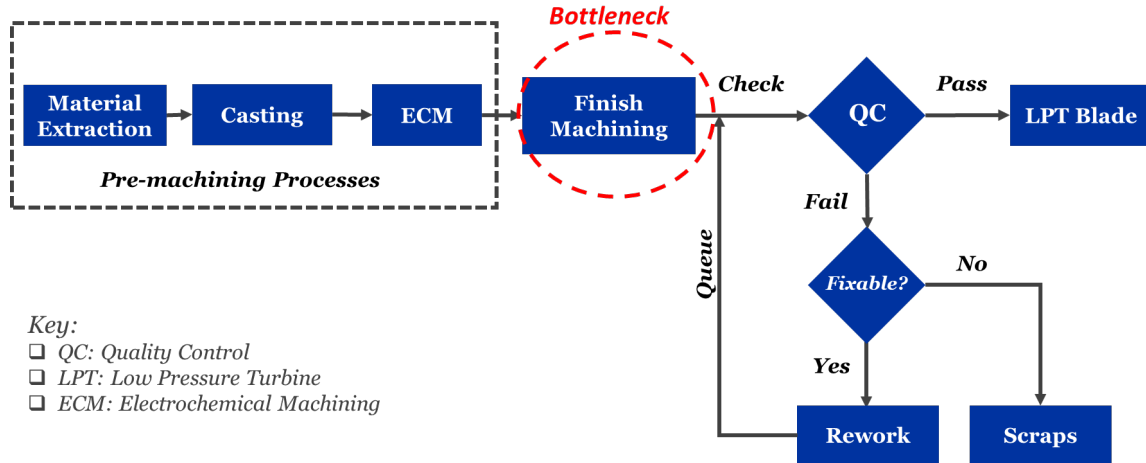
Figure 1-1. Process flow for low pressure turbine blade production

This research focused on improving the manufacturing/finish machining of titanium aluminide alloys due to their unique and desirable properties, especially in aerospace applications. It further explored the real-time investigation of titanium aluminide alloy machining to understand the crack initiation and propagation mechanism. With the possibility of creating a digital process twin framework, the ultimate goal is to achieve in-situ process monitoring and control for turbine alloy manufacturing. Insufficient digital manufacturing tools have forced turbine manufacturers to adopt conservative empirically (i.e., low productivity) and inefficient (i.e., high energy consumption) processing strategies to limit manufacturing scrap and expensive rework; this work, however, focused on elements needed for obtaining more aggressive, yet reliable, manufacturing parameters and monitoring techniques for processing γ-*TiAl* alloys via a digital process twin framework. A future implementation of a comprehensive DPT framework would help improve manufacturing performance and energy efficiency by offering more efficient and reliable processing strategies for the industry.

1.3 NOVELTY OF THE PROPOSED DIGITAL PROCESS TWIN PARADIGM

A digital twin framework, as identified by Ritto and Rochinha (2020), is created from the integration of three components (i) computational models, (ii) model calibration and validation using past and current process data, (iii) process uncertainty quantification. Successful integration of these components provides a much-improved process planning, monitoring, and adjustment capability. While much work has been done in cyber-physical manufacturing systems and establishing a digital twin of manufactured components, much of these efforts fail to address the impact of unit manufacturing processes on a given component's physical properties (Leng et al., 2019; Uhlemann et al., 2017). In this context, the authors propose a new definition for a Digital Process Twin (DPT) as an accurate, fast, and efficient virtual process representation that considers the impact of a unit manufacturing process on the physical characteristics of a workpiece, fusing physically informed models and measured data to optimize a given process. This approach is intended to symbiotically augment the popular digital twin (DT) concept, which acts on a higher 'systems' level to digitally integrate the entire product life cycle. Thus, a DPT would be housed within the DT of a component and ultimately serve to inform design-stage optimization efforts, ultimately the key to improving the product, process, and system sustainability (Badurdeen et al.).

The pioneering concept of a digital twin can be attributed to the collaborative work between Michael Grieves and John Vickers; in their 2003 presentation on product life-cycle management (Grieves, 2014), they shared the idea of managing the product life cycle from its virtual model. Grieves lecture highlighted the concept of a flow of information and data from the physical entity to the virtual representation of the product and vice versa, as shown in Figure 1-2, a concept referred to as mirroring or twinning. Twinning between the virtual and physical assets enables measurement and prediction of the physical state and real-time process optimization if necessary. The frequency in which this loop occurs is known as the twinning rate and should occur in real-time to accommodate rapid changes (Jones et al., 2020).
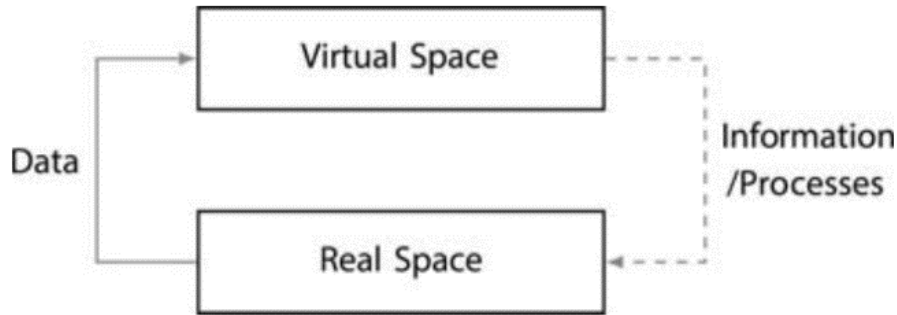
Figure 1-2. Twinning of virtual and physical spaces (Source: Jones et al. (2020) with permission of CC BY 2.0)

Recent advancements in physics, data science, and artificial intelligence have engendered the evolution of Industry 4.0 and smart manufacturing. A NASA integrated technology roadmap (Technology Area 11: Modeling, Simulation, Information Technology & Processing Roadmap; 2010) gave the following definition of a DT; "A digital twin is an integrated multiphysics, multiscale, probabilistic simulation of an as-built vehicle or system that uses the best available physical models, sensor updates, fleet history, etc., to mirror the life of its corresponding flying twin (GlaessgenandStargel, 2012)" (as shown in Figure 1-3).
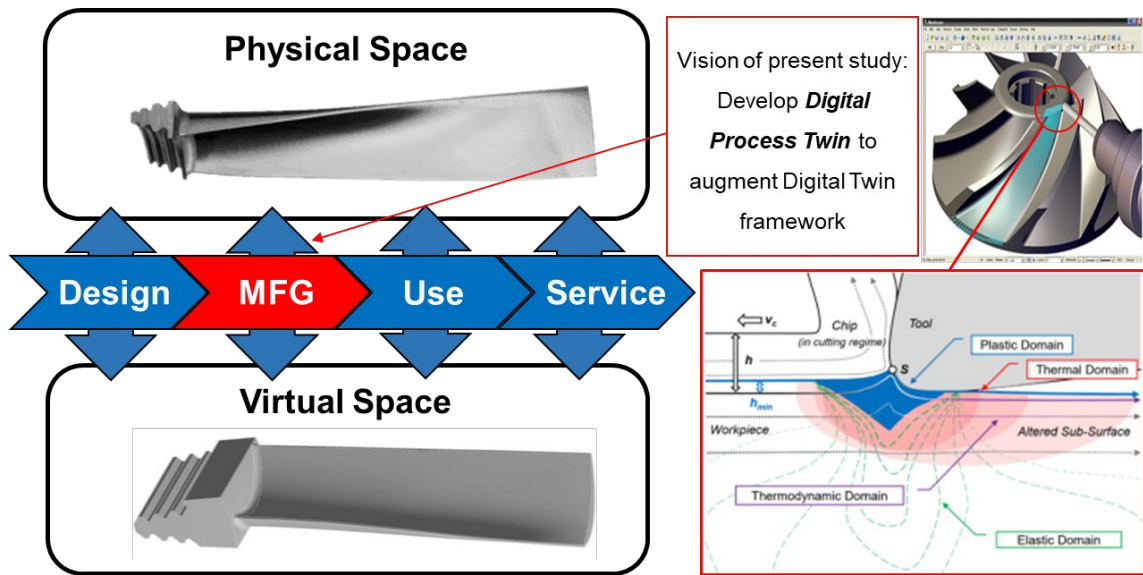
Figure 1-3. Digital twin framework across the product lifecycle and focus of present work on DPT and process physics (adapted from Schleich et al. (2017) with permission of Elsevier Inc., license number 5297310659697)

The product design phase in the lifecycle framework in Figure 1-3 is a virtualized, networked and visual process that has given rise to data-driven product design and cloud manufacturing. According to Tao et al. (2018), the data-driven product design process focuses primarily on physical data study rather than data generation with virtual models, resulting in a lack of convergence between the product's physical and virtual space. Due to the absence of interaction and iteration between big data analysis and diverse operations, the cloud manufacturing-based process cannot respond quickly to real-time changes. A new product design approach was proposed based on digital twins (DT) to address this limitation (Tao et al., 2018). A DT can accurately map all physical data from a product to a virtual environment. The dynamic manufacturing of the product is monitored and controlled throughout the manufacturing stage. Production elements such as cutting parameters and process conditions are gathered and recorded using sensors to monitor the manufacturing process. While extensive research has been conducted in cyber-physical manufacturing systems and the creation of a digital twin of the manufactured components, many of these efforts have failed to address the influence of unit manufacturing methods on the physical attributes of the specific component. This research investigates the development of a digital process twin capable of monitoring and controlling the manufacturing process by leveraging process characterization, sensor technology, and machine learning techniques to address these limitations.

Figure 1-4 illustrates the proposed approach toward calibrating the DPT with in-situ process characterization and leveraging AI to optimize process parameters across a wide range of process and resource efficiency metrics. As shown in Figure 1-4, the sensor selection would be driven by the multi-domain modeling, which helps avoid the common practice of having several sensors on the machine with few valuable data. This approach helps extract needful data while saving costs and resources.
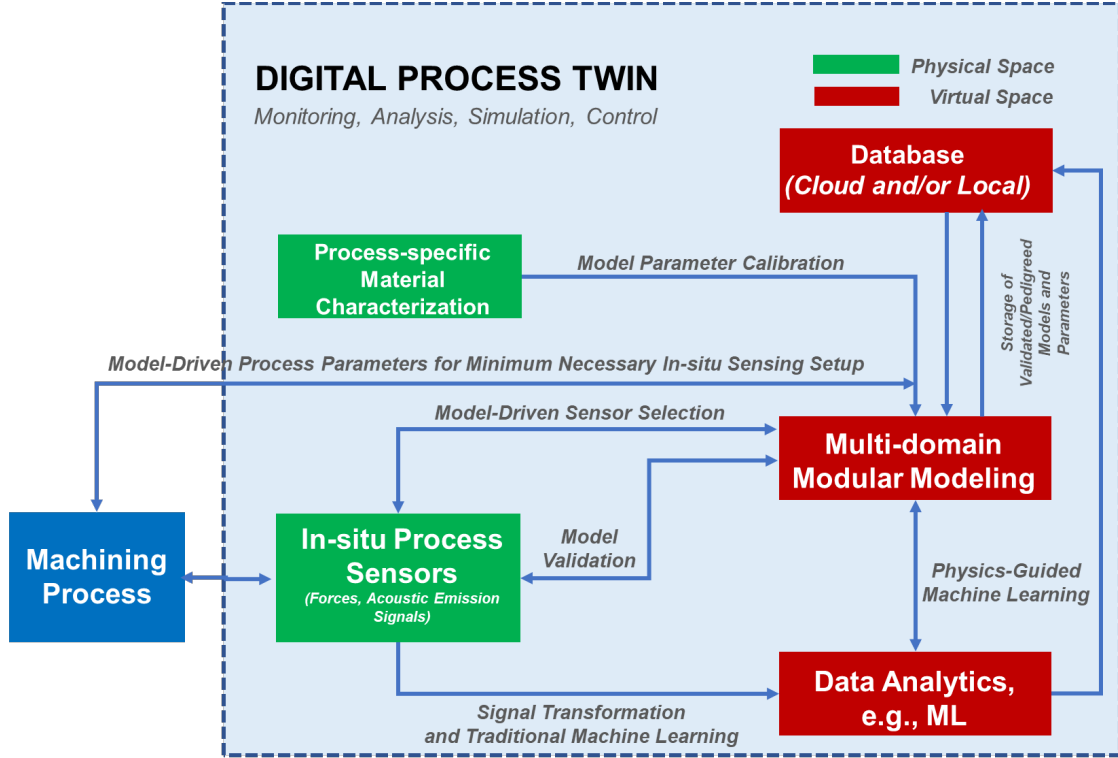
Figure 1-4. Framework of Digital Process Twin

The multi-domain modeling approach helps set the initial process parameter and gives the capability for a modular understanding of the process physics. The modeling efforts are integrated with data analytics tools such as machine learning for improved monitoring and prediction results. However, the multi-domain modeling efforts are not discussed extensively in this present study.

1.4 OVERVIEW OF DISSERTATION STRUCTURE

To address the current challenges with the machining of turbine alloys, especially in a component such as γ-*TiAl* low-pressure turbine blade, this work focused on the real-time characterization of γ-*TiAl* machining and process monitoring with the goal of future development of a comprehensive digital process twin capable of integrating real-time process characterization for model parameter determination, multi-domain modeling, sensor technology, and artificial intelligence to provide improved process control and productivity. The structure of this dissertation is as follows: Chapter 2 provides a background and literature review of the choice alloy, machinability, surface integrity,

modeling, in-situ process characterization, sensor selection, digital twin, and digital process twin. The primary experimental techniques and approaches used to achieve in-situ observation of cutting action and discuss technical challenges will be discussed. Chapter 3 provides an extensive account of the material and methodology with details on the custom in-situ testbed developed at the University of Kentucky for force, acoustic emission, and strain characterization. The sensor-based in-situ characterization results (high-speed imaging, digital image correlation, surface images) are reported in Chapter 4. In Chapter 5, the acoustic emission signal data collected were converted into two-dimensional scalograms and integrated with a machine learning technique for real-time quality monitoring. The process improvement impact on production metrics such as time, energy, and cost are reported in Chapter 6. Finally, in Chapter 7, a summary and outlook for the future is provided.

CHAPTER 2.

BACKGROUND AND LITERATURE REVIEW

2.1 APPLICATION AND PROPERTIES OF TITANIUM ALUMINIDE ALLOYS

Titanium intermetallic alloys such as $TiAl, Ti_3Al, Al_3Ti, Ti_2AlNb$ are currently gaining ground in the aerospace and automotive industry due to its suitability for high-temperature applications, good oxidation, and creep resistance. $TiAl$, for instance, has a highly ordered structure responsible for its unique physical and mechanical properties: high melting point, low density (4.5 g/cm3 for conventional Ti alloys and 3.7–4.7 g/cm3 for *TiAl* alloys), high Young's modulus (96–117 GPa for regular Ti alloys and 100–176 GPa for *TiAl* alloys), high strength, resistance to oxidation, and corrosion. Compared to conventional titanium, steel, and nickel alloys, *TiAl* low density offers improved strength in high-temperature performance, as shown in Figure 2-1.

TiAl alloys are well suited for low-pressure turbine blades and high-pressure compressor blades, usually manufactured of nickel-based superalloys (nearly twice as heavy as *TiAl*-based alloys). However, since high strength adversely affects ductility, *TiAl* is also a very brittle material with low fracture toughness at room temperature. This downside makes *TiAl* machining a complicated process and limits its industrial application. General Electric recently reported that Precision Castparts Corp.'s -*TiAl* low-pressure turbine blades were employed in GEnx engines which powered Boeing 787 and Boeing 747-8 aircraft (Bewlay et al., 2016). This occasion was the first time *TiAl*-based alloys have been used on a wide scale in a commercial aircraft engine. Commercial applications of *TiAl*-based alloys in the vehicle industry include high-performance turbochargers and exhaust valves for Formula One and other sports cars (Dimiduk et al., 2003; SommerandKeijzers, 2003). Additionally, alloys based on *TiAl* have also found limited use in military aircraft and the nuclear sector (BartolottaandKrause, 1999).

While *TiAl* material research has been active over the last 20 years, its application in aerospace engines is limited to mainly GE applications as a low-pressure turbine blade in its latest generation "GEnx" engine. According to Zhang et al. (2001) *TiAl* has lower thermal expansion and specific heat compared to existing materials. The poor ductility in

TiAl is due to its low dislocation density and propensity for cleavage fracture. The orientation and lamellae boundary micro-cracks along grain boundaries also contribute to the machining fracture mode.
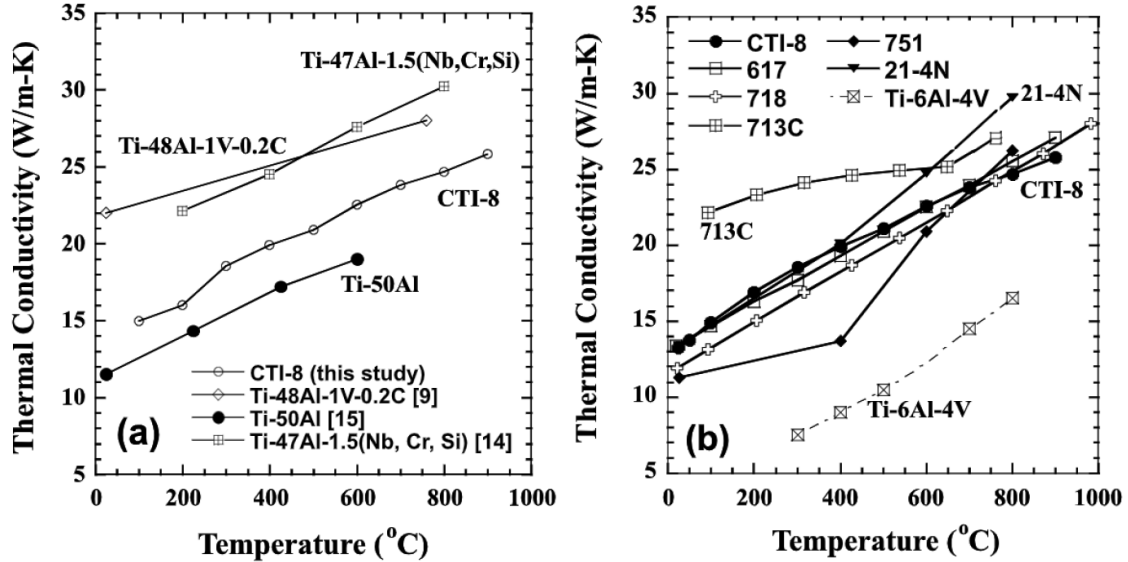
Figure 2-1. Comparison of thermal conductivity of CTI-8 with (a) other *TiAl* alloys and (b) with currently used materials (Source: Zhang et al. (2001) with permission of Elsevier Inc., license number 5297311041099).

2.2   MICROSTRUCTURE OF TITANIUM ALUMINIDE ALLOYS

Titanium aluminide ($TiAl$) alloys are ordered intermetallic materials formed from the strong affinity between titanium, a high percentage of aluminum (about $22 - 56\%$), and elements such as niobium, chromium, silicon, and boron. Over the years, the microstructures of *TiAl* alloys have been grouped under three categories, namely alpha-2 ($\alpha_2 - Ti_3Al$), gamma ($\gamma - TiAl$). And alpha-2/gamma (α_2/γ) phases. Among these, γ-*TiAl* features unique physical and mechanical properties: high melting point, low density, high strength, resistance to oxidation, and corrosion. It is an intermetallic compound with a high elasticity modulus, strength, oxidation resistance, and density of 3.76 g/cm^3. These desirable and unique properties have made it an alloy of interest across several industries, especially aerospace applications. $\gamma - TiAl$ have an L1$_o$ ordered face-centered structure which includes a broad range of homogeneity dependent on temperature. Figure 2-2 shows

the representation of the central region of a *TiAl* system, which depicts the variety of microstructure obtainable from the two-phase composition.
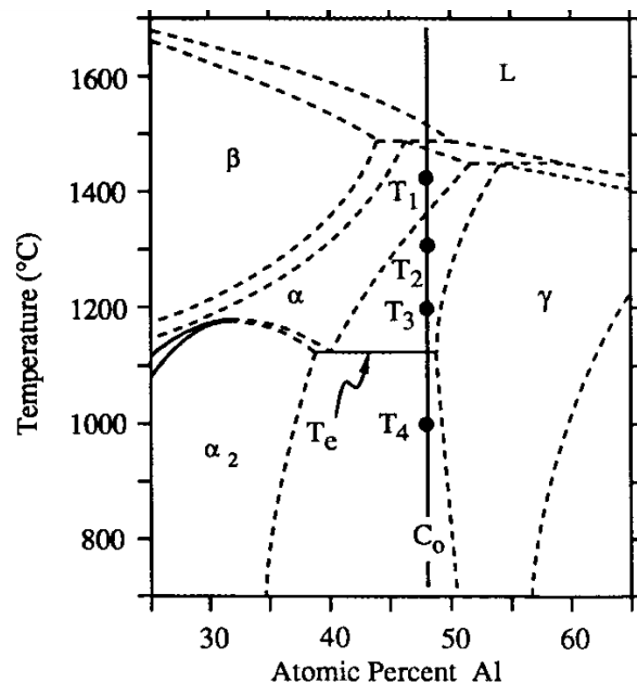
Figure 2-2. The central part of the equilibrium *Ti-Al* phase diagram with the following phases: disordered *β-Ti*, high-temperature disordered *α-Ti*, ordered hexagonal *α₂-Ti₃Al*, and ordered face-centered tetragonal *γ-TiAl*. (Source: Kim (1989) with permission of Elsevier Inc., license number 5297311237517)

The microstructure of titanium aluminide alloys can be grouped under three categories, namely alpha-2 ($\alpha_2 - Ti_3Al$), gamma ($\gamma - TiAl$), and alpha-2/gamma (α_2/γ) phases. These alloys comprise a long-range molecular arrangement at ambient and high temperatures ranging up to 1000°C. The properties of titanium aluminide alloys are highly dependent on the percentage concentration of aluminum and the microstructure type and order; thereby, it is important to appropriately identify or distinguish between the microstructures. Figure 2-3 shows the mid-section of the binary *TiAl* phase diagram and representative microstructure derived by mean heat treatments. The shaded region represents the titanium aluminides of the highest commercial interest.
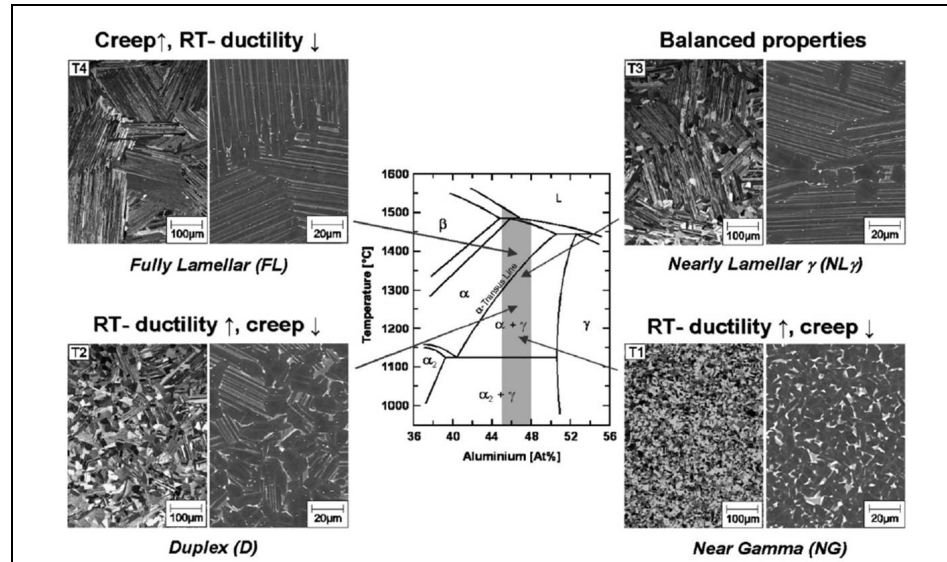
Figure 2-3. Mid-section of the binary $TiAl$ phase diagram and representative microstructure derived using heat treatments (Source: Clemens and Mayer (2013) with permission of WILEY - V C H VERLAG GMB, order number: 1216983).

The alpha-2 (α_2-Ti$_3$ Al) microstructure is made up of about 22-35% aluminum, 12-17 % Nb, 3% V composition and an α_2 stability zone kept in an orderly state at a temperature of 1180°C and above. They are made up of hexagonal structures and, in contrast to γ alloys, $\alpha_2 - Ti_3Al$ have a higher specific strength, lower elastic modulus, and ductility. The α_2/γ microstructural phase consists of 35-49 % of aluminum located in a duplex phase zone. This microstructure comprises two constituents: one in a single γ phase and the other with colonies of eutectoid lamellar structure, typically formed due to the alpha structure transformation during the cooling transition. Typically, the most frequent phase is the $\gamma - phase$ and $\boldsymbol{\alpha_2 - phase}$ exists as a complementary phase. The mechanical properties of the complementary phase microstructure are more balanced when contrasted to single-phase alloys. This is evident in its ability to maintain strength, ductility, and toughness at high temperatures. The gamma phase of titanium aluminide consists of about 49-57% of aluminum, and 1-10% of elements such as Ta, Mo, Nb, Mn, or Cr. It has a tetragonal face-centered microstructure, and it is uniquely known for its fragile behavior caused by restrained dislocation mobility. $\gamma - TiAl$ has an elastic modulus of 175 GPa, lower density, 3.9 g/cm^3, which is relatively higher than that of $\alpha_2 - Ti_3Al$ and other titanium alloys. As established across literature (Bentley et al., 1999;

BeranoagirreandLopez De Lacalle, 2010; Castellanos et al., 2019; Haidar et al., 2009; Kim, 1989), $\gamma - TiAl$ has proven to be a valuable and attractive material in engineering applications.

2.3　MACHINABILITY OF *TiAl* ALLOYS

As defined by the American Society for Engineering Education, "machinability" is a measure of the material response to be machined under a given set of machining parameters such as cutting speed, feed rate, and depth of cut, with a given tool type (tool material and geometry), which should result in a workpiece with adequate functional characteristics, surface integrity, and acceptable tool life. Titanium aluminides are difficult to machine, posing problems for cutting tool makers and materials researchers. An extensive literature review on milling, turning, drilling, electro-discharge machining (EDM), and other operations on titanium aluminides has shown that these alloys are much more difficult to machine than titanium-based alloys (Appel et al., 2011; Clemens and Mayer, 2014).

For instance, the heat conductivity of a workpiece's material is critical to its machinability. In general, the capacity to swiftly disperse machining generated heat via the material is helpful, especially in reducing the cutting temperature. Due to limited heat conductivity, *Ti*-based alloys are more difficult to machine than most other materials. The thermal conductivity of *TiAl* is about 22 W/mK, which is greater than that of typical titanium alloys and nickel superalloys (7.3 W/mK and 11.3 W/mK, respectively), but its effects are just as severe. Small and fine chips are commonly formed during machining. Due to these chips' restricted contact area, quick flow, and poor thermal conductivity, very high cutting temperatures are focused on the tool's cutting edge. As a result, the cutting tools wear out more quickly, compromising the workpiece's surface integrity. Low heat conductivity combined with high strength at high temperatures limits identifying appropriate machining parameter ranges and tool selection, particularly in continuous cutting operations like turning and drilling. The combination of low thermal conductivity and high strength at elevated temperatures produces other problems related to increased cutting forces, energy consumption, and vibrations.

Titanium is notable for its high affinity for many chemical elements. Because of this property, all cutting tool materials tend to chemically react with Ti alloys, especially at cutting temperatures above 500°C (AbbasiandPingfa, 2015; ClemensandMayer, 2016; Sun et al., 2015). High reactivity causes chips to weld at the tool's tip and cutting edge (BUE), leading to increased wear, catastrophic failures, and severe edge chipping. Several investigations show that γ-$TiAl$ and cutting tools have a high chemical affinity and a solid adhesive binding (Ezugwu, 2005; Pervaiz et al., 2014). Furthermore, the combination of this attraction and high thermal stresses causes tool wear by dissolution or diffusion via an increase in the temperature of the cutting zone (AbbasiandPingfa, 2015; Shokrani et al., 2012; Su et al., 2012).

Also, the ductility of an alloy is one of the most desired alloy properties during machining, as it enhances chip formation, chip breakage, and cutting tool life. However, titanium aluminide has an extremely low ductility ranging between 1 and 4% at room temperature due to its intermetallic characteristic. This brittle tendency makes the machining of $TiAl$ a challenging process. Ductility studies carried out by George et al. (1994) on $TiAl$ with α_2/γ structure showed that the angle between the lamellar boundaries along with the load axis significantly contribute to the yield stress of the lamellar structure. The fragile state at the lamellar boundaries significantly influences titanium aluminide alloys' low ductility.

Another essential material characteristic is work-hardening. It is the rise in the hardness of a surface layer and is caused by plastic deformation. This significant increase in the surface layer hardness and thickness causes residual stresses, compromises the part's surface integrity, and adversely affects the components' performance. This phenomenon reduces the cutting tool life due to the increased cutting load of the hardened layers, which causes rapid wear of the tool cutting edge. Surface hardening also impacts the amount of energy needed to cut metal. According to Mantle and Aspinwall (1997), a rise in hardness in γ-$TiAl$ machining implies a high sensitivity to strain hardening, further decreasing the material's already weak surface ductility and reducing fatigue life. Furthermore, they claim that surface hardness levels can be up to twice as high as nominal hardness and that cutting parameters have no impact on this occurrence. The material's cutting contact temperature influences surface hardening, primarily at the layer's depth. Due to the cooling effect that

16

decreases the temperature and the ductility of the workpiece in the cutting region, high-pressure lubrication systems have been proven to induce an increase in maximum hardness of up to 10%. Subsequent sub-sections further highlight the surface integrity challenges faced during the machining of titanium aluminide alloys.

A prevalent challenge in the machinability of titanium aluminide is the occurrence of surface cracking. Existing studies on this issue have shown a significant correlation between the surface cracks and factors such as material microstructure (grain size and type), mechanical properties (strength, ductility, or hardness), selected machining process (milling, drilling, and grinding), and cutting conditions (machining parameters, cutting tools, and environment). Among the material-related factors, the low ductility of γ-*TiAl* has been identified as the leading cause of surface cracking in titanium aluminide machining. Also, the microstructure of γ-*TiAl* was established to influence the surface crack formation, as cracks were seen to be initiated at the γ-γ lamellae interface in α_2/γ alloys. As shown in Figure 2-4, the interlamellar plate failure around the lamellae colonies, due to the applied load's angle, affected the crack formation in *TiAl* alloy turning and milling.
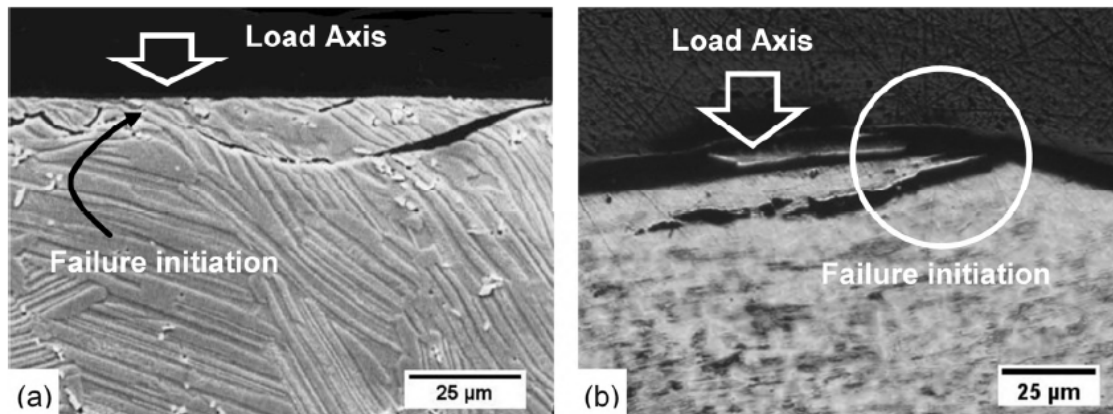
Figure 2-4. Fractography of; (a) turning sample in *Ti-45Al-2Nb-2Mn - 0.8* vol% TiB2, and (b) milling sample in *Ti -48Al -2Nb -0,7Cr -0,3Si* (Source: Mantle and Aspinwall (1997) with permission of Elsevier Inc., license number 5297320115366)

Studies into the cutting condition influence showed that the cutting environment has no significant effect on the crack intensity. The depth of cut significantly impacts the crack size and density by approximately 67% when adopting a low cutting speed and depth of cut between 0.05 and 0.1 mm (Sharman et al., 2001a). A crack geometry of 50 μm width and 5 μm depth was observed in the smallest depth of cut (0.05mm), while a 0.1 mm depth

17

of cut had a crack geometry of 150 μm width and 15 μm depth. Further studies by Aspinwall et al. (2005) also correlated the surface cracks to the cutting tool flank wear and cutting time in gamma XD^{TM} titanium aluminide (*Ti-45Al-2Nb-2Mn-0.8% TiB$_2$*) turning at low cutting speed. Considering the cutting tool selection influence on surface quality in *γ-TiAl* machining, existing studies have cut across the use of coated and uncoated tungsten carbide, poly-crystalline cubic boron nitride (PCBN), poly-crystalline diamond (PCD), and cubic boron nitride (CBN). It has been established that using tungsten carbide cutting tools has a great propensity for surface cracking compared to other tool types. This tendency is because cutting tools such as PCBN and PCD can maintain their sharp cutting edge longer than WC tools. This observation established a strong correlation between surface integrity and tool wear.

Thus far, the commonly adopted technique to avoid surface cracks formation in machining is to increase the cutting speed for a rise in cutting temperature and ductility at the tool-workpiece interface, which helps reduce the chance of crack initiation and propagation. However, the downside is the concurrent increase in thermal load and accumulation at the cutting edge resulting in rapid tool wear or low tool life. Also, this approach is challenging to adopt in titanium aluminide machining since the cutting temperature must exceed the brittle-to-ductile transition temperature of 600°C - 700°C. The estimated cutting temperature at the cutting tool-workpiece interface is around 420°C which is below the brittle-to-ductile transition temperature. To overcome this limitation in *TiAl* machining, Uhlmann et al. (2009) proposed a workpiece pre-heating approach. They established that pre-heating the workpiece to about 300°C significantly reduced the size and density of surface cracks as to room temperature machining. Increasing the pre-heat temperature to 700°C reduced the macro-cracks to micro-cracks, and >800°C preheat temperature eliminated the surface cracks after machining. As discussed in reported literature, the driving force behind surface finish research in *γ-TiAl* machining is the need for fatigue life improvement during application. The adoption of cracked surfaces in crucial applications is strongly discouraged due to fatigue failure during use (Bewlay et al., 2016).

Surface roughness is one of the principal terms used to describe machined components' quality and measure machining accuracy. A good surface finish is essentially

and often desired for improving the machined component's tribological properties, corrosion resistance, fatigue strength, and aesthetic look.

However, machining parameters such as cutting tool edge geometry, feed rate, cutting speed, and depth of cut have the most influence on the final surface roughness (Shokrani et al., 2012; Su et al., 2012; Sun et al., 2015). Khorasani, Yazdi, and Safizadeh (2012) came up with six influencing categories in several attempts to categorize parameters that influence the surface roughness (namely, tool properties, workpiece properties, cutting parameters, machine tool properties, thermal parameters and dynamic parameters). The primary sub-surface defect in titanium aluminide machining, namely, residual stresses and hardness, results from lamellar deformation during the applied machining steps (roughing, semi-finishing, and finishing operations). This phenomenon is due to the low ductility and the ability of titanium aluminide alloys to maintain their strength at high temperatures. The thickness of the deformed microstructure can assess the effect of cutting parameters on lamellar deformation. However, it has been observed that the distorted microstructure's depth can be reduced by employing additional techniques such as laser-assisted machining (LAM), ultrasound-assisted machining (UAC), or cryogenic cooling strategies.
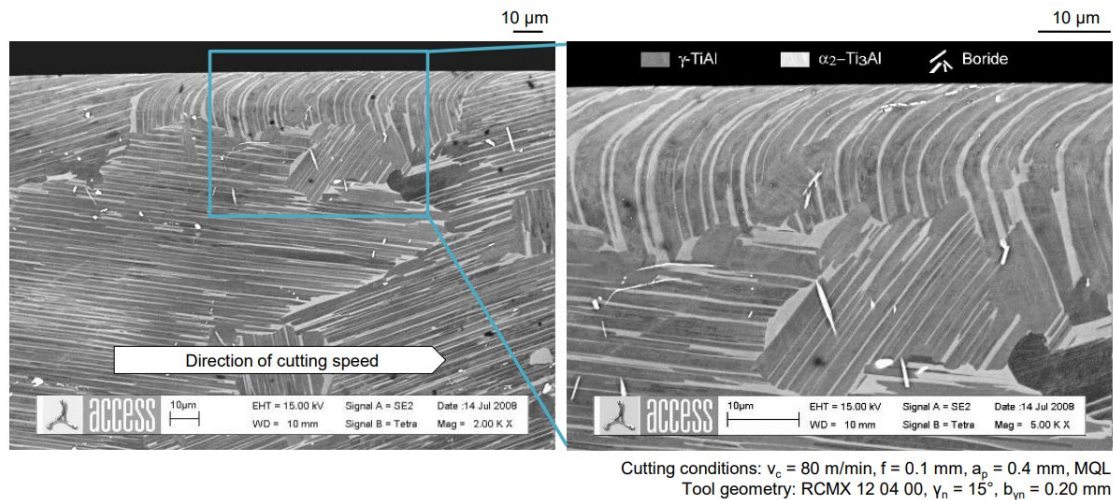
Figure 2-5. Machined surface cross-section showing lamellae deformation in the cutting direction (Source: (Priarone et al., 2012b) with permission of Elsevier Inc., license number 5297320416117)

2.4 CUTTING PARAMETERS INFLUENCE ON TITANIUM ALUMINIDE MACHINING

2.4.1 Cutting Tools Performance

Cutting tools are subjected to heat and mechanical stresses during machining. These stresses are substantially higher for titanium aluminides, resulting in fast cutting-edge wear (Priarone et al., 2012b). As a result, cutting tools must have a balanced set of properties, including temperature resistance, mechanical strength, toughness, and hardness. Various types of high hardness cutting tool materials, such as cemented tungsten carbide (WC), cubic boron nitride (CBN), and polycrystalline diamond, have been used to investigate the machinability of titanium aluminides (PCD) (Bentley et al., 1999; Castellanos et al., 2019; Priarone et al., 2012b; Sharman et al., 2001b). Tungsten carbide tools (WC) are the most popular among these materials in research. These tools can be coated with single or multiple layers of aluminum oxide (Al_2O_3) to increase their performance. The most extensively used industrially are cemented carbide tools. High fatigue strength, compressive strength, stiffness, and hardness are all characteristics of this material. Hard carbide particles, mostly tungsten carbides (WC) bound with metallic cobalt (Co) binder, are compacted and sintered to make these tools. The carbide particle size and binder concentration determine the relative balance of hardness and toughness.

Cemented carbides are grouped into six grades, P, M, K, N, S, and H. P grades are used to machine various types of steel or long chip material and are rated from 01 to 50. In contrast, M grades are recommended for stainless steel and heat resistant alloys, and K grades are used for short chipping materials such as cast iron. They are rated from 01 to 40, N grades are suitable for non-ferrous metals and alloys, S is for heat-resistance superalloys and titanium-based alloys, and H grades are for hard and hardened steel and alloys (Adaskina et al., 2013). It is also worth noting that carbide quality varies significantly from one producer to the next because classification methods do not always define the criteria for classifying carbide grades. Abrasive wear is the most common type of damage caused by WC tools. This deterioration is particularly noticeable in alloys containing more boride (*TiB₂*). According to experimental tests in turning and milling operations, abrasion wear generated by *TiB₂* lowers tool life by up to 10 times and accelerates fracture initiation on the surface (Chen et al., 2021; Venugopal et al., 2003;

Xiong et al., 2016). Comparative investigations of the performance of coated WC tools in the machining of titanium aluminides demonstrate that coatings do not give substantial benefits to the tool. Multiple studies (Celik et al., 2018; Ozer and Bahceci, 2009; Sharif and Rahim, 2007) found that for turning and drilling operations, uncoated WC tools with a higher straight grade, fine grain, and roughly 6wt% Co performed better than coated W. When machining *TiAl* with coated or uncoated surfaces, cutting parameters are essential.

In milling experiments, uncoated carbide tools with cutting speeds of 35, 50, and 71 m/min demonstrated that tool life declines dramatically from 70 minutes to 15 minutes in the 35 to 50 m/min range, but beyond 50 m/min, the tool life pattern changes and becomes practically constant. Furthermore, it was shown that using minimum quantity lubrication (MQL) can prolong tool life by up to 6 times (AbbasiandPingfa, 2015; Zhang et al., 2012). Wet lubrication can extend tool life by up to 24 times under cutting circumstances. Polycrystalline diamond tools and cubic boron nitride (CBN) have been demonstrated to outperform tungsten carbide in *TiAl* machining due to superior abrasion resilience, but only in continuous cutting processes (turning and drilling). However, these materials perform poorly in operations like milling, which is a discontinuous cutting process. For instance, CBN tools show diffusion, flank wear, craters, and built-up edge on the cutting edge when machining titanium. Unfortunately, little information about the tools' service life or cutting time is available. In several investigations in boring operations, CBN has been observed to have more flank wear and a shorter cutting length than cemented carbide tools. This difference is due to the CBN particles' higher binder concentration and greater grain size.

Cutting at a speed of 300 m/min with cutting tools comprising 80 percent CBN and 20 percent *TiC/WC* produced excellent results in terms of surface integrity(Uhlmann et al., 2004). Due to the heat impact of the high cutting speed at the tool/chip contact, almost crack-free surfaces and chips with very smooth undersides are seen. Certain publications (Arif et al.; Dhananchezian et al.; Doetz et al.; LiuandLi; Mcgee) claim that cubic boron nitride tools have a minor advantage over WC tools regarding workpiece surface integrity and process productivity. Furthermore, polycrystalline diamonds for *TiAl* machining appear to be more promising. However, process parameters and workpiece surface integrity, among other things, remain substantially unknown. Commercial cutting

geometries for typical titanium alloys are used in most *TiAl* research projects. However, specific geometries have been less successful in terms of tool life, surface integrity, and productivity.
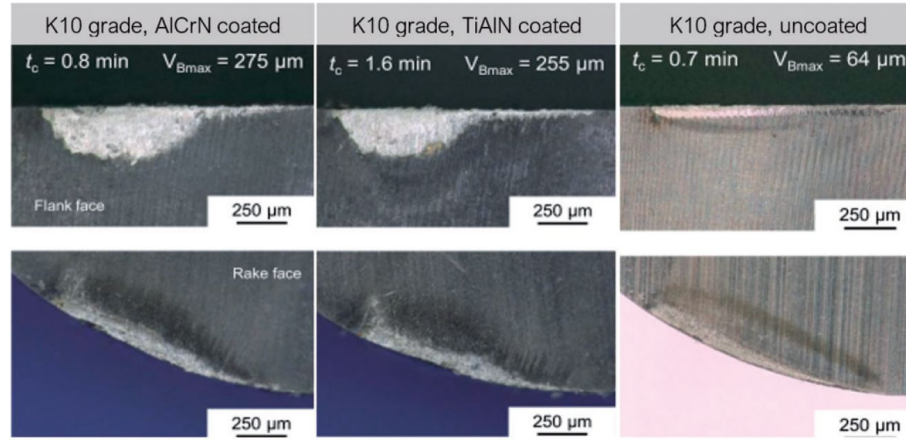
Figure 2-6. Tool wear observation for coated and uncoated ISO K10-grade carbide tools (Source: Priarone et al. (2012a) with permission of Springer Nature, license number 5297320563230)

2.4.2   Tool Wear Effect on Surface Integrity

The cutting tool edge geometry has significantly impacted the cutting process and machined product's functional performance. This edge geometry does not remain constant during a cutting process due to necessary metal-to-metal contact between the tool and the workpiece leading to wear/degradation of the tool edges. The tool edge geometry changes affect the thermo-mechanical properties, influencing the surface integrity factors. The tool wear rate and pattern hugely depend on the machinability of the workpiece and cutting tool material. For instance, Akhtar et al. (2014) noted that the ability of Nickel alloys to maintain their mechanical strength even at high temperatures exposes the cutting tool to both thermal and mechanical shock during cutting. While the tool wear mechanism experienced in different machining conditions varies, adhesion, abrasion, oxidation, and diffusion wear are often limited. The abrasion wear mechanism involves a chip-off in the tool due to the hardness of the workpiece.

In contrast, adhesion involves the clinging of workpiece material to the cutting tool due to high temperature and stress. In difficult to machine materials such as Titanium and

22

Inconel alloys, the high process temperature and tool-workpiece adhesion result in rapid tool wear. Diffusion wear is similar; however, the tool material diffuses due to high heat and is most common at the tool-chip interface. The oxidation wear mechanism involves the reaction of the tool material with its surrounding elements (either the workpiece or environment) at elevated temperatures, leaving a smoothly worn surface.

Studies have shown that the speed and feed at which the cutting tool moves on the workpiece influence the wear rate on the tool due to the generated temperature. An increase in process temperature softens the tool material, making it prone to wear. These wear challenges have led to solutions such as using coolants to reduce the process temperature. However, this solution might be undesirable if a dry machining condition is preferred. Tool coatings, however, as reported by Ucun et al. (2013), are highly effective due to their ability to reduce process friction coefficients, temperature, and a tool-built edge formation. Devillez et al. (2007) investigated the impact of tool coating in reducing tool wear and cutting forces in dry cutting of Inconel 718 superalloy while using a cemented carbide tool. They derived and compared the force ratio for all the coatings to establish the best performing coating and condition. The prominent tool wear observed was due to adhesion and welding of the machined material on the cutting tool edges. The *AlTiN* coating was found to give the best coating performance, and a relationship between the tool wear and expended power was also noticed. Wanigarathne et al. (2005) studied the relationship between the tool wear progression of a grooved insert and the cutting temperature and discovered a strong relationship between the two. Caprino et al. (1996) investigated the tool wear effect on process forces in orthogonal cutting of fiber-reinforced plastics; they noted a strong correlation between the flank wear and the cutting force variations. Zhang et al. (2010) did similar work in an end-milling operation of *Ti-6Al-4V* alloy, slight variation in cutting forces were observed for the first cutting pass due to the initial finite sharpness of the tool, however as the cut progresses and tool wear occurs, the cutting forces increase mainly in the F_y direction due to a change in tool edge geometry and contact length. Besides, they observed that both adhesion and diffusion are the main tool wear that occurs in the process.

The significant impact of tool wear on thermo-mechanical loading makes it critical to study effective surface integrity control and achieve premium product quality/performance. Dogra et al. (2011) reviewed existing literature to establish the influence of the tool micro-geometry on tool wear, surface integrity, chip formation, cutting force, and temperature. The cutting speed has been shown to influence the tool wear due to a directly proportional relationship between the cutting speed and generated temperature. However, high process temperature affects the tool life and impacts the surface integrity of the machined product due to induced tensile stress and might lead to a short-term operational failure of such product. Among the surface integrity factors, most studies have been carried out on the tool wear effect on machining-induced residual stress because of incomplete removal of the thermo-mechanical stresses generated during machining.

Machining-induced residual stresses are difficult to predict due to the complicated interactions between chip formation, ploughing, transient stresses distributions, temperature gradients, and material responses during cutting. An extensive study has been carried out to investigate the role of tool wear on induced stresses (Denkena and Meyer, 2009). Denkena and Meyer (2009) proposed managing the impact of tool wear on residual stress formation in hard turning operations. They argued that since the cutting-edge geometry substantially affects the stress and temperature distributions in the deformation zone, it would be best to modify the edge geometry to reduce the tool wear impact. The cutting tool is modified such that the flank contact length remains nearly constant over the cutting time, thereby producing a more steady and efficient process. Results showed improvement in tool life and a shift in compressive and tensile stress maximum due to lower contact length and cutting forces.

Denkena et al. (2008) investigated the influence of edge geometry and tool wear on induced residual stress in forged aluminum alloy machining and showed a strong relationship between the edge radius and induced residual stresses. Rao et al. (2011) carried out experimental and numerical studies of *Ti-6Al-4V* machining and developed a tool wear model illustrated in Eqn. 1 from the FE model's estimation of temperature and stress, and speed. The influence of the wear on surface integrity in terms of residual stress was observed, and results confirmed good residual stress performance within a limited wear range.

24

$$\frac{dW}{dt} = \sigma_t V_c C_1 \exp\left(\frac{C_2}{\theta}\right) \qquad (1)$$

Muñoz-Sánchez et al. (2011) used a Finite Element Analysis approach to simulate the influence of different cutting parameters on the residual stress generated in orthogonal cutting of AISI 316L steel. The tool wear was generated and controlled using electrical discharge machining, and results showed a corresponding increase in residual stresses as tool wear increased. Liu et al. (2011) studied the influence of the tool nose radius and wear on the residual stress distribution in steel hard-turning. Their conclusion drawn from X-ray diffraction measurements showed an increase in thrust force as nose radius increases; also an increase in surface residual stress and residual compressive stress as tool wear progresses.

Abusive machining of the workpiece can sometimes lead to the formation of a white layer on the machined surface, and these layers are either softer or harder than the base material. Attanasio et al. (2012) investigated the impact of tool wear on the formation of a white and dark layer in AISI 52100 steel turning. Their results showed that the white and dark layer formation increases due to the amount of wear on the cutting tool, and the wear increase is due to the cutting speed increase. Grzesik (2008) studied the role tool wear plays in the resulting surface roughness during hard turning operations with ceramic tools. The author used wiper geometry and standard ceramic cutting tools; Figure 2-7 below shows that the surface roughness increased as the tool wore over the cutting period.
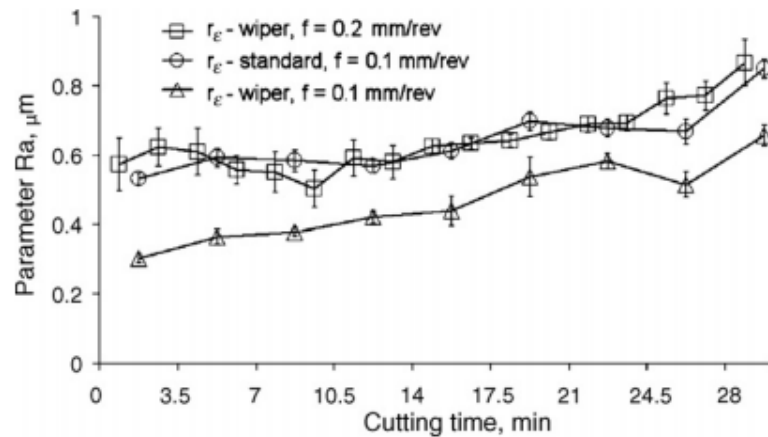
Figure 2-7. Surface Roughness as a function of time for different machining conditions. (Source: Grzesik (2008) with permission of Elsevier Inc., license number 5297320754628)

Li et al. (2014) investigated tool wear effects on surface integrity and fatigue life; they reported lower surface roughness, negligible fatigue life, and higher work-hardening/micro-hardness with an increase in tool wear. A white layer formation was also not observed due to the cooling effect as a result of intermittent cooling in the milling operation; however, in a turning operation, Che-Haron (2001) studied the tool-life effect on surface integrity in titanium at 2mm depth of cut and cutting speeds between $45 - 100m/min$, and microstructural changes along with white layer formation were observed. The cutting tool wear has been shown to increase work hardening, due to plastic deformation and frictional contact between the cutting tool flank and the workpiece surface. A larger contact area caused by the wear increases the plastic deformation and temperature, thereby increasing work -hardening. Zhou et al. (2011) explored the influence of tool wear on subsurface deformation of machined surfaces, using a backscattered electron microscope and EBSD to observe the subsurface features (shown in Figure 2-8). They reported a strong influence of tool wear on the changes in the microstructure, with recrystallization layers formed in grain sizes between 200-300nm.
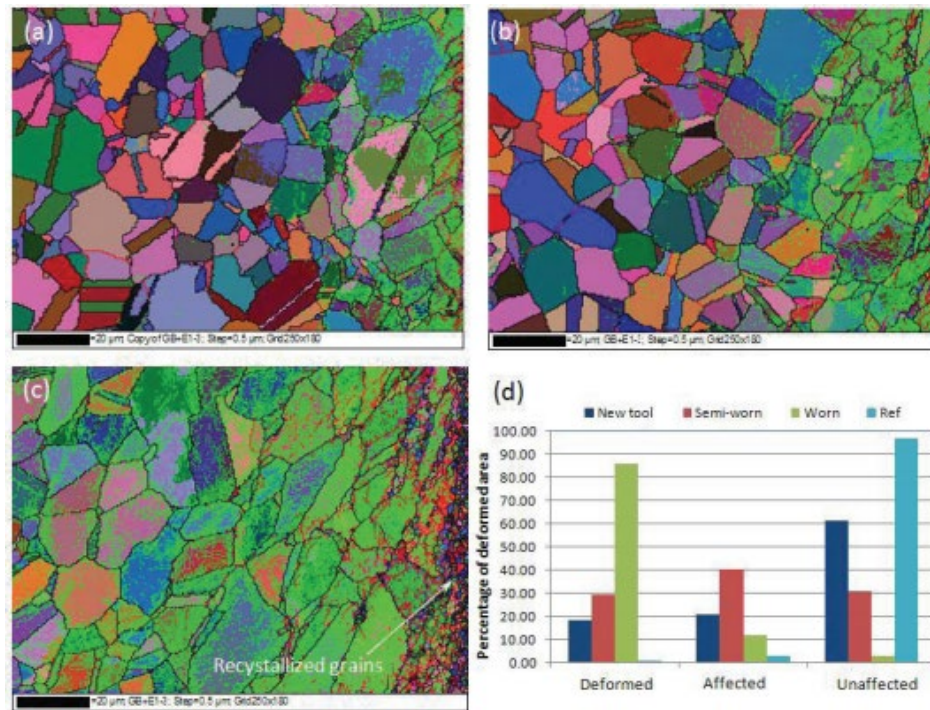
Figure 2-8. EBSD maps depicting the subsurface layer plastic deformation depth (a) new tool, (b) semi-worn, (c) worn tool, and (d) microstructure recrystallization. (Source: Zhou et al. (2011) with permission of Elsevier Inc., license number 5297320940560)

26

Kishawy and Elbestawi (2001) studied the tool wear effect on surface integrity in the high-speed turning of hardened steel; they showed that varying cutting conditions influence the machined surface's surface and subsurface layer properties. They observed that the surface defects generated on the workpiece surface depend on the tool's amount of wear and cutting speed. They concluded that it is possible to control the machining-induced residual stress based on the optimal adjustment of the cutting conditions. Tool wear effect on surface integrity factors such as microhardness and microstructure changes have also been investigated, El-Wardany et al. (2000) confirmed that the amount of wear on the cutting tool significantly influences both the surface microhardness and subsurface residual stress distribution, showing an increase in hardening depth at higher tool wear. Their finite element analysis results confirmed that experimental results were within a 12% deviation. Houchuan et al. (2015) showed variation in microhardness, microstructure, and surface roughness, due to the tool wear. They observed that the severe plastic deformation caused by excessive tool wear could significantly alter the workpiece microstructure.

2.5   SURFACE INTEGRITY IN MACHINING

2.5.1   Surface Integrity Background

A typical machining process consists of the operating equipment, cutting tool, workpiece, and the machine operator; of these connected entities, the workpiece can be deemed most important as other factors ensure its premium quality and enhanced functional performance. Over time, significant efforts have been directed towards achieving durable and functional products by leveraging continual advancements in technology to better understand and control machining processes. The aerospace sector, for instance, places the utmost importance on product quality due to the dire consequences attached to product failure. The surface condition of the workpiece after machining operation is commonly referred to as Surface Integrity. Early publications on this subject include Field (1971) detailed review on surface integrity. They highlighted surface alterations common to machined products, such as surface cracks, induced residual stresses, microhardness microstructure alterations, and built-up edge formation. The adverse effects of these alterations on product performance were noted. In another work,

Field et al. (1972) reviewed pertinent measurement techniques for surface integrity inspection by considering the varying level of surface integrity datasets. In the same publication, they defined surface integrity from a technical perspective as "the unimpaired or enhanced surface conditions or properties of a material resulting from a controlled manufacturing process," and the culmination of their efforts in surface integrity study led to the creation of an American National Standard for surface integrity.

Extensive research works ranging from characterization to measurement techniques of different surface integrity parameters such as residual stress and microhardness were reported between 1970 & 1990. Further studies were done by Tönshoff and Brinksmeier (1980) using experimental methods that investigated the influence of thermo-mechanical properties generated during machining on residual stress distribution and microhardness. At the same time, Brinksmeier et al. (1982) gave a comprehensive overview of the causes and measurement of machining-induced residual stresses. Measurement techniques for surface integrity can be categorized under destructive and non-destructive methods. Destructive testing methods such as metallographic inspection and x-ray diffraction, while widely accepted, are usually time-consuming, limited to crystalline materials, and lack real-time capability. In Brinksmeier et al. (1984) overview of nondestructive testing methods (NDT), they cited the capability of a non-destructive testing ultrasonic method to measure bulk properties of both metal and ceramic materials. At the same time, the ferromagnetic NDT approach is constrained to electrically conductive materials.

In a more recent publication, Thakur and Gangopadhyay (2016) defined surface integrity as the "combination of mechanical, metallurgical, topographical, thermal and chemical features of the surface of a component obtained from a particular manufacturing process, which can be related to the performance during the intended application of the same component." Alterations in induced residual stress can distort the product's mechanical and corrosion properties, while changes in microhardness can adversely affect the wear resistance and load capacity, especially in aircraft components. Early works on these two parameters include Liu and Barash (1976) two-part publication, which studied the effect of both sharp and worn tools on the sub-layer surface properties of the workpiece. They reported a change in residual stress distribution due to increased thermal effect from worn tool face and speed increase. In recent works, Sharman et al. (2006) studied the effect

28

of varying process parameters such as tool wear, geometry, and materials on surface integrity in the Inconel 718 turning operation. In a similar but more recent work, Sharman et al. (2015) focused on the effect of tool nose radius on surface quality and residual stresses in Inconel 718 material. They established that a tool nose radius increase would increase the radial cutting forces, deformation depth in the microstructure, and deepen compressive and tensile residual stresses. To achieve improved surface quality and product performance, Pu et al. (2012) investigated the effect of cryogenic machining on product properties and discovered that applying liquid nitrogen on the clearance side of a tool with a large edge radius yielded an improved surface and refined grains in *AZ31BMg* alloy machining. For various materials such as titanium, inconel 718, the effect of cryogenic cooling on machining performance measures such as tool wear, cutting temperature, force components, and friction was extensively studied (AxinteandDewes, 2002; Pusavec et al., 2014; Rotella and Umbrello, 2014; Sadeghifar et al., 2018; Schoop et al., 2019). *However, this present study will be constrained to dry machining approach due to setup limitation.* The correlation of the surface properties with product functional performance, along with substantial evidence of control, led to the development of models tailored to prediction and control of final surface quality on machined surfaces (Axinte and Dewes, 2002; Pusavec et al., 2014; RotellaandUmbrello, 2014; Sadeghifar et al., 2018; Schoop et al., 2019).

2.5.2 Surface Integrity Modeling

The emergence of newer material alloys, machining processes (such as micromachining), and higher quality standards have further propelled research on surface integrity. Also, the growing need for improved and predictable product functional performance in industries such as the biomedical, automotive, and aerospace sectors have led to the development of predictive models for surface integrity parameters over the past decade. Modeling machining and finishing procedures like grinding, burnishing, and polishing is critical for developing more efficient and sustainable products and processes. Machining is a highly complex process that involves phenomena that have historically been investigated in mechanics, thermodynamics, tribology, industrial engineering, and, more recently, materials and surface engineering. Over the past several decades, developing predictive models for machining performance indicators such as tool-wear/tool-life,

surface roughness, cutting forces/power/torque, part precision, and chip-form/chip breakability has been a significant research focus (Arif et al., 2013b; Ee et al., 2006; Fang and Jawahir, 2002; Jawahir et al., 2020; Jawahir and Wang, 2007; Jawahir et al., 2011; Li and Liang, 2005; Wang et al., 2007).

Much work has been given to modeling cutting pressures, tool wear, and tool life; Frederick Taylor's early models and research focused on this problem. Given the high cost of cutting tools and the need for better productivity and process security, tool-life is a prominent issue to study and anticipate. With the introduction of near-net-shape production methods such as precision casting and additive manufacturing in recent years, a trend toward finishing operations has emerged. Machining operations have become the most adaptable approach for precision finishing because of their unrivaled capacity to achieve exceptional dimensional tolerances, surface finishes at industrial sizes, and reasonable cost. Jawahir et al. (2020) provided a comprehensive overview of the recent development in sustainable machining, focusing on modeling and optimization needs for the future. M'saoubi et al. (2008) noted that while significant efforts have gone into developing empirical, numerical, and analytical models primarily for residual stress distribution, and results show useful predictions, there remain limitations regarding accurate material property characterization, cutting process depiction, and computation speed.

Also, there is an existing predictive relationship disconnect between induced residual stress and fatigue life of the machined product due to complex variables and geometric attributes involved. The need for improved process productivity and product quality has led to the development of predictive models aimed at near exact process simulation that would ultimately end in adaptive control of machining processes. This approach is strongly backed to reduce or eliminate expensive experimental trials and errors. A successful process modeling starts with identifying pertinent process inputs such as the workpiece material properties, cutting parameters, cutting tool geometry, etc. However, since these variables do not directly depict the desired industry quality metrics (surface integrity, roughness, or tool life), the preliminary inputs are first passed through physics-based models to predict the intermediate variables (process Forces, Temperature, Stress, Strain-rate, etc.), which are subsequently used to predict the industry-relevant output (Arrazola et al., 2013; Jawahir et al., 2011; Priarone et al., 2016; ThakurandGangopadhyay,

2016). Figure 2-9 shows a stepwise connection between preliminary process inputs and desired industry quality metrics.
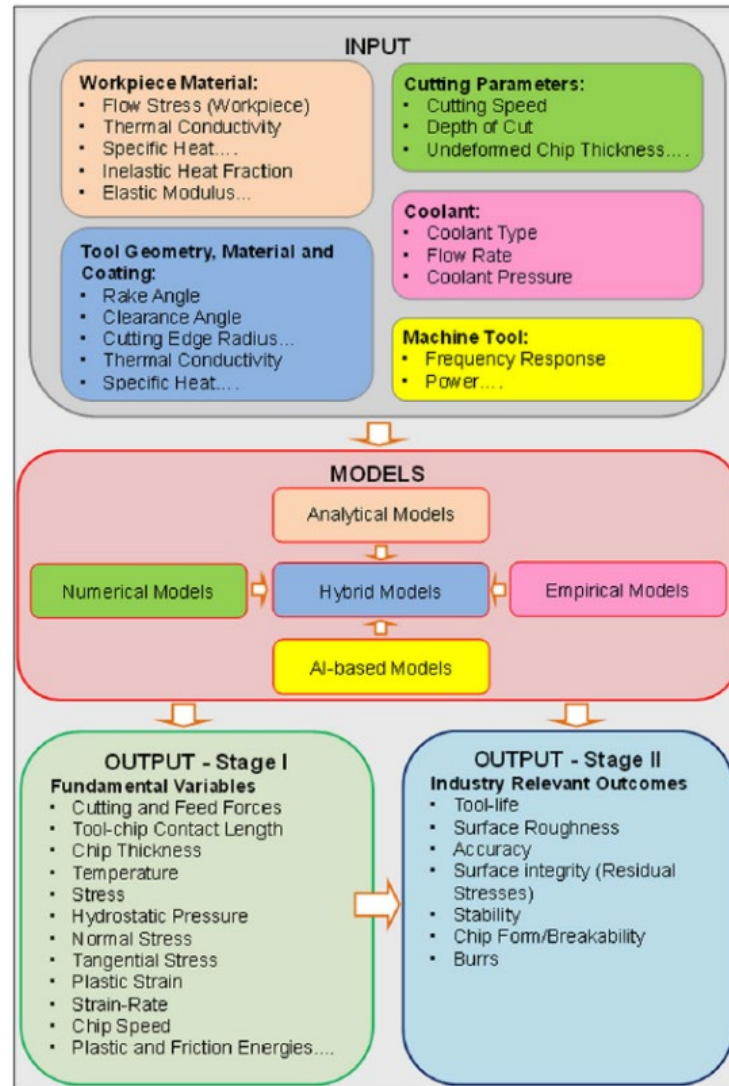
Figure 2-9. Machining process modeling approach (Source: Arrazola et al. (2013) with permission of Elsevier Inc., license number 5263770024758)

Existing predictive modeling techniques have different capabilities and limitations. Numerical models leverage continuum mechanics to predict fundamental variables such as the process forces, temperature, stress, and strain rates. In contrast, analytical models use the slip-line theory principles, though limited to a 2-dimensional setup. Empirical models, however, involve running several experiments and observing trends through data curve fitting, but this approach is quite expensive and time-consuming. Other approaches include AI-based models and hybrid models that leverage different models.

2.5.2.1 Numerical Modeling

Numerical models are built on continuum mechanics formulations such as finite element modeling (FEM), finite difference method (FDM), and boundary element method (BEM). FEM, the most common technique, requires a constitutive material model to establish a relationship between the flow stress and fundamental variables such as strain, strain rate, and cutting temperature. The model coefficients are critical for accuracy and are often acquired from a split-Hopkinson pressure bar (SHPB) test. FEM is subdivided into either an Eulerian or Lagrangian Mesh Formulation. A Lagrangian mesh changes as a function of time and the workpiece material, while an Eulerian mesh assumes a steady state. This fundamental difference makes a Lagrangian mesh approach much preferable across existing studies; however, combining these two approaches births the Arbitrary Lagrangian-Eulerian (ALE) technique, which leverages the strength of both methods for fast solution convergence.

Typical applications of numerical modeling over the years include the prediction of 2D strain distribution, temperature, chip formation, residual stresses, and white layer formation. The application of FEM for residual stress prediction is perhaps, the most common study across existing literature. Some of such works include Özel and Zeren (2007) Arbitrary Lagrangian-Eulerian FE model for the simulation of stress and surface properties induced by a round edge cutting tool during high-speed machining of AISI 4340 steel. Salio et al. (2006) used a nonlinear finite element software to estimate the residual stress distribution in AISI 316L turbine disk turning. Results and measurement trends agreed with experimental data from orthogonal cutting. Figure 2-11 shows residual stress prediction results from Hua et al. (2006) numerical modeling efforts on DEFORM 2D FE software. The authors varied different cutting parameters and studied the corresponding effect on induced stress. Figure 2-11a shows a substantial increase in circumferential stress and slight axial stress increase as both feed rate and cutting-edge radius are increased. Strain fields and strain rates can also be predicted with FE models, Özel et al. (2010) used 3D finite element modeling to obtain the strain distribution for *Ti-6Al-4V* alloy turning (shown in Figure 2-10a), and Özel and Zeren (2006) simulation result showed the strain-rate distribution at the shear zone of AISI 1045 orthogonal cutting (shown in Figure 2-10b).
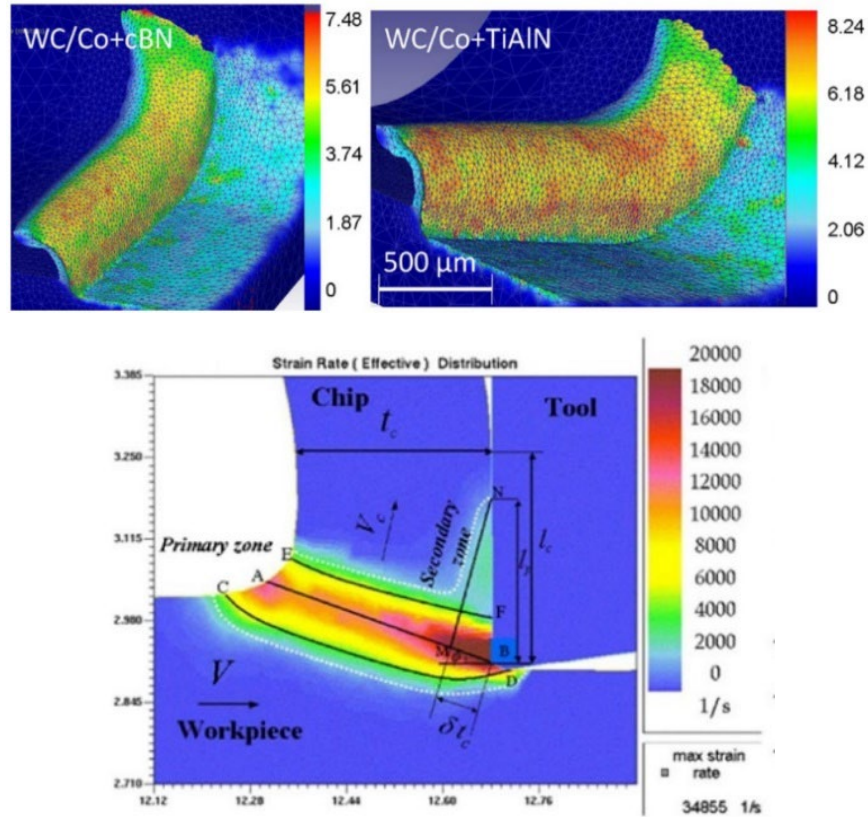
Figure 2-10. (a) Predicted strain fields with FE simulations during Ti6Al4 alloy (b) FE
simulation of chip formation during AISI P20 steel and carbide tool (Source: Özel et al.
(2010) with permission of Elsevier Inc., license number 5263770505901)
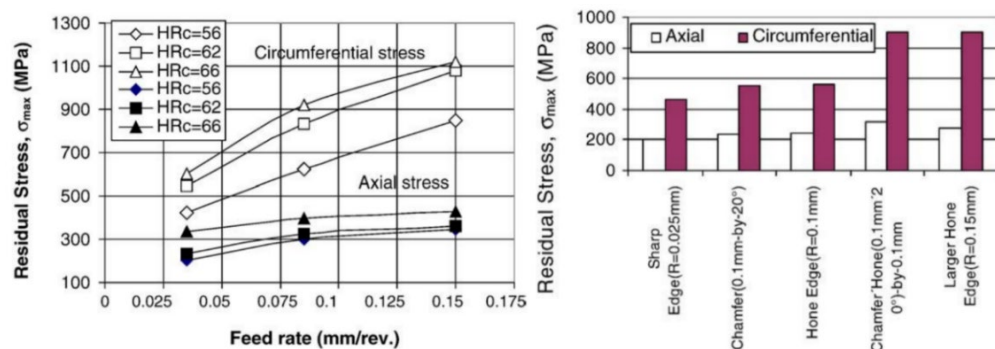
Figure 2-11. Effect of (a) feed rate on the maximum compressive residual stress for
different hardness (chamfer and hone: 1 mm × 20∘ × 0.1 mm, cutting speed = 120
m/min). (b) Cutting edge preparation on maximum residual stresses and penetration depth
(HRc = 62, cutting speed = 120 m/min, feed rate = 0.1 mm/rev) on maximum residual
stress (Source: Umbrello et al. (2011) with permission of Elsevier Inc., license number
5263770370170)

FE models have also seen application in chip morphology prediction, Umbrello et al. (2004) developed a numerical model which integrated both the Johnson-Cook flow model and Brozzo fracture criteria to capture the hydrostatic stress effect on-chip separation; the model was formulated on a Lagrangian mesh approach and implemented in DEFORM-2D FE software. Figure 2-12a and b. compares the observed chip morphology with the simulation outcome.
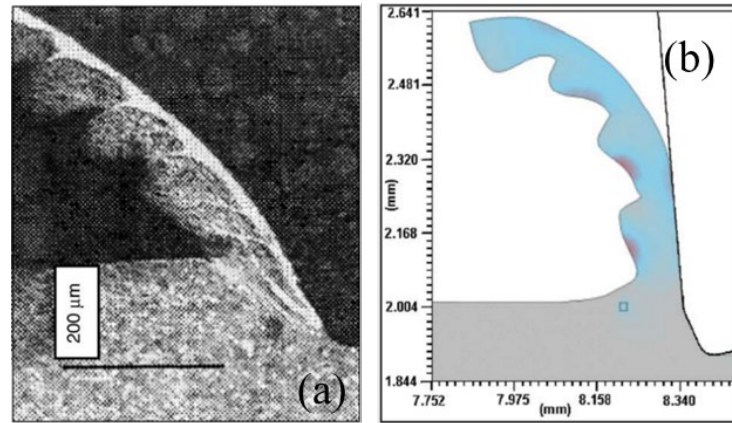
Figure 2-12. Morphology of the chip during machining workpiece with an initial hardness of 53 HRC: (a) observed (b) predicted. (Source: Umbrello et al. (2012) with permission of Elsevier Inc., license number 5297321321062)

Simoneau et al. (2007) investigated AISI 1045 steel microstructure effect on process outcome using FE simulation on *ABAQUS: Explicit*[TM] software. Grain size and orientation effect on micro-machining with a finite sharp tool and two different microstructures (a normalized and four thermal cycles refined microstructure) were studied. FE has also seen application in white layer thickness prediction as Ranganath et al. (2009) developed a FE model to study subsurface deformation as white layers and bent grains in a finishing process. They used a Johnson-Cook model to describe the flow of nickel superalloy material, while results confirmed shear banding and distorted surface layers even at low process speed. In a similar work, Ramesh and Melkote (2008) modeled the white layer formation in orthogonal cutting of AISI 52100 steel and reported that the white layer produced a higher and shifted peak compressive residual stresses on the surface. FEM technique, however, highly depends on the power and performance of the operating computer for reduced computation time and flexibility. Also, while recent

technological advancements have been helpful, there remain drawbacks regarding the accurate characterization of the constitutive model and computation time when compared with other approaches.

2.5.2.2 *Analytical Modeling*

A good understanding of the physics behind machining operations has been a widely embraced approach for analyzing and predicting surface integrity factors such as residual stresses and fatigue life. This approach, commonly referred to as analytical modeling, provides better insight into the machining process through process assumptions at a much-reduced computational time. However, it is essential to be wary of the assumptions made, as the wrong assumptions could falsely represent the process. While analytical modeling is complex and requires an in-depth understanding of process physics, it still depicts the process better than other methods. Early work with this technique includes Liu and Barash (1976) two-part publication, which studied the effect of both sharp and worn tools on the sub-layer surface properties of a machined product. They confirmed that most of the changes in residual stress are due to an increased thermal effect caused by the worn tool face and speed increase. Wu and Matsumoto (1990) investigated the role hardness has on residual stress formation and discovered a strong relationship between the stress pattern and deformation field orientation. Liang and Su (2007) developed a residual stress predictive model using pre-existing force and temperature models. They validated their model with experimental data from the orthogonal cut of AISI 316L and AISI 4340 alloys. In another work, Liang et al. (2008) proposed an inverse calculation approach which allows the use of the desired residual stresses as a pre-specified input to selecting process parameters and cutting-tool geometry.

Yang and Liu (2002) developed a stress-based friction model and studied its influence on residual stresses. Outeiro et al. (2010) used experimental data to develop a model that explored the relationship between size effects and surface integrity because of the edge radius. Ulutan et al. (2007) developed a residual stress analytical model considering the elastic loading, tool and workpiece temperature model, and final relaxation process. The heat equations for the tool, chip, and workpiece were solved using a finite difference approach, and the thermo-mechanical stresses were resolved with an analytical

elasto-plastic model. Lazoglu et al. (2008) proposed an improved residual stress analytical model which used both isotropic and kinematic hardening along with triangular distribution of mechanical forces for enhanced modeling, results were validated with x-ray diffraction measurements.

In recent work, (Schoop et al., 2019) modeled the thermal, plastic, elastic, and thermodynamic domains in machining using analytical and semi-empirical models. The proposed approach was computationally effective and faster (in the order of seconds), with a result deviation around +/- 10%, as shown in Figure 2-13. Regardless of the selected modeling approach, accurate machining process prediction requires precise characterization of the process parameters.
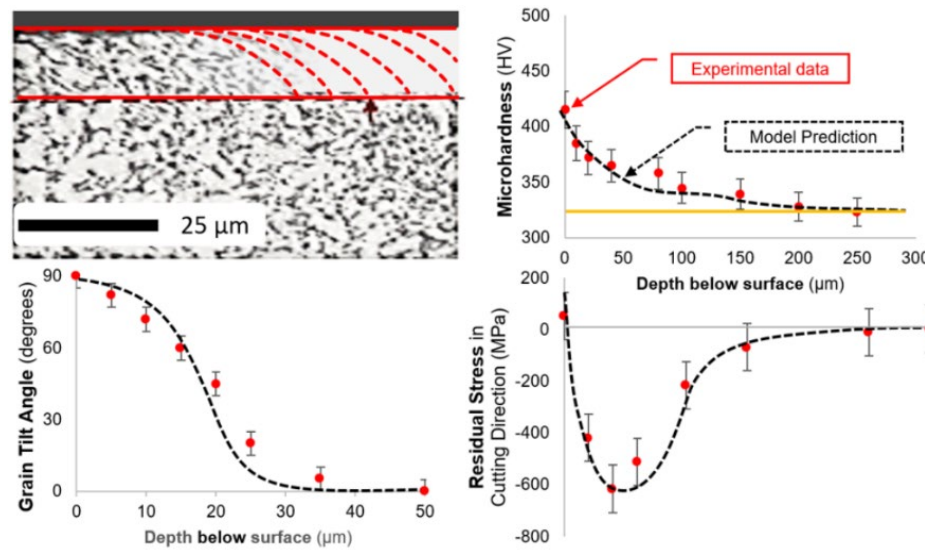
Figure 2-13. Validation of the proposed model in *Ti-6Al-4V* cryogenic machining with $V_c = 60 \ m/min, f = 0.05mm/rev, r_\beta = 25 \ \mu m$ (Source: (Schoop et al., 2019) with permission of CC BY NC ND)

2.5.2.3 Empirical Modeling

Empirical modeling is the easiest modeling approach due to its direct use of experimental trials to understand the correlation between process variables and outcomes. Experimental matrices are constructed to cover a wide range of cutting conditions, and data are analyzed using statistical methods. However, conclusions are only as robust as the experiment scope, and a poor experimental design would limit modeling accuracy. Also, this approach is quite expensive and time-consuming, as there is a need to consider different cutting conditions

for a better understanding of the process. Using a hardness-based flow stress model, Umbrello and Filice (UmbrelloandFilice) carried out empirical modeling of white and dark layer formation of hardened AISI 52100 alloy. Figure 2-14a & Figure 2-14b shows the hardness result after a dry orthogonal turning test at a fixed cutting speed and feed rate. Arrazola et al. (2013) summarize these models' principles, strengths, and limitations as shown in Table 2-1.
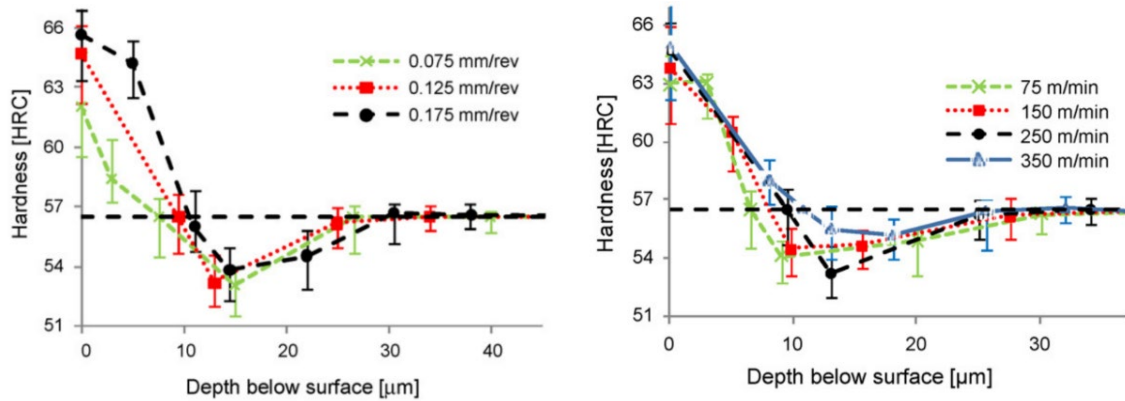
Figure 2-14. Experimental hardness profile of the hard turned specimens at (a) fixed cutting speed of 250m/min and (b) fixed feed rate of 0.125 mm/rev. (Source: Umbrello and Filice (2009) with permission of Elsevier Inc., license number 5263770984700)

Table 2-1. Benefits and limitations of modeling approaches (Source: Arrazola et al. (2013) with permission of Elsevier Inc., license number 5297330394800)

	Analytical	Numerical	Empirical	Hybrid
Principle	Slip-line theory or minimum energy principle	Continuum mechanics using FEM, FDM & meshless FEM	Curve fitting of experimental data	Combines the strengths of other approaches
Capabilities	Predicts cutting forces, chip geometry, tool-chip contact length, average stresses, strains,	Predicts forces, chip geometry, stresses, strain, strain rates, and temperatures	Applicable to most machining operations for measurable process variables only	Provides meta-models for a family of models to be integrated

	strain-rates and temperatures			
Limitations	Usually limited to 2-D analysis with single and multiple cutting edge, but some 3-D models exist	Material model, friction as input, computational limitations: e.g., meshing	Valid only for the range of experimentation	Limited to the strength of the base model: i.e., analytical, numerical, empirical, etc.
Advantages	Ability to develop fast, practical tools	Opportunities to connect to industry-relevant parameters	Practical, fast, and direct estimation of industry-relevant parameters	Improves the capabilities and accuracies of the base models
Disadvantages	Unique to each machining problem	Long computation time	Extensive experimentation, time-consuming and costly	Need for extensive data from experiments and/or simulations

2.6 IN-SITU CHARACTERIZATION OF MACHINING PROCESSES

This section presents a comprehensive overview of past and current research on the in-situ characterization of machining processes in the chip formation mechanism, surface integrity, induced strain, and temperature measurement of the machined workpiece, chip, and cutting tool. The varying material response and findings under the main deformation zones, specifically the primary, secondary, and tertiary deformation zones, are highlighted, focusing on specific considerations for efficient characterization of each unique zone. Various state-of-the-art in-situ characterization setups are discussed and compared, including each approach's relevant strengths and weaknesses. Finally, an outlook for future work in this highly relevant and growing area is presented, most notably the need for more widespread implementation of carefully constructed, diffraction-limited in-situ setups to enable rapid calibration and validation of physically informed and AI-enabled process modeling and optimization paradigms.

2.6.1 Review of Experimental Setups

The earliest attempts towards investigating cutting processes and chip formation have adopted a quick stop device (QSD). The operating principle of the QSD design is centered

on a rapid separation or disengagement of the workpiece and cutting tool (Hastings, 1967). While this method is ex-situ, it is highly relevant for establishing historical significance and the need for more advanced in-situ techniques. This approach made it possible to observe and analyze the chip root after an abrupt 'freezing' of the cutting process. Pioneer reports on QSD setups can be traced to the 1920s when Rosenhain and Sturney (1925) investigated the cutting flow rupture mechanism, and Herbert (1928) also used the QSD setup to study the formation of the built-up edge during a turning operation. Several improved QSD designs were innovated between 1935 and 1970 and reported across (Administration et al., 1961; Bhattacharyya, 1964; Kececioglu, 1958). Notably, one such method is the explosive QSD, which operates by an explosive charge driving a piston alongside the tool post (Hastings, 1967; Philip, 1971; StevensonandOxley, 1969) and an explosively-driven bolt-stop on the tool holder (Ellis et al., 1969; Spaans, 1971; Williams et al., 1970). Stevenson and Oxley (1969) were among the first to attempt strain-rate measurement during orthogonal machining using printed grids and explosive QSD (developed by Hastings (1967)). In this method, they printed 0.002-inch square grids on the workpiece before cutting, and the QSD was used to freeze the assumed steady-state deformation during cutting. They also developed a post-process method to calculate the strain rate by analyzing the streamlined deformation on the printed grids. It is worth noting that the freezing procedure in QSD setups works on the assumption that continuous chip formation is a steady-state process whereby observation at a single instant would accurately depict average streamline deformation. However, Childs (1971) proved that this assumption is fundamentally false through a double exposure imaging technique at a relatively low cutting speed of 0.025 m/min, which made the QSD approach unreliable for detailed analysis of the mechanics of cutting processes. Additionally, a comprehensive study on QSDs by Brown and Komanduri (1973) showed a non-uniform acceleration in the explosive QSD setup capable of wrong tool location. It also exaggerates the pressure energy measurements after a time interval. Thus, researchers stopped using the QSD technique since it fails to provide reliable and quantitative information suitable for the calibration or validation of process models.

The QSD setup limitations caused a shift towards an in-situ (or real-time) study that captures the fundamental behavior of metal cutting processes. The earliest record of

attempts to conduct in-situ cutting process observation was in 1936, when Prof. Schwerd (Schwerd, 1935) at the Technical University of Hannover, Germany. He developed a custom in-situ setup capable of 100 nanosecond exposure to study the transition between continuous and discontinuous chip formation in free machining of (leaded) steel at speeds ranging from 5 to 1000 m/min (0.083 to 16.67 m/s).

2.6.2 Strain and Strain Rate Characterization

A plane strain linear sliding operating principle is based on a stationary or moving cutting tool that linearly advances into a moving or stationary workpiece with its edge perpendicular to its motional direction (also known as orthogonal cutting, shown in Figure 2-15) (Osorio-Pinzon et al., 2019). The in-situ testbeds built on this principle operate with a high-speed or infrared camera directly observing the cutting process to achieve strain and temperature field measurement. This section will discuss the various plane strain linear sliding setups focused on extracting displacement, strain, material constitutive parameters, and friction modeling inputs.
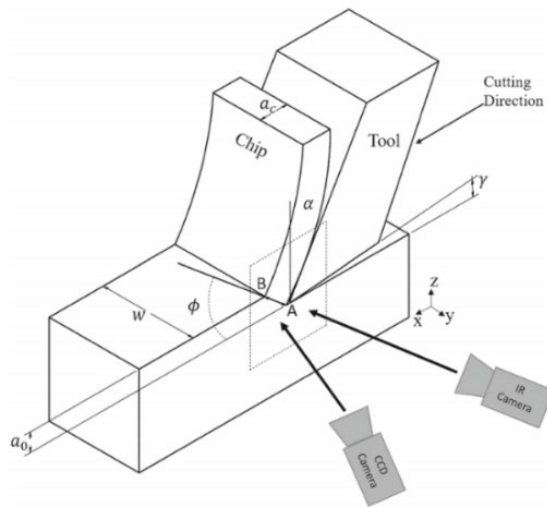
Figure 2-15. Overview schematic of plane strain machining (Source: Osorio-Pinzon et al. (2019) with permission of Springer Nature, license number 5263771188932)

Existing in-situ setups help capture the entire deformation field present in machining processes. Lee et al. (2006) obtained the strain deformation field for dry machined copper using a microscope, a CCD high-speed camera setup with transparent sapphire tools at 1 m/min and 250 fps. The camera offered a spatial resolution of about

3.3um (pixel size) for the process images, while the velocity and strain distribution field was estimated using the PIV technique. Accurate measurement with post-process analysis such as DIC or PIV requires good spatial resolution and low noise; however, this is not obtainable with the intensified multi-channel camera setup. Hijazi and Madhavan (2008) attempted to solve this bottleneck by developing a non-intensified multi-channel camera system comprising four high-speed dual-frame cameras and dual-cavity lasers (camera system picture and schematic displayed in Figure 2-16 and Figure 2-17, respectively). The setup was capable of ultra-high frame rates (up to 200MHz) image capture at default lens and camera resolution. This novel setup bypasses the gating present in the image intensifier, allowing pulsed illumination sources and provided improved spatial resolution up to 2 μm and 0.1% noise.
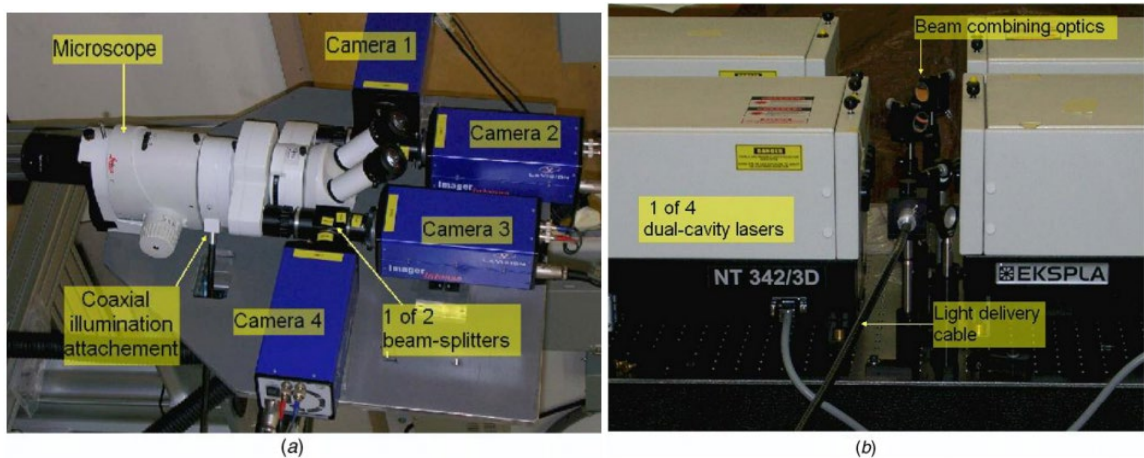
Figure 2-16. Proposed camera system: (a) the four dual-frame cameras mounted on the stereo microscope, (b) the four dual-cavity lasers, and the beam combining optics (Source: Hijazi and Madhavan (2008) with permission of IOP Publishing, order number: 1215802)
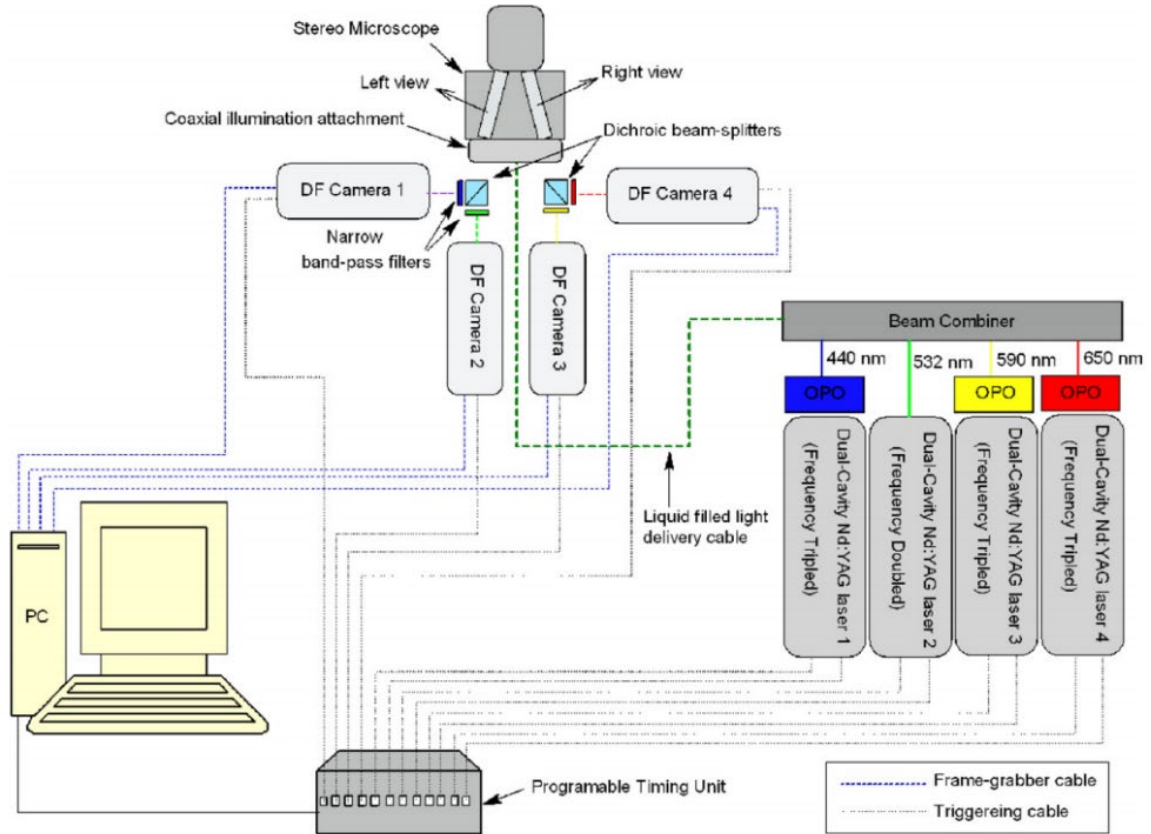
Figure 2-17. Detailed schematic of camera setup (Source: Hijazi and Madhavan (2008) with permission of IOP Publishing, order number: 1215802)

Guo et al. (2015) explored an in-situ observation of the deformation field in orthogonal machining of brass, both in cutting and sliding states. The experimental matrix covered dry-cut observations under plane strain conditions at different rake angles, subsequently controlling the chip formation and deformation field. The experimental setup comprises a novel die assembly (Figure 2-18a and b), providing constrained movement of the workpiece against a fixed tool wedge/indenter using sapphire glass (this allows good imaging). The whole fixture's compression loading enables the workpiece's movement via a plunger placed at the workpiece end. The rake angles on the indenters range between -70° to 15° to adequately capture the cutting and sliding conditions. The process images were processed using particle image velocimetry to extract the grid deformation, strain, and strain-rate distribution. Guo et al. (2015), with the in-situ images displayed in Figure 2-19, confirmed different chip formation modes and prow slope as the rake angle (α) is varied: stable prow/sliding mode (α = -70°), discontinuous chip mode (α= -50°), segmented

42

chip mode (α = -20°), and continuous chip mode (α = 0°). Results established a critical rake angle above which *cutting* occurs and below which *sliding* occurs. While this provides insight into both unsteady and continuous flow field formation, the experiments were limited to a low cutting speeds of about 10 mms[-1], with 5000 frames/sec camera framerate and resolution of about 3.3 μm/pixel.

Improving on the cutting speed, Baizeau et al. (2017) quantified the induced strain fields in aluminum machining, adopting a high-speed double-frame camera and pulsed laser lighting setup for the cutting zone observation. Their design displayed in Figure 2-20 consists of a 30-mJ Nd: YAG laser (capable of 5 – 8 ns pulse duration), a 10x Mitutoyo telecentric microscope, and up to 90 m/min cutting speed. Adopting a double frame CMOS imager allowed a considerably low interframe time of around 120ns; however, the pulsed lighting reduced the camera acquisition frequency to 15Hz. The higher resolution images obtained detected the primary shear angle by combining the DIC technique with a custom numerical procedure to manage image aberrations. They prepared five different surfaces through micro-blasting and varying pressures for the DIC analysis. They obtained a 0.1-micron uncertainty on the deformation regions. They also developed a custom approach for residual strain estimation, with the detailed schematic of the adopted acquisition and synchronization device displayed in Figure 2-21.
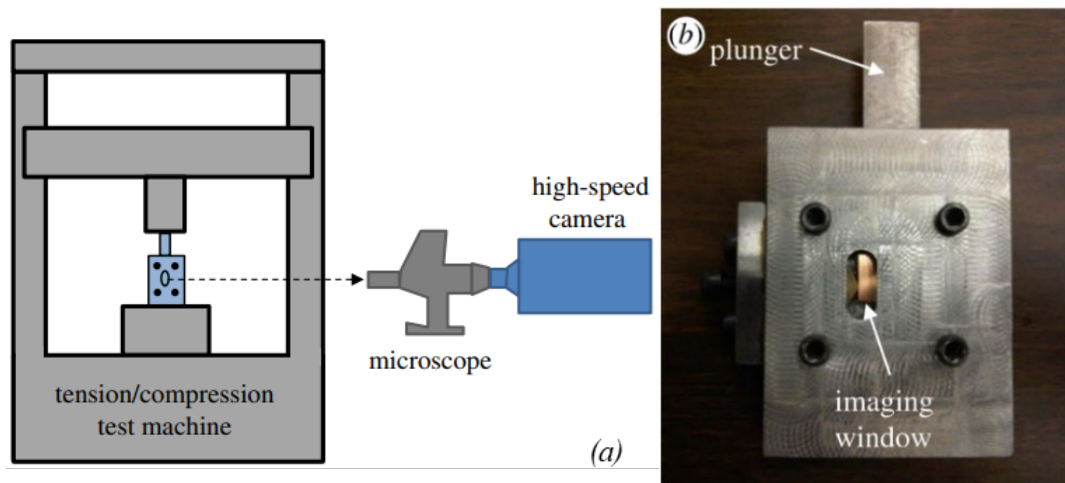
Figure 2-18. Experimental setup (Source: Guo et al. (2015) with permission of Royal Society of London, order number: 1215805).
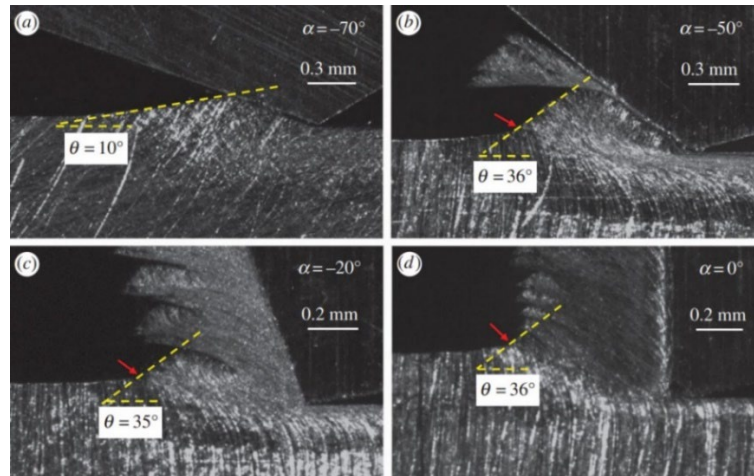
Figure 2-19. Slope (θ) of the prow free surface for (a) stable prow, (b) discrete particle, (c) segmented chip, and (d) continuous chip cases (Source: Guo et al. (2015) with permission of Royal Society of London, order number: 1215805)
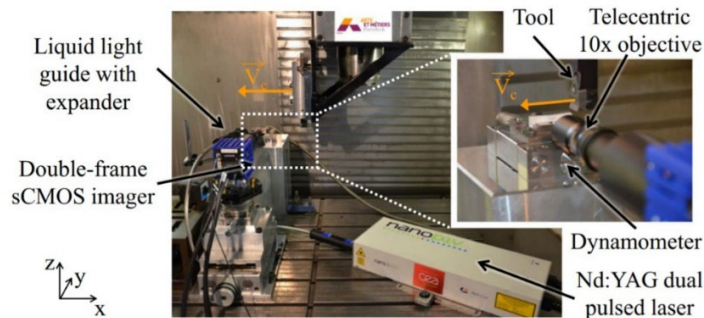
Figure 2-20. Experimental setup adopted by (Source: Baizeau et al. (2017) with permission of Royal Society of London, order number: 1215806)
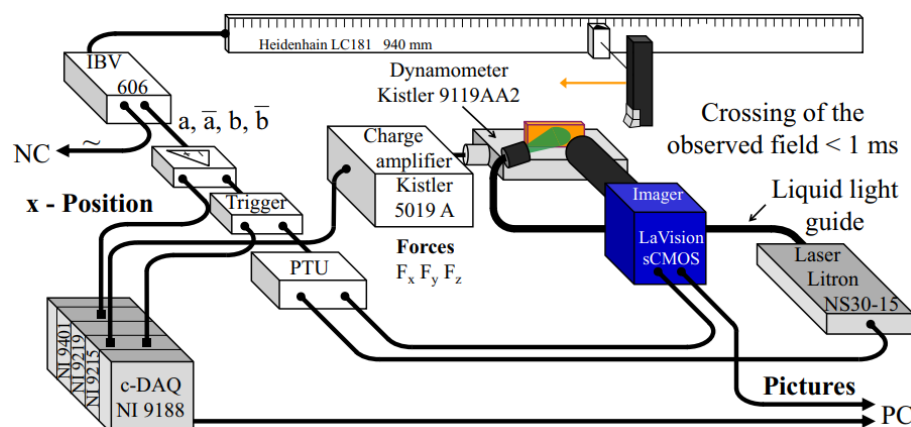
Figure 2-21. Detailed schematic of acquisition and synchronization device (Source: Baizeau et al. (2017) with permission of Springer Nature, license number: 5297340862674)

The focus of most in-situ setups is either strain or temperature field measurements. However, Harzallah et al. (2018) concurrently achieved full-field strain and temperature measurement for *Ti-6Al-4V* machining using a bi-spectral imaging setup, a combination of an infrared and high-speed silicon-based camera (displayed in Figure 2-22). They observed a 500 x 500 µm area by applying a flux spectral separator, an off-axis parabolic mirror, and two 1040 lumen LEDs within a low cutting range of 3 – 15 m/min. However, as highlighted by Zhang (2019), the limitations of this setup include (1) different spatial resolution and acquisition rates between the infrared camera and silicon-based camera and (2) varying surface preparation requirements for digital image correlation and infrared imaging (3) the expensive setup cost of integrating thermal imaging and high-speed imaging. With a high-speed camera (capable of 6000 frames per second and 25 microsecond exposure time), DIC technique, and a heat diffusion method, they acquired and post-processed captured images for strain, strain rate, and temperature estimation. Their results showed a significant influence of the cutting speed on the deformation mechanism. They also reported a combination of shear and compression in the primary shear zone (PDZ) at low cutting speeds, while at higher rates, there exists only a shear action and a decrease in the PDZ breadth.

Arriola et al. (2011) also studied the temperature and strain field developed in steel orthogonal cutting, with an embedded thermocouple and a dual spectrum camera shown in Figure 2-23. The dual setup, which comprised a visual and thermal imaging system, was synchronized to enable accurate matching of the high-speed images with the tool, workpiece, and chip locations. A data acquisition system could extract the process cutting forces concurrently; however, the setup requires special tooling. Also, the extracted images were quite blurry, restricting the study to the primary shear zone.
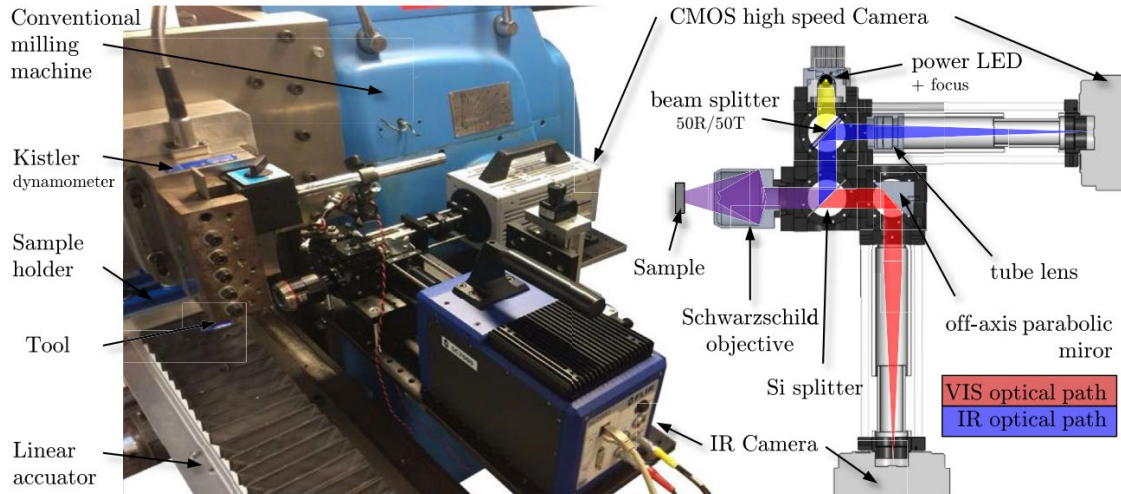
Figure 2-22. (a) Orthogonal cutting device and imaging apparatus (b) Bi-spectral imaging schematic (Source: Harzallah et al. (2018) with permission of Elsevier Inc, license number: 5297340990081)
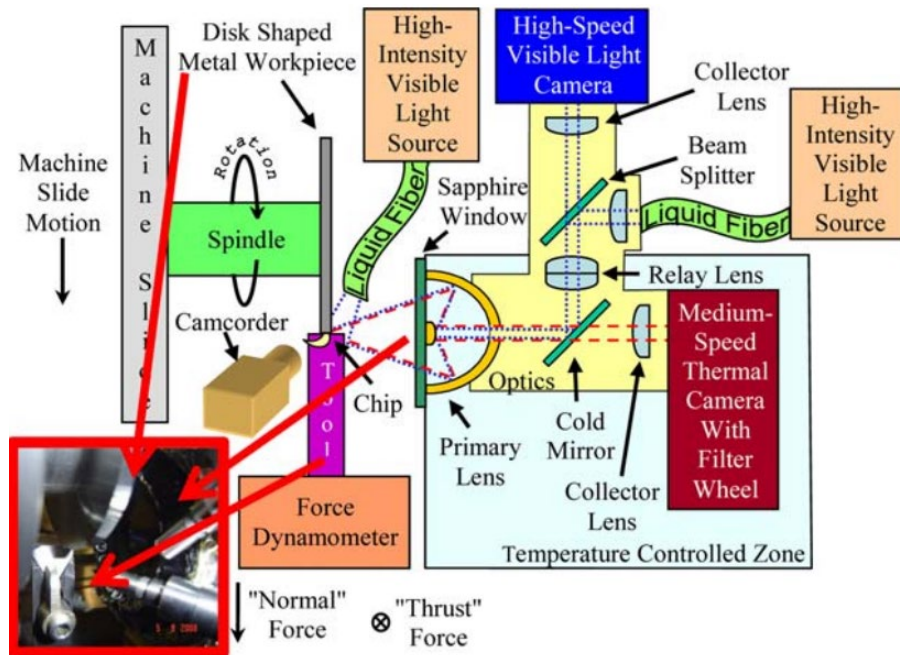
Figure 2-23. Schematic of dual-spectrum camera setup (Source: Arriola et al. (2011) with permission of Elsevier Inc, license number: 5297341233639)

Zhang et al. (2017) investigated the cutting stress distribution during orthogonal machining; they evaluated the deformation field with a DIC technique and effectively combined the experimental results with a material constitutive model. A crucial contribution of their efforts is tweaking the hydrostatic pressure field in the mechanical

equilibrium equations to account for elastic deformation inaccuracies in captured images. Their experimental setup comprised a prodimax HD high-speed camera coupled with a Navitar X12 zoom lens and two 40W high-power LEDs. They cut the workpiece samples into 40 x 13 x 2.5 mm sizes via electrical discharge machining and ground (for oxide layer removal), polished with 220 grit SIC paper and 320 grit micro-bead. This ensured surface patterns fit for accurate post-process DIC analysis. They observed the cutting action through a sapphire glass, which provided a plane strain setup. The authors used the computed stress distribution obtained to calculate the cutting forces indirectly. The results were compared with the experimental force measurements and were in good agreement.

In Germany, Tausendfreund et al. (2018) achieved in-process stress and strain measurements within a nanometer range for a single-tooth milling process. They investigated the impact of process-induced strain on their setup's final workpiece surface integrity, as displayed in Figure 2-24. Their design comprises an Optronis CP70 high-speed camera coupled with a custom periscope optic with an adjustable lens aperture between $f/4$ and $f/22$, yielding a 4080 x 3072 pixels image resolution and a 5.5 µm pixel size at a 10 m/s cutting speed. Understanding that varying parameters (such as speckle size and evaluation window size) can influence the measurement uncertainties in speckle photography, the authors conducted Monte Carlo simulations to determine each parameter's influence. In another work, the authors used the same setup to investigate the workpiece displacement frequent in rough manufacturing (such as rolling, grinding, single tooth milling) conditions (Tausendfreund et al., 2020).

Huang et al. (2020) developed an extended DIC method that reconstructs the displacement field and accounts for the elastoplastic strain and stress distribution during orthogonal cutting. They successfully reconstructed the stress fields by combining the displacement field, estimated from DIC analysis, and the material constitutive model. Experimental results and comparison displayed in Table 2-2 show significant improvement with the model-based finite-element (FE) DIC over a subset DIC and a FE DIC method.
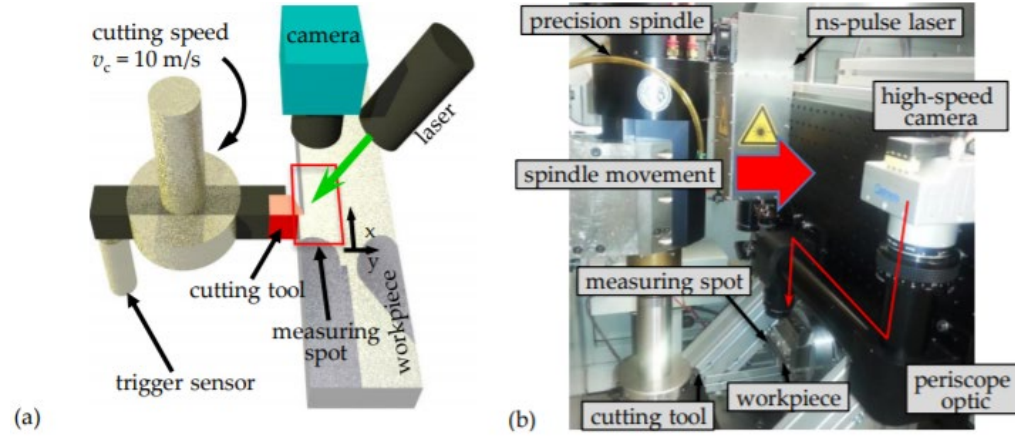
Figure 2-24. Experimental setup (Source: Tausendfreund et al. (2018) with permission of CC BY 2.0)
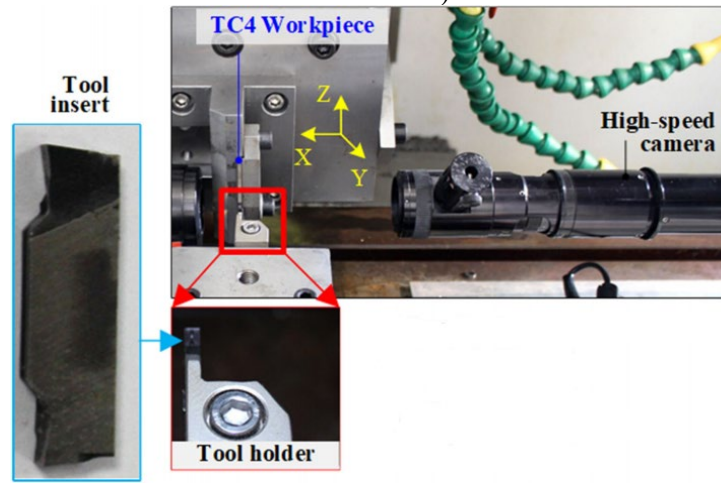
Figure 2-25. Experimental setup (Source: Huang et al. (2020) with permission of IEEE Incorporated, order number: 1216994)

Table 2-2. Performance of different DIC methods on displacement, strain, and stress (Source: Huang et al. (2020) with permission of IEEE Incorporated, order number: 1216994)

Methods	Relative % Errors (Max, Ave)		
	Displacement	Strain	Stress
Subset-DIC	(100.0, 1.70)	(132.4, 73.2)	(825.7, 235.8)
FE-DIC	(111.9, 2.24)	(95.5, 86.8)	(701.6, 51.9)
M-FE-DIC	(0.96, 0.08)	(6.0, 1.4)	(31.3, 6.1)

Several publications have attempted to estimate material plastic constitutive parameters using both in-situ setup and DIC analysis (Cheng et al., 2019; Thimm et al., 2019; Zhang et al., 2018b; Zhang et al., 2019). An inverse method by Thimm et al. (2019)

combined both high-speed imaging and Digital Image Correlation (setup displayed in Figure 2-26), focusing on realistic industry cutting conditions. As shown in Figure 2-27, the input material parameter A, B, and n were first calculated using a nonlinear least square regression analysis. Initial values were assumed for both C and m, which helps estimate the shear strain rate, cutting, and thrust force values. The obtained results (shown in Table Figure 2-3) were compared with experimental results, and the deviations are stored as Q_i. The routine is iterated for varying conditions as defined by the experimental matrix. The deviation values Q_i are summed, and the program only ends when a minimum deviation Q is attained, and the final material parameters signify the optimal values. Based on linear orthogonal cutting tests, their experimental setup comprises a Kistler dynamometer type 9129AA (5 kHz sampling rate), double-cavity Nd-YAG-Laser, and a high-speed camera capable of 2550 x 1600 pixels. The experiments were done at 160 m/min cutting speed, 0.1 mm chip thickness and 750 mm cut length. The Johnson-Cook parameters obtained were compared to those reported by (JaspersandDautzenberg), who used a Split-Hopkinson test setup; results were found comparable and further validated with FEM simulations.

Zhang et al. (2019) also presented a hybrid approach to identifying the material constitutive model coefficients needed for efficient metal cutting modeling via in-situ imaging characterization of the primary shear zone post-process DIC analysis. They quantified the strain and strain rate values in the deformation field of Nickel Aluminum Bronze Alloy cutting; the shear forces were extracted from the stress model and subsequently matched with the measured data using sequential optimization, yielding the constitutive model coefficients. Experiments were carried out at cutting speeds between $30\ m/min$ and $180\ m/min$, with 532 nm wavelength lasers, Kistler 9257B dynamometer, and a dual shutter camera attached to a Navitar zoom lens. FEM simulation was also used to validate the strain, strain rate, and temperature measure from the in-situ characterization by calculating the shear force estimates and matching them against the measured force. It was then solved using optimization and a sequential least square approach. However, they reported blurry images at cutting speeds above 300 m/min and highlighted the need for a dedicated and improved LED lighting system. Besides, since the constitutive models were solely identified from the primary shear zone, they are not suitable for the secondary shear zone FEM simulations due to temperature differences in the two zones. In recent work,

Zhang et al. (2021) also investigated the plastic deformation behavior during orthogonal cutting of AL7075-T6 alloy using digital image correlation and heat convection-conduction techniques. Their results showed substantial strain-softening action in the PSZ and lowered thermal softening action during fast heating scenarios. These efforts also set the tone for further studies on material behavior and robust numerical models.

Denkena et al. (2021) in-situ setup focused on estimating the friction coefficient necessary for improved friction models. They studied the chip formation mechanism adopting a PSLS setup with a Photron Fastcam SA5 camera, Kistler Dynamometer, and digital particle image velocimetry. The study was carried out at cutting speed between 50 – 150 m/min and 10,000 -30,000 frames/sec, with CrAlN coatings. This effort gave a better understanding of the induced friction in cutting processes and significant progress towards friction modeling.
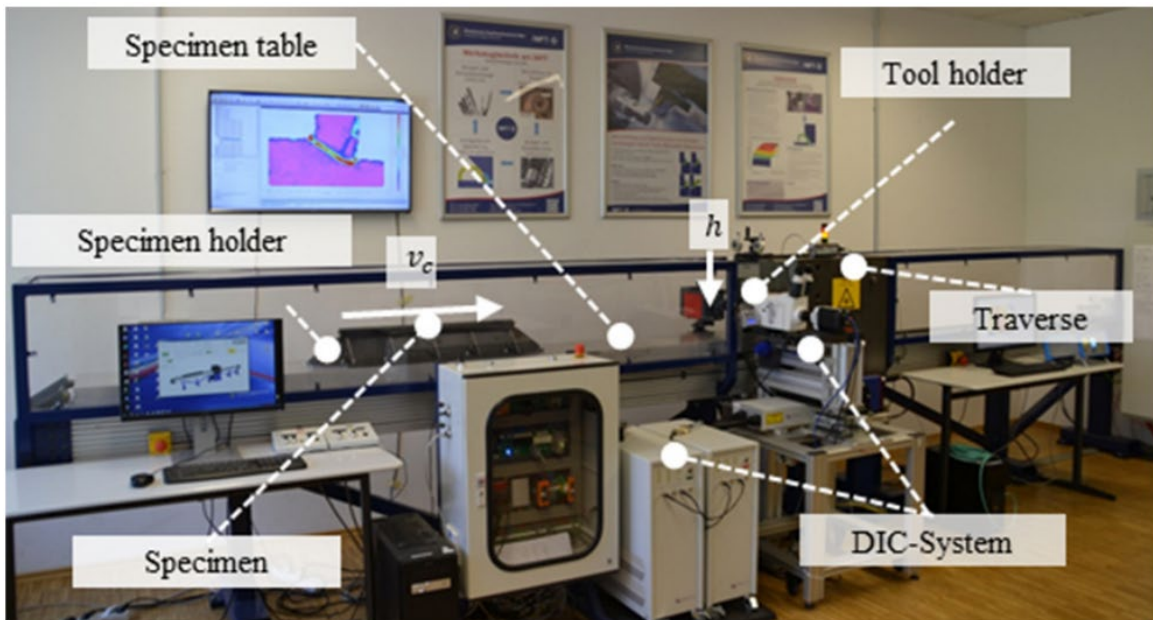
Figure 2-26. Experimental setup (Source: Thimm et al. (2019) with permission of CC BY NC ND)

A, B and n

(C, m)$_{Start}$

$\sigma_f = f(\varphi, \dot{\varphi}, T)$

Experiment: i = 1...M

Cutting conditions: $v_{c,i}$, h_i, b_i, γ_i

Material: λ, c, ρ, T_M

Inverse calculation
$\dot{\gamma}_{AB,i}$, Fc_i, Ff_i

$Q_i = \sum_{j=1}^{N} \left| \frac{w_{Ox,i} - w_{Exp,i}}{w_{Exp,i}} \right| \cdot p_j$

Linear-orthogonal cutting experiments results
$w_{Exp,1} \cdots w_{Exp,M}$

i = i+1

i = M   N

Y

$(C, m) = \min \sum_{i=1}^{M} Q_i$ N

Y

Material parameters: C, m
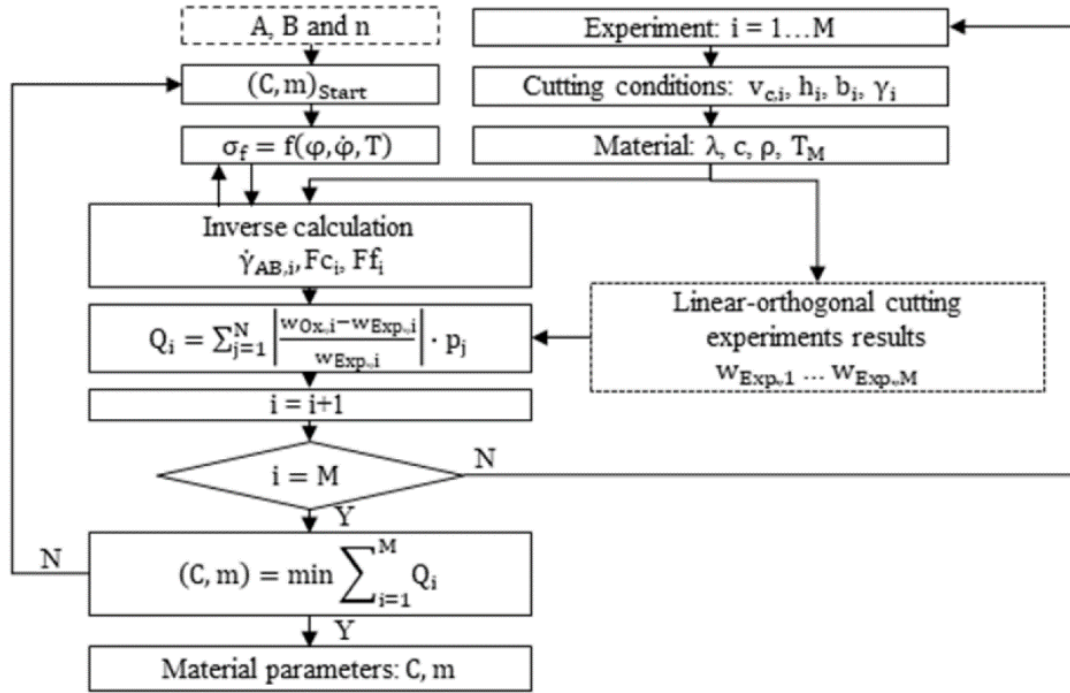
Figure 2-27. An inverse method for determining Johnson Cook parameters (Source: Thimm et al. (2019) with permission of CC BY NC ND)

Table 2-3. Comparison of obtained John Cook model input (Source: Thimm et al. (2019) with permission of CC BY NC ND)

	A in MPa	B in MPa	C	m	n	φ_o in s^{-1}
Inverse	492	585	0.0088	1.2162	0.1677	0.001
Jaspers et al.	553	601	0.0134	1	0.234	1

Large-scale extrusion machining (LSEM) is useful in creating ultra-fine grains by manipulating the severe plastic deformation process. A couple of machining publications have adopted an in-situ study of the cutting process (Cai et al., 2015; Efe et al., 2012; SuttonandHild, 2015). (Cai et al., 2015) studied the strain distribution field present during LSEM of OFHC copper. Combining a novel LSEM device, high-speed imaging, and post-process DIC analysis could better estimate and develop a new shear strain model. They adopted two setups: free and constrained machining setups. The constrained machining displayed in Figure 2-28 helped investigate the geometrical constraint effect on strain distribution present in LSEM. The constraint changed the chip flow direction as the material flows into the PDZ, increasing the inclination angle β as the chip thickness ratio

decreases. A Photron SA-X2-480K-M1 camera was used to observe a 1x1 mm deformation field at 50 fps and 1 micron per pixel spatial resolution.
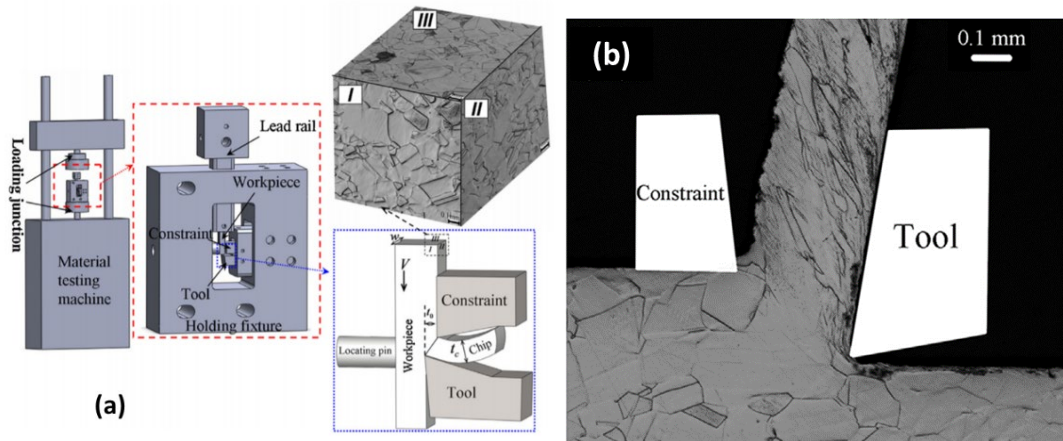
Figure 2-28. (a) Experimental setup (b) captured process image for constrained machining setup (Source: Cai et al. (2015) with permission of Elsevier Inc., licencese number: 5300550674729)

More recently, Schoop et al. (2019) developed a state-of-the-art high-speed in-situ testbed consisting of a custom video microscope with coaxial illumination and a custom-built LED liquid light guide-fed light source (patents: (Schoop, 2020a; Schoop, 2020b)), delivering more than 2000 lumens at the sample (see Figure 2-29c for typical image quality obtained at very short 159 ns exposure time). The setup also comprises a high-speed linear servo motor stage, 50 nm encoder feedback, and various integrated sensors such as strain gages, thermocouples, acoustic emission sensors, and accelerometers. By matching the numerical aperture (NA) and magnification of each objective lens with the CMOS 1024 by 1024, 20 µm pixel size imaging sensor of the Photron SA-Z 2001K, the setup realizes very high spatial resolution (up to 800 nm with Nyquist sampling at 50x objective magnification (0.7 NA)) and continuous acquisition rates up to 2.1 million/second at exposure time down to 159 nanoseconds (representative image displayed in Figure 2-29c).

Figure 2-29a provides an overview of the custom-built in-situ testbed. The testbed was constructed on a ~2-ton granite surface plate (see Figure 2-29b), with a welded steel base bolted into the building's concrete foundation and filled with sandbags to dampen vibrations. The primary cutting stroke (1 m travel length), powered by a proprietary linear servo motor by Yaskawa (experimental series SLGFW2), can achieve up to 4.2 m/s (~250

m/min) travel speed with 5 Gs of acceleration and a peak force above 5 kN. Encoder feedback of 50 nm/pulse and travel straightness of better than 5 microns over the entire stroke promotes exceptionally smooth speed and positional control required for high magnification in-situ microscopy at frame rates up to 2.1 million/second (typically around 200,000 fps) and up to 50x objective magnification. The vertical axis, which controls the uncut chip thickness in 2D cutting (which could also be considered the depth of cut or feed), features positional repeatability of better than 0.4 microns. Integrated foil strain gauges capture cutting forces by Futek, which typically achieve better than 0.2 N force measurement accuracy at a sampling bandwidth of 50 kHz (Futek's IAA300 differential amplifier).

(a)

Z-Axis Carriage for Focus Adjustment (50nm encoder resolution)

Additional 2-position External Diffuse Illumination

Custom 25MPx Coaxial Illumination Machine Vision Vertical Microscope

Adjustable External Coolant/Lubricant Delivery

Non-contact Laser Surface Profilometer

Custom Coaxial Illumination Microscope

Custom High-rigidity (Tungsten) Sample Vise

Y-Axis Carriage for Focus Adjustment (50nm encoder resolution)

Structurally-integrated force and acoustic emission (AE) sensors (F_c, F_f, AE for sample and tool)

X-Axis Carriage for Main Cutting Stroke (v_c up to 250 m/min)

Figure 2-29. (a) Custom-built experimental in-situ characterization testbed setup, highlighting relevant features, with (b) external overview of the overall setup and (c) Representative in-situ image for machining of Inconel 718 at 10x objective magnification, 159 nanosecond exposure, speed = 120 m/min, uncut chip thickness = 70μm. (Source: (Schoop et al., 2019) with permission of CC BY NC ND)

The in-situ PSLS imaging and DIC technique have been applied extensively in CFRP studies (Agarwal et al., 2015; Barile et al., 2019; Li et al., 2020; Topac et al., 2017; Venkatachalam et al., 2018). Agarwal et al. (2015) attempted to understand the impact of anisotropy and heterogeneity frequent in fiber-reinforced plastic machining damage mechanisms by adopting chip, force, and DIC analysis on a speckled workpiece. Figure 2-30a and b show the experimental setup and strain distribution obtained at 0.1 mm depth of cut and 300 mm/min cutting speed. This setup was limited to low cutting speed due to camera capability and design. Also, the captured images, as evident in Figure 2-30b, can be improved. Li et al. (2020) investigated the influence of different hole-making machining strategies (such as abrasive waterjet machining (AWJM), drilling, ultraviolet laser multi-pass machining, and high-power fiber laser cutting) on the surface integrity of CFRP laminates. Adopting a setup of two CCD cameras coupled with 50 mm focal length and two separate illumination sources, they could capture process images of 2448 x 2048 pixels. To ensure speckled pattern for DIC analysis, the CFRP samples were first prepared with black paint coating sprayed on a white background (size of 150-250 micron, shown in Figure 2-31)
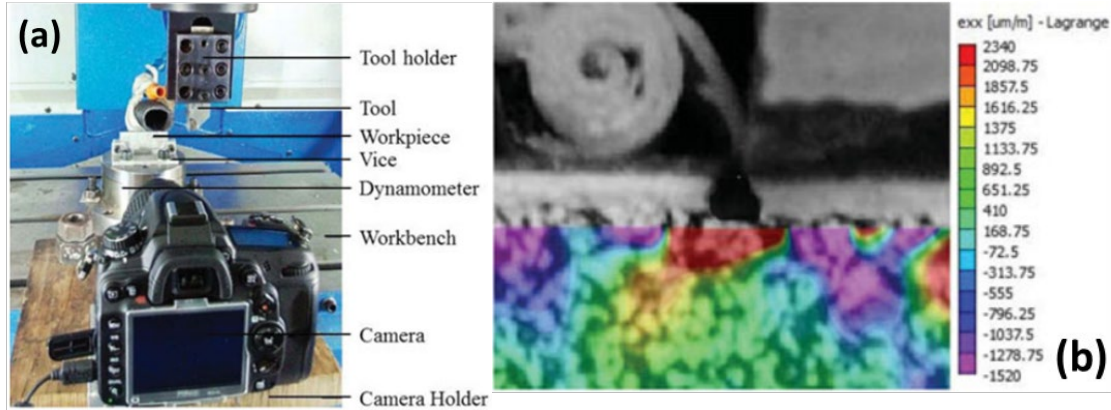
Figure 2-30. (a) Experimental setup (b) ε_{xx} - strain distribution at 0.1 mm chip thickness and 300 mm/min cutting speed (Source: Agarwal et al. (2015) with permission of Elsevier Inc, license number: 5297371134035)
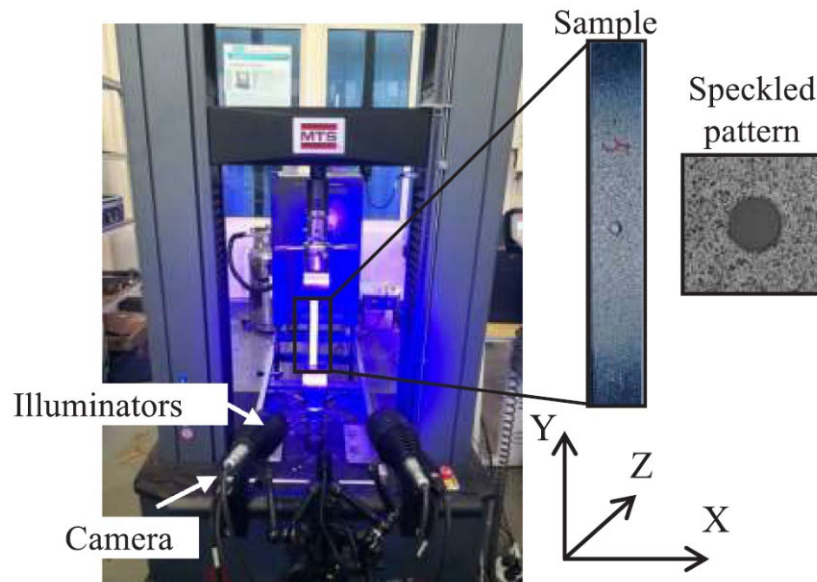
Figure 2-31. Experimental setup (Source: Li et al. (2020) with permission of Elsevier Inc, license number: 5297371279737)

Interestingly DIC techniques have also been adopted in woodcutting and loading (Matsuda et al., 2018; Mckinley et al., 2019). Matsuda et al. (2018) used the DIC technique to measure the strain distribution across the cutting zone during woodcutting (workpiece made from air-dried hinoki). The 50 mm x 5mm x 50 mm sample was machined at a varying cutting angle and cut depth but with a fixed clearance angle. The process was

observed with a KEYENCE high-speed camera, at a low frame rate of 250 fps, 2.2×10^{-3} mm/pixel and a picture resolution of 640 x 480 pixels. After the DIC processing, they were able to extract the compression ε_x, normal ε_y, and shear γ_{xy} strain.

The ballistic characterization setup is a unique design pioneered at Denver Research Institute in 1982, when Komanduri et al. (1982) used two different designs; a planning type ballistic setup and a lathe machine to investigate shear instability in steel machining. List et al. (2013) later developed their ballistic setup to study the primary shear zone in mild steel machining. As shown in Figure 2-32, the design can be split into a launch and a receiving tube; the sample is fixed to a projectile and shot in the launch tube, which must be long enough to attain a steady speed. Two cutting tools are symmetrically placed at the entrance of the receiving tube to cut the samples. They observed the process with an intensified CCD camera and microscope setup at 1024 x 1024-pixel resolution, 3.5 mm^2 observation area, and 30 mm focal length. Due to the high-speed setup, a short exposure time in micro-seconds was necessary. A snapshot of the chip cross-section at a cutting speed of 1020 m/min, allowing observation of the deformation flow pattern. The same setup was adopted by Sutter and List (2013) to study the chip formation mechanism during *Ti-6Al-4V* machining. The process was carried out with an intensified CCD 54 m/s cutting speed and 0.25 mm depth of cut.
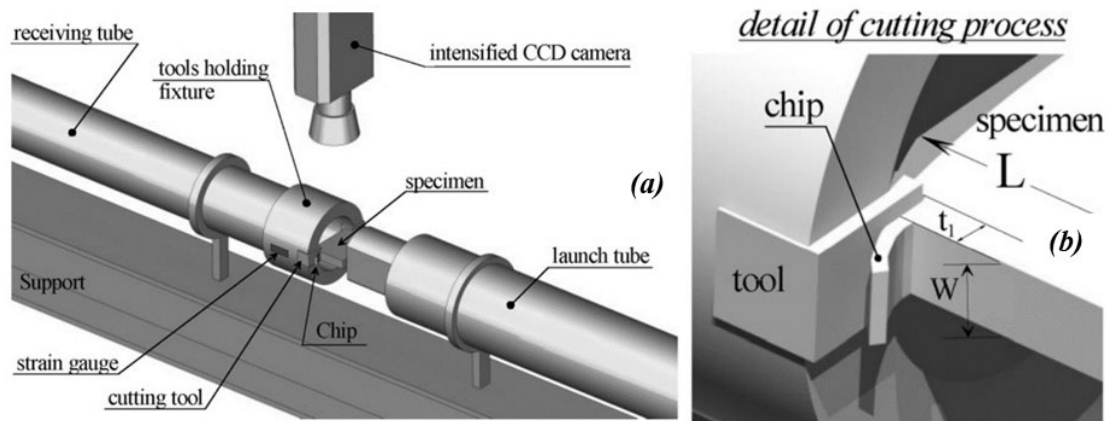
Figure 2-32. (a) Schematic diagram of the ballistic cutting setup (b) detailed view (Source: List et al. (2013) with permission of Elsevier S.A., order number: 1215824)

2.7 SMART SENSOR SELECTION

Smart sensors and instrumentation are critical driving factors of innovation for Industry 4.0 and other trends such as digital twins, smart factories, smart production, smart mobility, smart home, and smart city. Several authors have recognized and acknowledged the importance of sensors, measurement science, and smart evaluation for Industry 4.0 (KimandHwangbo, 2018; Lee et al., 2018; Wu et al., 2019). In order to effectively optimize the use of Industry 4.0 or digital process twin in manufacturing, it is crucial to understand the many technologies, particularly sensors, that enable manufacturing processes to function efficiently while using these innovations. For instance, any reliable monitoring system must be built around an efficient and, if possible, inexpensive sensorial system with fast signal processing methods and low-cost computational strategies capable of correlating measured signals with relevant information about the process's current status. Also, the adoption of sensors makes it possible to acquire information, evaluate the gathered data, and take actions based on the merged models and entities in a DPT. Also, with sensors, cloud-based IoT solutions can link the physical and virtual worlds, allowing businesses to control IoT device connection and flexibility.

The illustration in Figure 2-33 depicts an idea for a smart hybrid manufacturing system capable of performing both subtractive and additive manufacturing operations on a single platform (Kim et al., 2018).
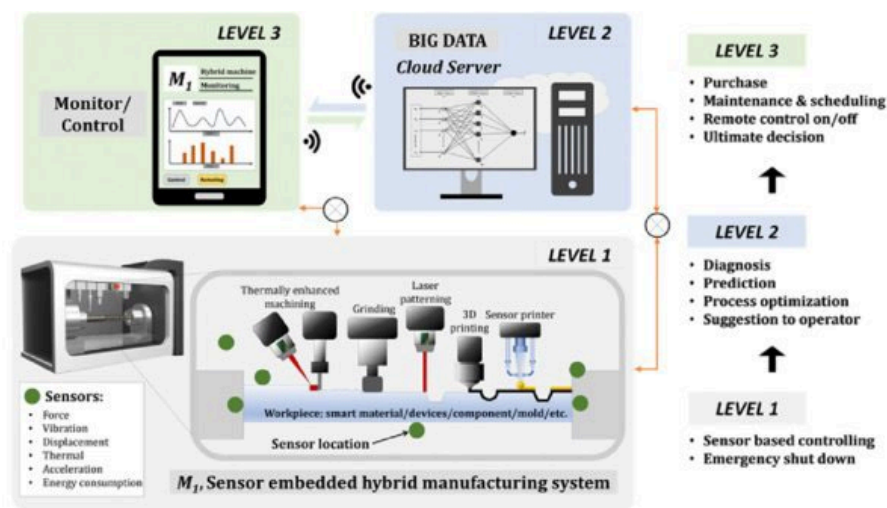
Figure 2-33. Smart hybrid manufacturing system (Source: (Kim et al., 2018) with permission of Elsevier S.A., license number: 5297380297019).

Numerous sensors, including force, vibration, displacement, temperature, humidity, acceleration, and energy consumption sensors, are incorporated into the system, providing real-time data on these variables. The common industrial practice, as highlighted in Figure 2-33 is to have as many sensors as possible installed on machine equipment or tools. Though this approach yields tons of data, it is expensive, and not all of the extracted data is useful for process monitoring and prediction. It might be best to only select sensors based on required model parameters to resolve this challenge. In this work, a model-driven sensor selection approach is considered. Only force sensors (strain gages), acoustic emission, and accelerometers were used on the lab in-situ high-speed testbed due to the required model parameters. For instance, the acoustic emission sensor can detect process-induced cracks during titanium aluminide machining. The following sub-section discusses the application of acoustic emission in crack detection and process monitoring.

2.7.1 Acoustic Emission

Existing methods focused on monitoring and analyzing the crack formation during titanium aluminide machining are post-mortem. However, since a release of energy typically accompanies crack formation, the authors propose that the crack formation in titanium aluminide machining can be monitored with an acoustic emission sensor. The extracted acoustic emission signal data can then be analyzed for pattern recognition, damage quantification, process monitoring, and control; an approach applied in various fields of study (Neupane et al., 2021; Oh and Jo, 2019; Tran and Lundgren, 2020). An informed sensor selection for process characterization is known as 'smart' or 'physics-informed' sensors and sensor data. This approach contrasts with the 'big data' methodology, which often is without physical correlation to material behavior and causal mechanisms. For accurate process characterization, it is imperative to select sensors whose data correlate to the real-world material's behavior.

Acoustic Emission (AE) involves the rapid release of energy in a structure or body undergoing loading or deformation conditions. The ability to pick the deformation stress wave frequency with a piezoelectric sensor can be traced to redistributing local strain energy associated with respective deformation conditions. They have substantial practical relevance to non-destructive testing, but they are also often used in seismology. In terms

of nondestructive testing and tool condition monitoring, the main limitation of AE is the lack of a rigid formula or set of models that can be applied to every use case, including those involving different materials and failure modes. AE is primarily a qualitative measurement tool, and other non-destructive tests or calibration/correlation trials are required to obtain quantitative feedback. However, some of the advantages of using AE for machining applications include high sensitivity, continuous online measurement, bulk volume monitoring, and pinpointing the location of damaged regions. AE signals include application functions, sensor type, propagation medium, coupling efficiency, sensor sensitivity, amplifier gain, and threshold voltage.

Additionally, the cost of testing and developing a baseline for comparison is both expensive and time-consuming. For the most part, most AE studies in machining have concentrated on machine condition and tool wear monitoring. In both approaches, relevant features such as AE energy, counts, RMS values, and count distributions were extracted and correlated with selected quality metrics. However, only a few attempts have been made to correlate the AE signals with the surface finish of the workpiece. Extracted AE signals contain process or material-specific information useful for the signal source detection, location, and severity. AE signals can be categorized under burst, continuous, and mixed signals. Burst signals are due to defect emergence during deformation.

In contrast, continuous signals consist of overlapping transients (noise included) from varying emission sources, and mixed AE signals consist of both burst and continuous signals overlaid with environmental noise. According to Terchi and Au (2001), the post-utilization of AE signals for process monitoring involves three critical steps; signal enhancement, signal separation, and signal analysis. The signal enhancement step involves the optimal removal of embedded noise, preceding the segmentation of crucial burst signals or critical events. The signal analysis subsequently attempts to identify or correlate the wave source and appropriately characterize its magnitude, severity, and propagation. The acoustic emission technique has found several studies and applications in material science research. Its scope spans damage initiation detection, dynamic loading, composite materials crack propagation, and definition of damage and fracture mechanism. The application of AE signals has focused extensively on machine and tool condition monitoring, friction analysis, and fault detection in machining. It is also a well-established

sensor for detecting fracture and fracture/deformation mode. Modern advancements in signal processing and pattern recognition analysis have driven several AE signal characterization and adoption fields in recent years.

2.8 CONCLUSIONS

Due to its intermetallic structure, titanium aluminide exhibits unique properties such as low density, high strength, high stiffness, corrosion resistance, and creep resistance. However, as reported in this section, surface integrity problems defects (such as microstructural alterations, work hardening, residual stresses, and surface cracks) are induced during the cutting of titanium aluminide alloy. This material has proven to be much more difficult to machine when compared to other alloys. Based on the literature review above, the following conclusions were deduced:

- Titanium aluminide alloys tend to work harden due to their organized microstructures and ionic limits. This behavior impacts component quality in roughness, surface integrity, and tool service life.
- The low ductility of titanium aluminides is a significant disadvantage to surface integrity. It fosters crack initiation and lamellar deformation, affecting machined components' surface integrity and fatigue strength.
- The heat generated at the cutting interface is dissipated through the cutting tool due to the low thermal conductivity, resulting in accelerated cutting-edge wear.
- Maintaining hardness and strength at temperatures between 700 and 800 degrees Celsius makes chip formation more complex, resulting in higher cutting forces and faster tool wear.

Also, based on the comprehensive review of efforts to observe cutting processes in-situ through optical and kinematic approaches provided, the following key directions of this field of study can be noted. Considering the current state-of-the-art in this field, we propose that future efforts focus specifically on realizing improved spatial and temporal resolution to enable a more detailed analysis of the highly relevant evolution of sub-surface strains and temperatures during cutting. Such efforts will require a more complex, multi-disciplinary engagement with advanced optics and lighting experts. Achieving diffraction-

limited optical performance in high-speed imaging is a non-trivial technical challenge, and most currently used setups involve very low NA (numerical aperture), optics (e.g., 2x objective magnification and 0.055 NA), along with optical magnifiers (e.g., 2-15x), which only provide 'empty magnification' and thus significantly limit the Rayleigh resolution of the obtained images. Many currently used setups leverage external lighting, which is a highly inefficient means of delivering photons to a high-speed camera sensor. Thus, excessively long exposure times are often selected, resulting in significant motion blur. Based on results in the literature and considering the well-established physics of microscope optics, coaxial illumination with lasers and ultra-high intensity LEDs can be considered the most efficient means of illuminating microscopic high-speed videos.

Recent efforts with high NA (e.g., up to 0.7 NA and 50x objective magnification) optics with long working distances have demonstrated the ability to yield true sub-micron optical/spatial resolution (Adeniji and Schoop, 2021; Schoop, 2021; Schoop et al., 2019; Schoop et al., 2021) Moreover, adequately designed coaxial illumination allows for extremely short (100s of a nanosecond) exposure times required for blur-free imaging of cutting processes at industrially relevant speeds (100s of m/s). Careful matching of high-speed camera sensors/pixels with custom lighting and optics is critical to achieving the required resolution, depth of field, and working distances to analyze machining process phenomena beyond those occurring in the primary deformation zone. In particular, we envision higher resolution in-situ characterization to offer new possibilities in detailed measurements of sub-surface (micro) strain evolution, which is required for an improved understanding of machining-induced surface integrity (e.g., sub-surface strain hardening and residual stress evolution). While much work has been devoted to studying the chip formation process, including large plastic strains and temperatures (in the primary, secondary, and tertiary shear zones), future work should focus on better elucidating how surface integrity evolves dynamically due to coupled thermal and mechanical (i.e., thermo-mechanical) effects. Encouraging results, such as that by Tausendfreund et al. (2018) point toward the tremendous potential of in-situ characterization to be efficiently leveraged. As the industry progresses towards greater use of near-net-shape manufacturing techniques such as additive manufacturing and precision casting while also driving towards more sustainable practices such as multiple product life cycles, a robust understanding of

machining-induced surface integrity is needed will only increase. In-situ characterization could serve as an excellent tool to improve this understanding, inevitably leading to new product and process innovations.

Additionally, 'multi-physics' characterization of cutting processes, e.g., optical strain measurement and thermographic temperature measurement, along with kinematic force measurement, will be vital to using in-situ characterization as an experimental tool for direct and/or inverse calibration of constitutive material models, as well as the state of variable friction and contact between the cutting tool, chip, and workpiece surface. Indeed, leveraging in-situ characterization of machining as a quasi 'materials characterization technique for machining-specific thermo-mechanical regimes' is one of the most long-standing promises and objectives of this field, with many researchers attempting to solve this problem over the years. Recent advances in camera sensors, optics, lighting, and more advanced computer algorithms (e.g., DIC and PIV) and emerging machine learning techniques for image and data analysis serve as crucial enablers towards this ambitious goal. Recent results such as those by Zhang et al. (2019) suggests that in-situ characterization may soon become an established technique for inverse calibration of constitutive material models, supporting more reliable process modeling efforts. They propose that using novel artificial intelligence algorithms to (a) analyze in-situ data more quickly and efficiently and (b) link experimentally-identified parameters to process model inputs represents a significant opportunity that deserves further study.

In conclusion, as advanced machining research is increasingly embracing more digitally-enabled technologies to enable more efficient and sustainable machining practices, the almost 100-year-old experimental tools of in-situ characterization should continue to serve as a stable foundation for identifying fundamental process physics, leveraging in-situ experimental techniques, fast and efficient calibration, and validating AI-augmented process modeling paradigms. It should yield significantly faster and more robust process models that could generate Digital Process Twins of cutting processes in the industry. A summary of technical specification for various in-situ setup and literature findings highlighted above is shown in Table 2-4.

Table 2-4. Overview of technical specification for various in-situ setup found in the literature. (Adapted and expanded from Zouabi et al. (2021) with permission of CC BY NC ND)

Material	Speed	Camera	Area of study	Chip thickn ess	Field of View	Magnific ation	Resoluti on	Pixel size (µm)	Effective Spatial Resolution (µm)	Frames per second (fps)	Exposure time (µs)	References
Brass	0.25 x 1	-	Chip formation	-	-	X25	-	-	-	-	2	Childs (1971)
Steel	1000	-	Chip formation	-	-		-	-	-	10,000	0.100	Schwerd (1935)
42CrMo 4	150/30 0	Photron Ultima APX-RS	Chip formation	0.2, 0.3	1 x 1	X12	-	20	3.33	400	1	Pujana et al. (2008)
AISI 1045	200	Imager-Intense (SensiCa mQE)	Chip formation (PDZ)	0.15	0.35 x 0.25	X25	1296 x 925	6.5	6.5	1,000,0 00	0.500	Hijazi and Madhavan (2008)
Al6061-T6	0.6	-	Large Strain Defomation	0.1	2.1 x 2.1	X3	256 x 256	8.2	5.47	250	-	Gnanamanickam et al. (2009)
42CrMo 4	30	-	Temperatur e, Plastic Strain	0.1	-	X15	256 x 128	-	-	30,000	33	Arriola et al. (2011)
Ti, Mg	0.6	pco.dima x HD	LSEM	0.2	1.4 x 1.4	-	1000 x 1000	11	-	2,000	-	Guo et al. (2012)
Ti-6Al-4V	6	FASTCA M APX RS2	Strain Field Measureme nt	0.15	0.3 x 0.3	-	128 x 128	17	-	70,000	10	Calamaz et al. (2012)
AISI101 8	1020	-	Strain and velocity fields	0.84	1.75 x 1.75	X10	1024 x 1024	1.7	-	-	-	List et al. (2013)
Ti-6Al-4V	6	Photron Fastcam APX-RS	Strain fields	0.25	0.65 x 0.6	X10	384 x 352	17	3.4	18,000	6.6	Pottier et al. (2014)

63

Brass	0.06	pco.dimax HD	Deformation fields	0.05-0.15	4.3 x 2.4	X5	1296 x 720	11	4.4	-	-	Guo et al. (2015)
Copper	6×10^{-4}	Photron SA-X2-480K-M1	Strain Modeling in LSEM	0.1-0.25	1 x 1	-	1000 x 1000	20	-	32,400	-	Cai et al. (2015)
Al7075-T6	0.35/0.5	pco.dimax HD	Stress Fields	0.1/0.15	1.68 x 0.94	X12	1920 x 1080	11	1.83	-	-	Zhang et al. (2017)
AW7020-T6	90	PCO edge 5.5	Strain	0.1	1.7 x 1.4	X10	-	6.5	1.30	-	.020	Baizeau et al. (2017)
Al6061-T6	0.1	pco.dimax HD	Velocity and stress fields	0.06/0.08/0.1	1.75 x 0.98	X12	1920 x 1080	11	1.83	1,000	-	Zhang et al. (2018a)
Ti-6Al-4V	3/15	Photron Fastcam SA3	Temperature and kinematic fields	0.25	0.58 x 0.58 / 0.43 x 0.39	X15	512 x 512 / 384 x 352	20	2.67	6,000 / 10,000	50	Harzallah (2018)
ECAE Ti	30	Photron SA-5	Strain and Strain Rate	0.1	0.5 x 0.5	X12	1024 x 1024	20	3.3	50,000	-	Davis et al. (2018)
Ti-6Al-4V, AISI 4340		Photron Fastcam SA-Z	Surface Integrity, Contact Mechanics	0.001-0.150		X50	1024 x 1024	20	0.60	50,000 - 2,100,000	0.159	(Schoop et al., 2019)
Ti-6Al-4V	8	PCO.dimax HD	Displacement, Strain, and Stress Fields	0.02	4 x 4	X12	1296 x 720	11	1.83	2,000	-	Huang et al. (2020)
AISI 4140	50 100	Photron Fastcam SA5	Friction Modeling	0.1	-	X6	1024 x 1024	20	6.67	10,000 20,000	10 6.25	Denkena et al. (2021)

Table 2-5. Summary of literature review findings

	Current Research State	Research Gaps and Future Work
Surface Integrity Modeling	• A significant amount of experimental/anecdotal studies from academia, but the lack of industrial adoption of SI modeling. • Relevant recent keynotes and reviews: Arrazola et al. (2013); Jawahir et al. (2011)	• Realistic prediction of industry-relevant quality metrics (such as surface integrity, tool-life, surface roughness, etc) • Lack of reliable and efficient predictive models connecting fundamental variables with industry-relevant quality metrics. •
		• Model-based selection of process variables (feeds/speeds). • Insufficient understanding of the machining process and physics-based modeling.
		• Hybrid analytical/numerical modeling approach. • Capability for short computational time and relevant inputs (see below).
		• Model-based analysis and optimization of surface integrity evolution. • Lack of realistic numerical and analytical model inputs (material flow stress, friction, and thermal data).
		• Model-based optimization of material/component performance, using 'machining as surface engineering process'. • Lack of understanding of the correlation between surface integrity parameters and functional performance of machined components.
In-situ Characterization	• Persistent lack of machining-specific friction and flow stress	• Efficient material characterization technique for capturing realistic strain, strain rates, and temperature values.

In-situ Characterization	data, due to lack of realistic characterization techniques • Relevant recent keynotes and reviews: Harzallah et al. (2018); Melkote et al. (2017).	• Low process speed for current/previous in situ machining test setups • Limited in-situ imaging capabilities (low frame-rates and spatial resolution)
		• Database of validated flow stress models for common alloys in machining. • Lack of accurate relationship between material flow stress and pertinent process variables. • Lack of realistic and robust process models (e.g., hybrid models)
Adaptive Machining Process Control (Digital Process Twins)	• Significant focus on forces, tool-life, and part geometry improvement; lack of surface integrity considerations, Beyond 'form, fit, function' • Relevant recent keynotes and reviews: Jones et al. (2020); Ritto and Rochinha (2020); Ulsoy and Koren (1993)	• Real-time adaptive control of machining-induced surface integrity, using process models • Limited leverage of machine learning techniques to identify process trends needed for accurate surface integrity monitoring
		• AI-enabled multi-objective adaptive process optimization (e.g., tool-life, residual stress, productivity/cost, etc.) • Lack of real-time capable process models to inform 'physics' aspect of AI optimization scheme

CHAPTER 3.

MATERIALS AND METHODOLOGY

3.1 CUSTOM IN-SITU TESTBED FOR MATERIAL CHARACTERIZATION

For many decades, much anecdotal evidence of the detrimental effects of machining-induced damage, such as grain deformation, strain hardening, and grain plucking, has been collected by industry and academia. Several papers have attempted to study the correlation between machining-induced surface integrity and product functional performance (Brinksmeier et al., 2014; Brinksmeier et al., 2018). However, despite these efforts, there remains a lack of efficient and robust models to relate machining process parameters, such as feeds and speeds, with surface damage characteristics. Significant advances have been made to promote model-based Integrated Computational Materials Engineering (ICME) in alloy design and primary and secondary processing (casting, forging, forming, joining). However, there are no industrially-viable models for predicting process-induced surface integrity (Bolcavage et al., 2014). This limitation severely affects the aerospace industry, where new and novel materials are regularly developed but with little knowledge of appropriate finish machining strategies.

The status quo for optimizing manufacturing processes across different sectors is empirical modeling due to the shortage of efficient and reliable modeling alternatives. Empirical models (EM) are the most robust and easily implementable modeling approach, which leverage the direct use of experimental trials to understand the correlation between process variables and outcomes (Arrazola et al., 2013). Experimental matrices are constructed to cover a wide range of cutting conditions, and data are analyzed using statistical methods. However, conclusions are only as robust as the experiment scope, and a poor experimental design would limit modeling accuracy. Also, this approach is quite expensive and time-consuming, as there is a need to consider different cutting conditions for a holistic understanding of the process physics.

Modeling alternatives such as numerical and analytical models are unreliable due to a lack of in-situ characterization of model inputs and long computational time. Early

efforts toward so-called in-situ characterization of machining processes can be dated to Schwerd (1935), who was among the first to study the process of chip formation during cutting. Subsequently, (StevensonandOxley) adopted more advanced characterization techniques, such as explosive quick stop device setup. The deformation to the square grids printed on the workpiece was observed after an abrupt process stop. However, most of these approaches did rely on significant post-processing and an oversimplified assumption of instantaneous 'freezing' of a steady-state deformation, as Childs (1971) later established. Since achieving an efficient and realistic process or material, characterization is critical for developing (and calibrating) robust and accurate process models. Several publications have been on this topic, including (2015; 2018; Lee et al.). However, the cutting speed range for adopted solutions is not representative of a typical machining process due to imaging and experimental setup limitations.

In 2019, (Schoop et al., 2019) reported their experimental development efforts of an improved ultra-high-speed in-situ testbed, capable of realistic process characterization up to 250 m/min cutting speed and beyond 1,000,000 fps, with standard frame rates order of 50,000 to 500,000 fps (setup shown in Figure 2-30). This unique ultrahigh-speed microscopy testbed created at the University of Kentucky was used to capture the data for most of the experiments in this work. Using the latest generation of CMOS high resolution (2 Mpx), ultra-high-throughput (16 Gpx/sec) sensor technology (iX cameras i-speed 726), combined with a custom-built ultra-high intensity LED liquid light guide (>250 million lux), the system is capable of obtaining nanosecond exposure microscopic images at realistic cutting speeds (vc = 50-250 m/min) and frame rates up to 1,000,000 frames per second. In this scenario, the ultra-high-speed camera is coupled to a high-resolution video microscope produced by Mitutoyo (VMU-V), as shown in Figure 3-1, which can be utilized consistently at magnifications of up to 50 times. When optical (Raleigh/diffraction) and sensor (Nyquist/sampling) restrictions are taken into consideration, the maximum spatial resolution of the system is roughly 550 nm, which corresponds to the wavelength of visible light (550nm). This allows for the resolution of very tiny strains and extremely high strain rates, up to 108. At the same time, extremely high stresses, up to a factor of 10,000 percent, may be resolved with digital image correlation software (DIC) written in Matlab. However,

it is worth noting that the adopted setup was not designed with lubrication or cooling capability, thereby the experiments were limited to dry machining.
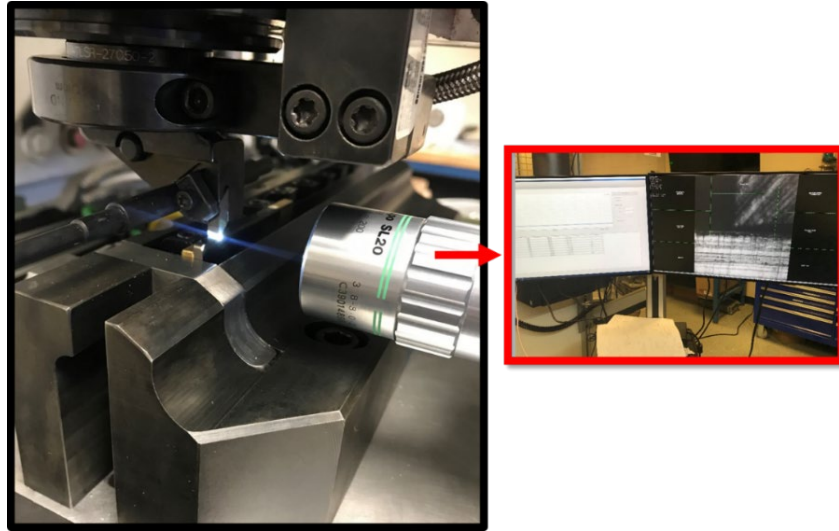
Figure 3-1. A zoomed-in view of the experimental set-up.

The ultra-high-speed microscopy system is combined with a high-speed linear stage capable of more than 5 Gs of acceleration and peak speeds of 4 m/s and 50 nm absolute encoder feedback to allow in-situ creation of a very detailed picture sequence in the laboratory. The use of DIC to analyze these sequences reveals complex strain and strain rate fields, which can then be correlated with synchronized force, vibration, thermal, and other data collected using a variety of sensors such as high-resolution strain gages, accelerometers, infrared pyrometers, and thermocouples, among other things. The custom-developed testbed allows for extensive characterization of dynamic material behavior throughout the machining process over a wide range of physical characteristics and domains. A key goal was to use the machining/finishing process as a more accurate material property characterization approach, accomplished via careful design.

3.1.1 Machining Deformation Zones

Different zones characterize the metal cutting process, the most commonly cited ones being the Primary Deformation Zone (PDZ), the Secondary Deformation Zone (SDZ), and the Tertiary Deformation Zone (TDZ). Among these three, only the TDZ is most closely related to the field of surface integrity. Figure 3-2 provides a schematic overview

of the five total zones identified by (Schoop et al., 2019), overlaid on a real in-situ optical micrograph obtained during the cutting of Inconel 718 at a cutting speed of 70 m/min. The primary shear zone occurs along the shear plane formed due to the contact between the cutting tool edge and the uncut chip, while the secondary shear zone occurs along the tool rake face due to the rubbing interaction between the formed chip and tool rake face. The tertiary shear zone, which has been scarcely studied, is formed due to the contact between the tool flank face and the workpiece surface. The rubbing interface generates heat and induces a significant proportion of the temperature observed in the workpiece sub-surface. The subsequent sections of this work will highlight studies across these three zones.
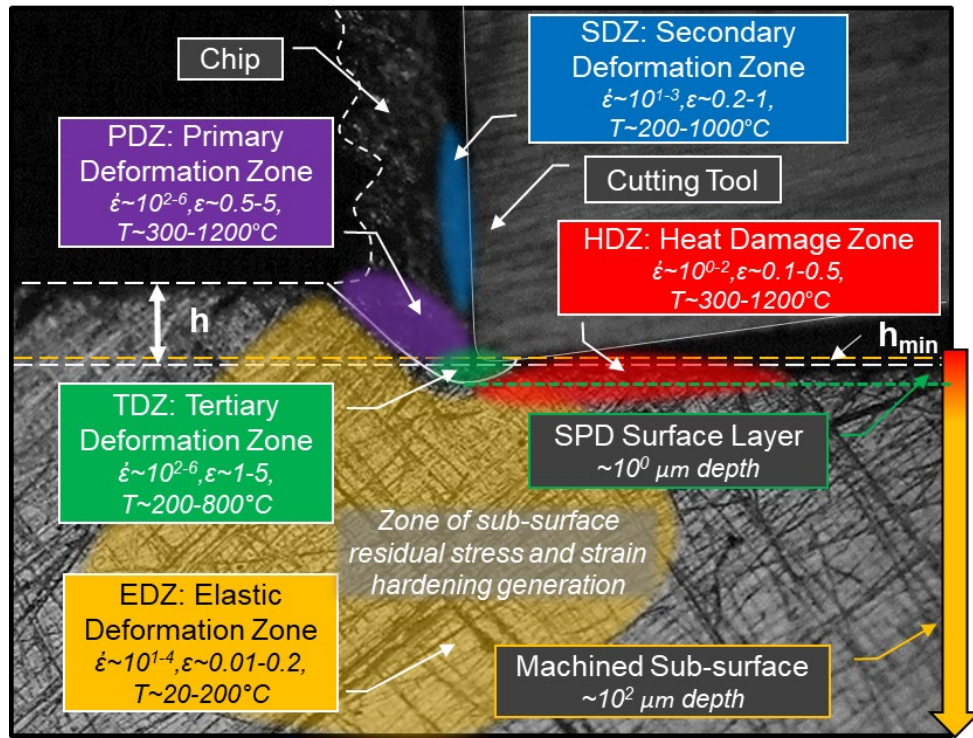
Figure 3-2. Schematic overview of the various zones of deformation that characterize metal cutting operations.

As seen in Figure 3-2, two additional zones were proposed, the Elastic Deformation Zone (EDZ) and the Heat Damage Zone (HDZ); both are particularly relevant to the surface integrity study. Notably, neither of these zones has received much attention, primarily attributed to the technical challenges of obtaining in-situ data from these tough to observe zones of the workpiece sub-surface region. Strain in the EDZ and HDZ is relatively small (less than 0.1 in almost all cases) and is accumulated in a complex and

infinitesimal/incremental loading/unloading cycle. In contrast, measurement of the considerable strain within the PDZ is readily achieved even with limited spatial and temporal resolution (i.e., using limited magnification and relatively low frame rates).

With the ultra-high-speed in-situ characterization testbed, fundamental process-specific material properties of gamma titanium-aluminide (γ-*TiAl*) low-pressure turbine (LPT) alloy would be characterized in both cutting (machining) and severe plastic deformation (burnishing) regimes with continuous acquisition mode at previously unattainable temporal (159ns) and spatial (500nm) resolution. Samples were processed into test coupons via electric discharge machining (EDM) and low-stress grinding and polishing (~3mm width strips of 100-200mm length and 20-60mm height).

The multi-sensor plane-strain (2D) in-situ characterization approach captures optical, kinematic, and thermal data to unambiguously characterize and calibrate the workpiece material's process-specific behavior across four relevant physical locations domains (elastic, plastic, thermal, thermodynamic). Outlined trials for a limited but tailored experimental work are shown in Table 3-1. Proposed experimental trials would evaluate 'extremes' during in-situ testing to cover the range observed in production. The experiment would consist of two types of cutting tools, a carbide (K68 grade) and a polycrystalline cubic boron nitride tool. As shown in Table 3-1, the cutting speed, uncut chip thickness, and tool wear varied regarding the desired regime and realistic machining conditions.

Table 3-1. Experimental matrix for in-situ characterization of γ-*TiAl* machining.

Tool Material	Cutting Speed (m/min)	Uncut chip thickness (μm)	Tool Wear (μm)
Carbide (K68)	25	0-20um	Unworn
PcBN (low binder micro grain)	50, 100, 150	Near h_{min}	50, 100, 150
Permutations	2	4	2	4

Also, the proposed technique integrated both optically measured strain and cutting force data. Titanium aluminide block samples were processed into test coupons via electric discharge machining (EDM) and low stress grinding and polishing (~3mm width strips of 100-200mm length and 20-60mm height).

Table 3-2. Hand Polishing recipe for γ-$TiAl$ alloy

Polishing Pad	Abrasive	Base Speed (RMP)	Time (min: seconds)	Comments
180 Grit SiC Paper	Water: low amount	300	Depends	Keep polishing until the majority of samples appear in the same plane.
220 Grit SiC w/ MD Gekko	Water: low amount	300	Depends	
500 Grit SiC w/ MD Gekko	Water: low amount	300	Depends	
1200 Grit SiC w/ MD Gekko	Water: Low Amount	300	Depends	
MD-Largo	9µm diamond	150	10:00 – 20:00	Run closer to the center of the pad.
PolyPAD	3 µm diamond	150	10:00 – 20:00	
TRICOTE	1 µm diamond	150	10:00 – 20:00	
TRICOTE	0.5 µm diamond	150	10:00	
TRICOTE	0.02 µm colloidal silica/OPS	150	04:30	Run water and continue polishing for 30 seconds immediately after the 4-minute mark to wash away the reacted layer of material.

The polishing procedure/recipe is described in Table 3-1, and Figure 3-3 shows a good microscopy result obtained without etching. The microscopy images clearly show the sample microstructure (γ-phase grains), a prerequisite for a quality in-situ characterization. The microscopy result can be further improved by etching the samples.
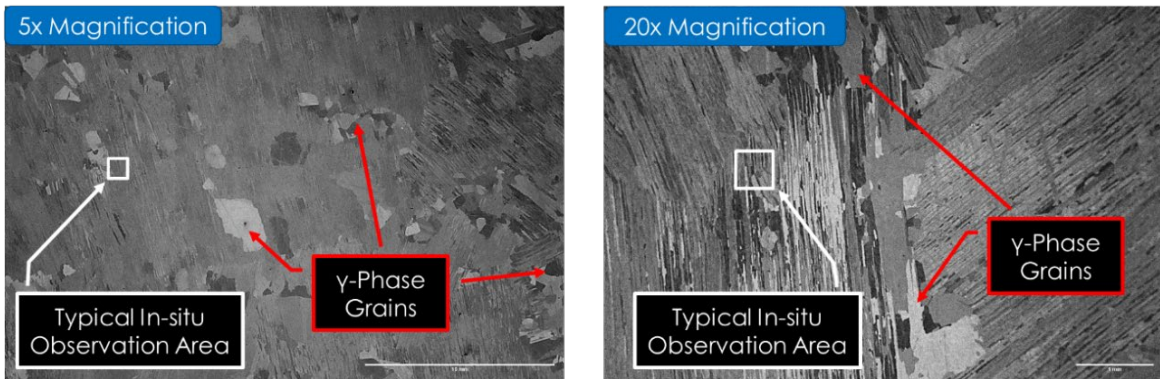
Figure 3-3. Near lamellar γ-*TiAl* microstructure captured after polishing recipe

The cutting tool edge geometry significantly impacts the cutting process and machined product's functional performance. This edge geometry does not remain constant during a cutting process due to necessary metal-to-metal contact between the tool and the workpiece leading to wear/degradation of the tool edges. The tool edge geometry changes affect the thermo-mechanical properties, influencing the surface integrity factors. Its wear rate and pattern hugely depend on the machinability of the workpiece and cutting tool material. The carbide tools used for the experimental work were prepared for different edge geometries using the process described in Figure 3-4. A custom experimental tool holder setup was assembled. The cutting tool edge was diamond grinded on a polishing machine to bring the edge to a rough geometry. A final step of micron-graded diamond film lapping was used to bring the tool edge to the desired geometry and flank wear.
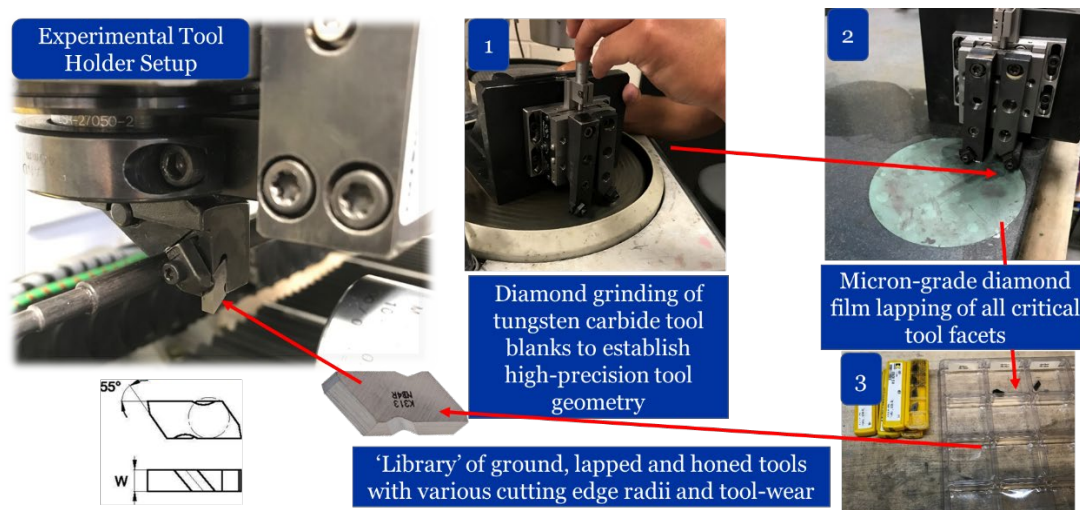
Figure 3-4. A figure of the cutting tool edge preparation process

3.1.2 Force Measurement

The primary cutting stroke (1 m travel length), powered by a proprietary linear servo motor by Yaskawa (experimental series SLGFW2), can achieve up to 4.2 m/s (~250 m/min) travel speed with 5Gs of acceleration and a peak force above 5 kN. The vertical axis, which controls the uncut chip thickness in 2D cutting (which could also be considered the depth of cut or feed), features positional repeatability of better than 0.4 microns. Integrated foil strain gauges capture cutting forces (Futek LLB300 series), which typically achieve better than 0.2 N force measurement accuracy at a sampling bandwidth of 50 kHz (Futek's IAA300 differential amplifier). A high natural frequency (beginning at 21.0 kHz and increasing up to 58 kHz) is delivered by the sensor, which results in a rapid reaction time that improves accuracy and reduces cycle time. Furthermore, the high rigidity of the sensor contributes to its accuracy by allowing for very low deflection, which may be measured in increments as small as 0.0003" (0.0076 mm). Aside from that, specific design and manufacturing touches improve the sensor's performance even further, such as a highly tailored strain element that significantly minimizes the number of solder connections, thereby enhancing the sensor's dependability and durability.

3.1.3 Acoustic Emission Measurement

For this study, the acoustic emission signals were collected using an AE sensor by KISTLER, model 8152C with 5125C AE coupler, featuring a bandwidth of 100-900 kHz, was used along with a National Instruments USB-6361 data acquisition system (DAQ), featuring a peak sampling rate of 2 Ms/ch. The AE sensor was integrated into the cutting tool holder using a rigid M6 screw connection per the manufacturer's specification to maintain constant signal attenuation during cutting. The distance of the AE sensor to the cutting tool tip was approximately 20mm, with the solid steel tool holder shank (grade AISI 4350) separating the tungsten carbide cutting insert (NB2R geometry, K68 grade) and AE sensor. It comprises the sensor housing, the piezoelectric sensing element, and the built-in impedance converter referred to as the AE-Sensor. The piezoelectric ceramic sensing element is set on a thin steel diaphragm, which acts as a mechanical coupling. The sensitivity and frequency response of the sensor is determined by the way it is constructed.

A little protrusion is visible on the coupling surface of the diaphragm welded into the housing, which is used to measure the AE signals. Consequently, a precisely specified coupling force is produced during mounting, ensuring that the AE transmission has a steady and repeatable coupling throughout. As a result of the design, the sensing element is acoustically separated from the housing and provides excellent protection against external noise.

3.1.4 Displacement and Strain Measurement

The two standard techniques for extracting the strain deformation field from captured process images are Digital Image Correlation (DIC) and Particle Image Velocimetry (PIV). Digital Image Correlation (DIC) is a non-contact technique used in measuring 2D and 3D material deformation through image tracking and registration. The deformation quantification is achieved by correlating two or more captured images, representing the before (reference) and after (current) deformation state of the observed region/workpiece.

The underlying physics is based on subset-based tracking, whereby the area of interest is subdivided into about $n \, x \, m$ pixels regions, commonly referred to as subsets. Subsets from both reference and current images are chosen for correlation via measurement of their local displacements in the x and y directions. To achieve accurate and precise matching, the subset selected must contain appropriate variations in intensity to ensure that it can be classified uniquely and reliably in the deformed picture. The surface to be examined must be dotted with natural or artificial speckles pattern (or, more precisely, the strength of random gray level fluctuation). Hence, researchers often painted the sample's area of interest with random paint speckles before deformation for efficient image tracking. As shown in Figure 8, Equation 2 and 3, the initial point (x, y) from the reference image can be mapped to the point (x^*, y^*) on the deformation image, then the center translations (u, v) of the sub-image in the $X \, and \, Y$ directions can be evaluated using the Taylor Series.

$$x^* = x + u(x, y) \tag{2}$$

$$y^* = y + v(x, y) \tag{3}$$

75
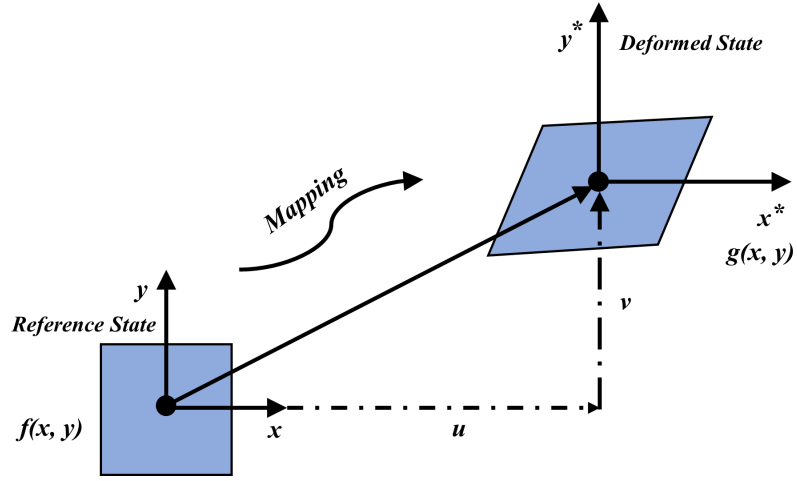
Figure 3-5. Schematic figure of reference and current subsets in DIC

To compare and match the process images, correlation criteria such as cross-correlation criterion, squared sum differences criterion, and the sum of absolute differences criterion. Also, since the reference and deformed images' intensity are different (since they are captured at various locations), it is essential to account for variations using correlation criteria such as the Zero-Normalized Square sum of Differences Criterion (ZNSSD). The correlation coefficient C between the subset pixels of the two successive images can be calculated using a fast Fourier transformation as shown in Equation 6, with $f(x, y)$ and $g(x^*, y^*)$, representing the grayscale values for reference and deformed state (Tong, 2018).

$$x^* = x + u + \frac{\partial u}{\partial x}\Delta x + \frac{\partial u}{\partial y}\Delta y + \frac{1}{2}\frac{\partial^2 u}{\partial x^2}\Delta x^2 + \frac{1}{2}\frac{\partial^2 u}{\partial y^2}\Delta y^2 + \frac{\partial^2 u}{\partial x\partial y}\Delta x\Delta y \qquad (4)$$

$$y^* = y + v + \frac{\partial v}{\partial x}\Delta x + \frac{\partial v}{\partial y}\Delta y + \frac{1}{2}\frac{\partial^2 v}{\partial x^2}\Delta x^2 + \frac{1}{2}\frac{\partial^2 v}{\partial y^2}\Delta y^2 + \frac{\partial^2 v}{\partial x\partial y}\Delta x\Delta y \qquad (5)$$

$$C = \frac{\sum_S f(x, y) g(x^*, y^*)}{\sqrt{\sum_S f^2(x, y) \sum_S g^2(x^*, y^*)}} \qquad (6)$$

Where, $\frac{\partial u}{\partial x}$ and $\frac{\partial v}{\partial y}$ represent the normal strains, $\frac{\partial v}{\partial x}$ and $\frac{\partial u}{\partial y}$ represents the shear strains, Δx and Δy represent the distance from the reference subset center to a similar point on the deformed image subset. The displacement and strain fields can either be reduced or interpolated to form a "continuous" displacement/strain field. Each subgroup's

displacement and strain information is computed using the first and second-order transformations. The result is a grid containing displacement and strain information to the reference configuration, referred to as Lagrangian displacements/strains.

While the DIC technique has enabled reduced computational time and accurate deformation measurement, its application in machining has been limited to two-dimensional image correlation due to the focus of existing experimental setups on in-plane deformation. Also, the limitation of the subset-based DIC technique includes (1) the presence of unwanted pixels around the area of interest boundary (2) for specimens with geometric discontinuities; the subset-based DIC technique is likely to produce erroneous measurements (Pan, 2011). The camera quality, lighting source, and out-of-plane movement have also been identified as significant sources of error when adopting the DIC technique (Hoult et al., 2013; Siebert et al., 2007), and attempts have been made to quantify the number of uncertainties involved (Badaloni et al., 2015; Balcaen et al., 2017; Wang et al., 2012b; Zappa et al., 2014). Hence, this technique's accuracy depends on the experimental setup, image quality, and workpiece surface/speckle pattern. The DIC technique has seen application beyond machining across subject topics such as vibration analysis (Beberniss and Ehrhardt, 2017; Helfrick et al., 2011; Wang et al., 2012a), tensile tests (Tung et al., 2010; Wang et al., 2010; Wattrisse et al., 2001), and biomechanics (Palanca et al., 2015; Palanca et al., 2016). Figure 3-6a and b show the captured process images (for reference and deformed state) from a tensile loading experiment. At the same time, the displacement output after applying two different DIC methods is displayed in Figure 3-7a and b.
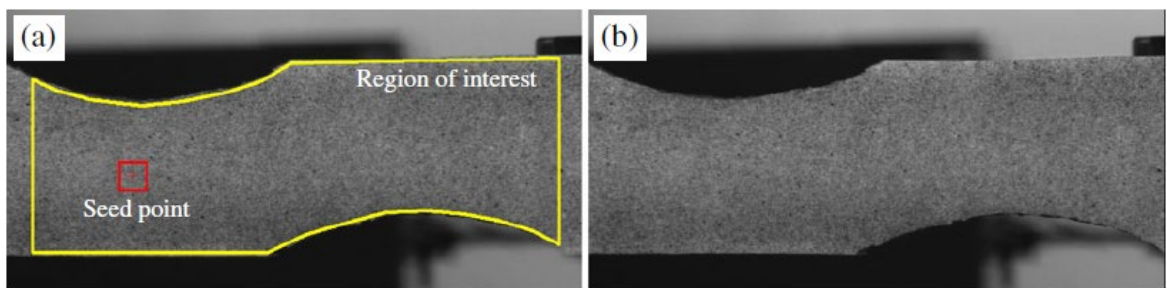
Figure 3-6. Experiment tensile loading images (a) reference image, (b) deformed image, (Source: Pan (2011) with permission of Elsevier S.A., license number: 5297380778601)
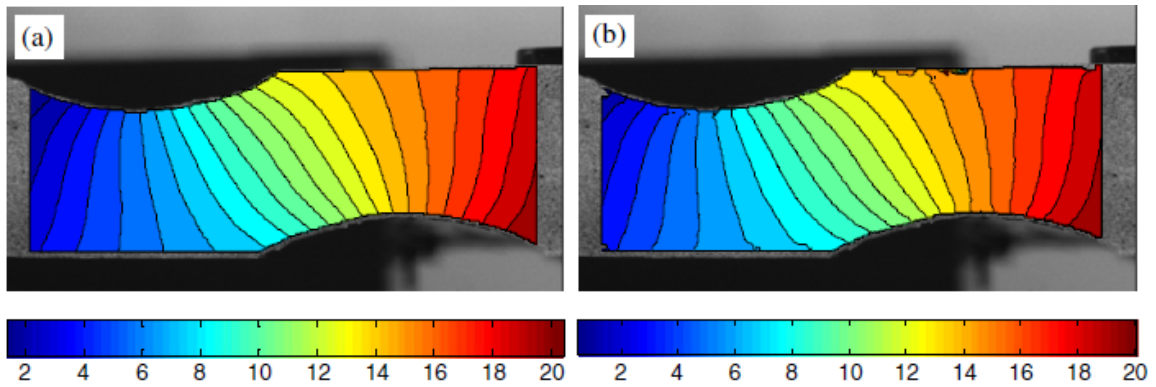
Figure 3-7. DIC displacement field output for (a) custom technique (b) subset-based DIC technique (Source: Pan (2011) with permission of Elsevier S.A., license number: 5297380778601)

The PIV technique is used to compute the 2D velocity field in a fluid flow at a high spatial resolution by seeding the fluid particles and taking snapshots of the fluid flow. The images are discretized into different sections, and the seeded particles are tracked to obtain the particle displacement over the time frame. As shown in subsequent sections, the PIV technique has been extensively applied across various machining studies (Denkena et al. 2021; Guo et al., 2012; Lee et al., 2006; Meinhart et al., 1999). The images must be in the right sequence for DIC and PIV analysis for an accurate result. DIC is often preferred to PIV at low to moderate cutting speed and in serrated chip studies (Harzallah, 2018); however, it requires unblurred images, which are challenging to obtain at high cutting speeds.

3.2   SCANNING WHITE LIGHT INTERFEROMETRY

Surface roughness and surface porosity are critical in determining the quality of a machined surface of porous tungsten, measured in microns. R_a = 0.8 µm is the current industry standard for average surface roughness. A value of 32 µin is comparable to Ra = 0.8 µm. Surface roughness may be measured in various techniques, the most frequent optical comparisons using a set of standardized samples and profilometry (profiling). The latter approach probes the surface of a machined sample using a stylus with a tiny radius tip, as opposed to the former. Profilometry can not provide highly accurate surface roughness data for finely polished surfaces (R_a < 1 µm) because no feature smaller than the

stylus tip radius can be identified. An initially sharp stylus will undergo wear due to the initial sharpness of the stylus. The Ra of machined porous tungsten samples, as measured by a non-contact approach, was determined as a result. This was accomplished using a Zygo NewView 7300 scanning white-light interferometer (SWLI) with 20x and 50x objectives, which Zygo manufactured. SWLI digitizes 3D surfaces with nanometric accuracy (±5 nm) by scanning the sample vertically and capturing interference fringes to create a point cloud of data that can be assembled.

Surface roughness measurements of machined porous tungsten were collected at three different percentages of the sample's radius, in the same way as surface porosity measurements were taken. Ten evenly spaced measurement lines were obtained from each tested area to get a statistically significant average value for Ra and the dispersion over a particular surface from the three measured regions. Because of the porosity of the workpiece material, the surface roughness of the workpiece cannot be easily compared to the surface roughness of the corresponding dense material. Although this is impossible, a qualitative comparison of samples machined with various settings is possible. This was partly due to the high number of measurements obtained from each sample, which allowed the average roughness for a specific sample to be more consistently repeatable than 0.05 mm. Cutting edge radii measurements were taken similarly to surface roughness measurements. At a magnification of 50x, different locations along cutting edges or objects of interest were photographed. Figure 3-8 summarizes the most common uses of SWLI during this study.
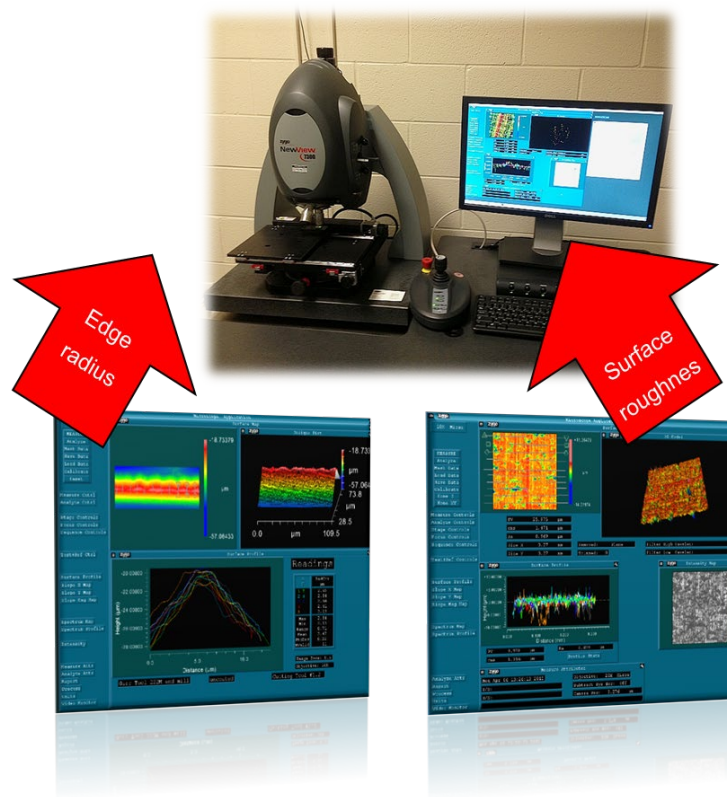
Figure 3-8. Overview of most commonly used applications of Zygo NewView 7300 3D profiler. Top image shows the instrument, which uses a laser to create nanometrically accurate point clouds of interference fringe data. Edge radius and surface roughness measurements were performed on the same instrument yet analyzed with specialized applications, shown in the bottom two images.

CHAPTER 4.

SENSOR-BASED IN-SITU CHARACTERIZATION OF *TiAl* MACHINING

4.1 SCOPE AND INTRODUCTION

Pioneering works on the real-time characterization of machining processes goes as far back as the 1960s (Oxley, 1961; Palmer and Oxley, 1959; Roth and Oxley, 1972; Stevenson and Oxley, 1969). The advancement of sensors and imaging equipment has made this approach gain significant ground. Its application has evolved to different material alloys and machining conditions. To achieve a realistic, accurate, and economical process characterization, the adoption of low-cost sensors and transducers such as acoustic emission sensors, strain gages, and accelerometers have been widely accepted. A well-positioned sensor can accurately detect process variables and extract relevant data necessary for fault detection or monitoring.

Considering the difficulty (formation of surface cracks) associated with titanium aluminide machining, several studies have investigated post-mortem factors influencing crack formation. However, there is a gap regarding the in-situ/real-time investigation of *TiAl* machining process. The current gap in the real-time characterization of titanium aluminide is primarily due to the shortage of an experimental setup capable of extracting needed process variables and data. This chapter leveraged the recently developed, ultra-high-speed in-situ characterization testbed to study cutting and severe plastic deformation processes in continuous acquisition mode at previously unattainable temporal (159ns) and spatial (500nm) resolution. Figure 4-1 summarizes the approach to capturing multi-sensory measurements (optical, kinematic, thermal) via ultra-high-speed microscopy (2.1 million frames/second), dynamometers, strain gauges, dynamometers, accelerometers, acoustic emission devices, thermocouples, infrared imaging, and servo motor controller data to yield the process-specific data across four relevant physical domains (elastic, plastic, thermal, and thermodynamic).

Figure 4-1. Overview of multi-sensory in-situ testbed characterization domains and associated measurement.

This chapter will look into achieving a precise range of machining parameters for both orthogonal cutting and milling of γ-*TiAl* alloy with carbide cutting tools. Relevant data such as the force, strain, and acoustic emission signal data extracted from the in-situ characterization testbed described in Chapter 3 and the influence of the chip thickness will be discussed in this chapter.

4.2   IN-SITU PROCESS CHARACTERIZATION

4.2.1   High-Speed Imaging of γ-*TiAl* Orthogonal Cuts

The in-situ testbed developed at the University of Kentucky can capture high-speed images of orthogonal machining cuts. The Photron FASTCAM SA-Z captures high-definition digital pictures at ultra-fast speeds, allowing detailed observation and understanding of processes. The FASTCAM SA-Z employs Photron's patented CMOS image sensor technology that combines fast recording speeds with exceptional light sensitivity and picture clarity to deliver today's most adaptable ultra-high-speed digital camera. It delivers the maximum imaging performance with megapixel picture resolution at frame rates up to 21,000 frames per second (fps) using its very light-sensitive image sensor (monochrome ISO 50,000) with a 12-bit dynamic range, frame rates in excess of 2 million frames per second at decreased picture quality, as well as shutter speeds as fast as 159 nanoseconds. The camera body design uses heat-pipe technology, resulting in a thermally stable and dependable high-speed imaging system appropriate for usage in the

most demanding conditions. This camera has standard operating features such as a mechanical shutter for remote system calibration, a dual-channel Gigabit Ethernet interface for quick picture download, and internal memory card drives for image download and storage on low-cost removable recording media. The system also has memory segmentation, allowing recording in one memory partition while downloading a prior recording in another. To remotely turn off cooling fans to prevent vibration while recording at high magnifications. Figure 4-2 shows the in-situ image captured at a cutting speed of 120 m/min, 70 μm chip thickness using a 10x microscope objective on a Photron FASTCAM SA-Z camera. Extracting high-resolution machining microscopic images makes it possible to apply digital image correlation on such images for severe plastic deformation, sub-surface, strain, and strain rate characterization.
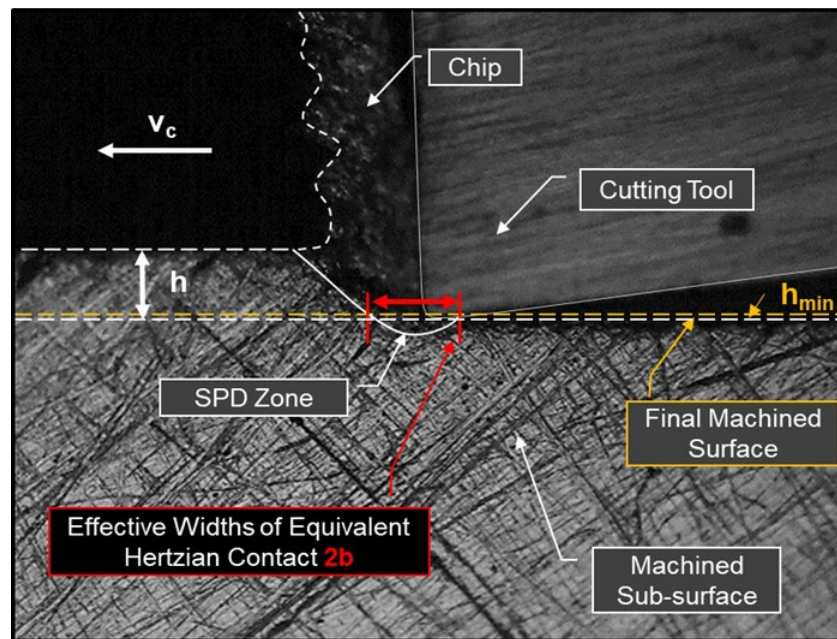
Figure 4-2. Captured in-situ image at 10x objective magnification, 159 nanosecond exposure, speed = 120 m/min, uncut chip thickness = 70 μm.

Figure 4-3 shows the high-speed image of an orthogonal cut of titanium aluminide alloy at a 60m/min cutting speed, 20x objective, 200 kfps, 318 ns exposure, and 0.003mm chip thickness using a sharp carbide cutting tool. This set of cutting parameters gives a ductile cutting mode. However, a slight change in the cutting tool edge geometry was observed to cause 'chip squeezing' during machining. The experimental trials show that it

is possible to avoid thermal cracks with an appropriate selection of feed and speed using a sharp or worn tool.
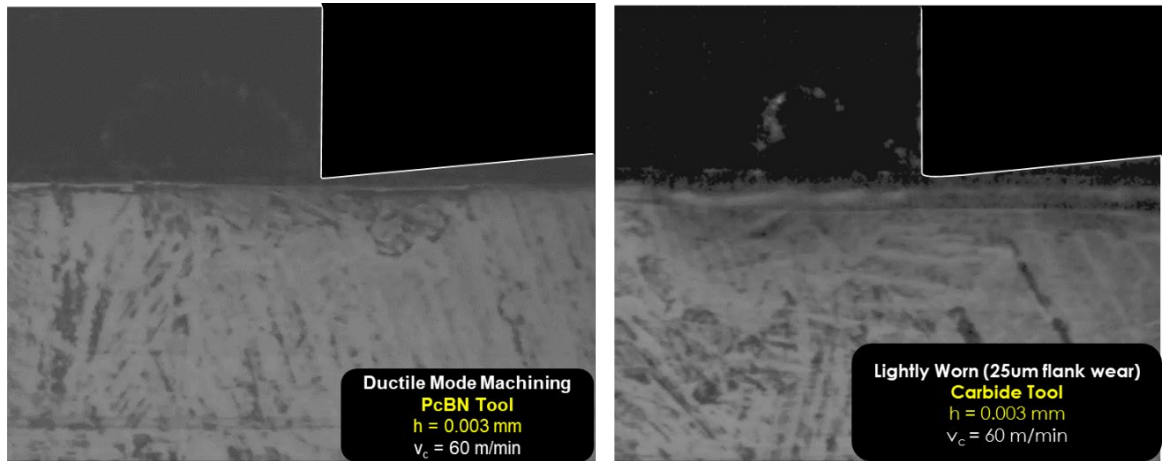
Figure 4-3. High-speed images from the orthogonal cutting of titanium aluminide alloys at 0.003 mm chip thickness and 60 m/min cutting speed.

4.2.2 Digital Image Correlation

Since resolutions of 1/100th of a pixel may be attained with good optics and illumination, digital imaging methods (such as DIC) have been widely used for the investigation of displacements and stresses. While most research has been on continuous flow (finite/large strain) across the primary and tertiary deformation zones, DIC may also be used to investigate nanometric sub-surface deformations, which are critical to developing surface integrity (e.g., RS and sub-surface strain hardening measurement). This study used an open-source 2D digital image correlation program in MATLAB, called Ncorr, to estimate the strain and strain rate values. Also, a two-pass approach initially developed by Tausendfreund et al. (2018) was used to examine the subsurface deformation field. An initial subsurface image with the cutting tool just slightly above the workpiece was captured, followed by another shot during the machining of the workpiece where the cutting tool is fully engaged on the machined surface. The two images were then passed into the ncorr application. The objective is to achieve some kind of one-to-one correlation between material spots in the reference (initial undeformed image) and current (subsequent deformed picture) configurations. DIC does this by taking tiny pieces of the reference picture, known as subsets, and calculating their placements in the present configuration.

We acquire displacement and strain information for each subset through the transformation used to match the subset's position in the present configuration. In the reference design, many subsets are chosen, generally with a spacing parameter to decrease computing expense (also note that subsets typically overlap). The ultimate result is a grid with displacement and strain information relative to the reference configuration, commonly known as Lagrangian displacements/strains. To generate a "continuous" displacement/strain field, the displacement/strain fields may be decreased or interpolated.
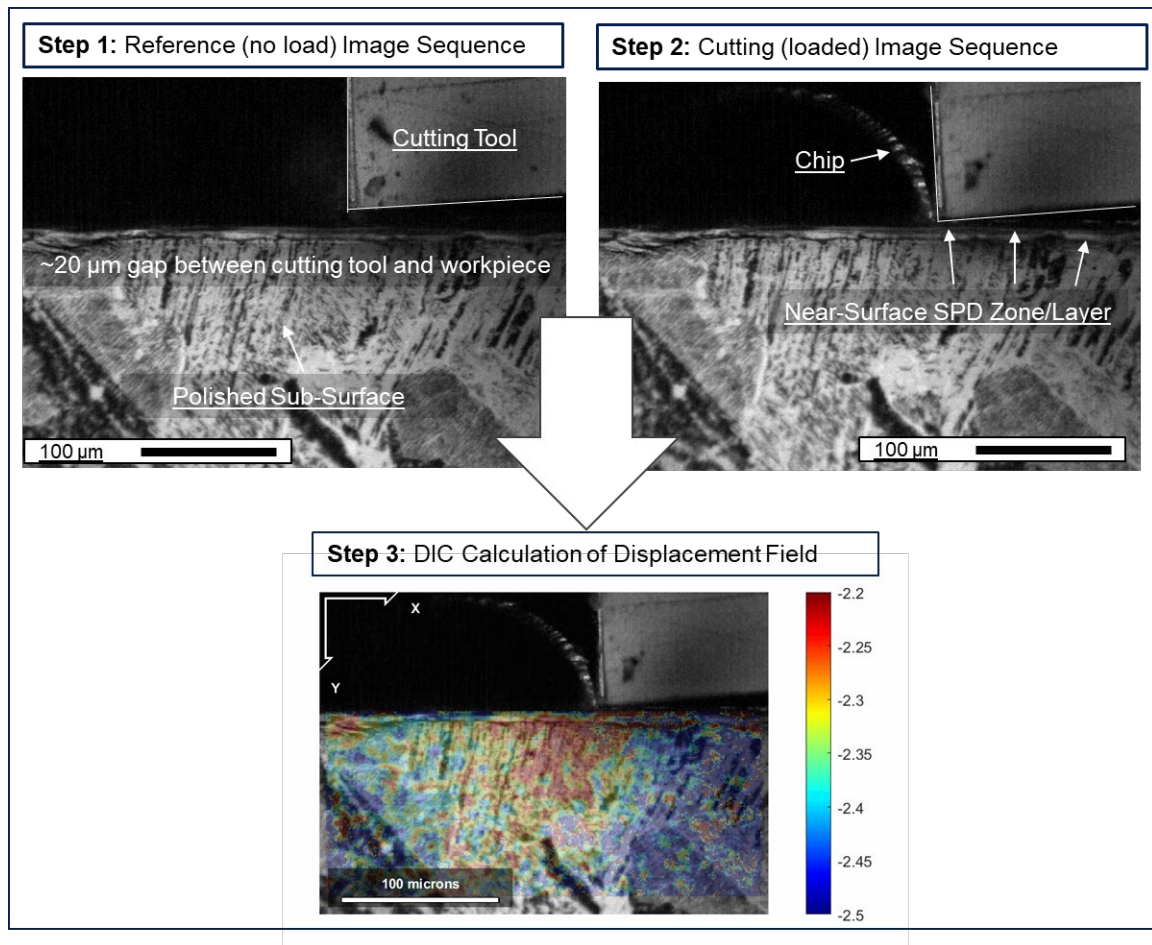
Figure 4-4. Digital image correlation steps and final displacement field.

By locating the exact point of the workpiece material spring back (i.e., the point at which the workpiece material exists, the flank face at the height of h_{min} above the bottom of the tool tip), and finding the horizontal intersection of this streamline with the beginning of sub-surface plastic deformation in the SPD zone (severe plastic deformation), as

illustrated in Figure 4-4. Likewise, the equivalent contact width in cutting may be determined by finding the shear plane angle and projecting a right-angle line towards the sub-surface ahead of the cut. It was found that grain pullout/cracking occurred preferentially when *TiAl* lamellae were approximately perpendicular to the shear plane, i.e., when mechanical loading was applied along the weakest direction of the microstructure.

4.2.3   Cutting Forces

The orthogonal cutting experiments were carried out on the custom in-situ testbed developed at the University of Kentucky, as described in Chapter 3. On the testbed, integrated foil strain gauges were used to capture cutting forces (Futek LLB300 series), which typically achieve better than 0.2 N force measurement accuracy at a sampling bandwidth of 50 kHz (Futek's IAA300 differential amplifier). The experimental matrix ranges from 1 to 21µm chip thickness, 60 m/min cutting speed, sharp tool (carbide and PCBN), and worn tool (25, 50, and 150µm VB). Three values were recorded and averaged for each force measurement to obtain a meaningful number. The reported scatterplot comprises the spread between the maximum and minimum of the five force values and uncertainty of ±5%, representing the inherent inaccuracy of the foil strain gauge itself.

The cutting and feed force data were captured for 3, 5, 7, 9, 14, and 21 µm chip thickness at 60 m/min cutting speed for three separate trials. Figure 4-5 shows the plot of the average cutting force and respective chip thickness for different cutting tools and tool edge geometry. From Figure 4-5, it is observed that the cutting force magnitude increases proportionally with chip thickness and tool edge radius. Also, the data profile for both the sharp carbide and sharp PCBN tool is similar. This result is similar to findings from existing literature (Aspinwall et al., 2005; Mantle and Aspinwall, 1997; Mantle and Aspinwall, 2000). The maximum chip thickness was restricted to 21µm due to the poor surface integrity of the machined surface beyond this value. This observation is due to the brittle nature of titanium aluminide alloys and the corresponding increase in cutting forces with respect to the chip thickness.
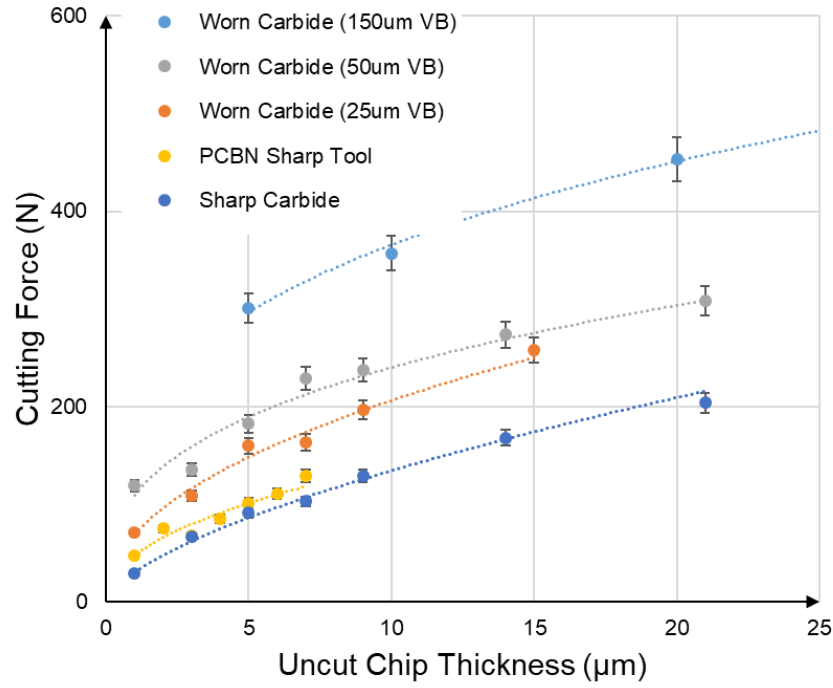
Figure 4-5. Cutting force against chip thickness for different cutting-edge geometry and cutting tool types.

4.2.3.1 Force Data Analysis

The force data extracted from the in-situ testbed were analyzed for further deductions. The cutting and feed force data were captured for 3, 5, 7, 9, 14, and 21μm chip thickness at 60 m/min cutting speed for three separate trials. Figure 4-5 shows the plot of the average cutting force and respective chip thickness for different cutting tools and tool edge geometry. The specific feed, k_c and cutting force, k_f are calculated for respective chip thickness as shown below;

$$k_c = \frac{h}{2.97 \times F_c \times 0.001} \tag{7}$$

$$k_f = \frac{h}{2.97 \times F_f \times 0.001} \tag{8}$$

The coefficient and exponent on the log-log plot in Figure 4-6 were recorded and used to generate the cutting and feed force coefficient empirical model as a function of the flank wear.
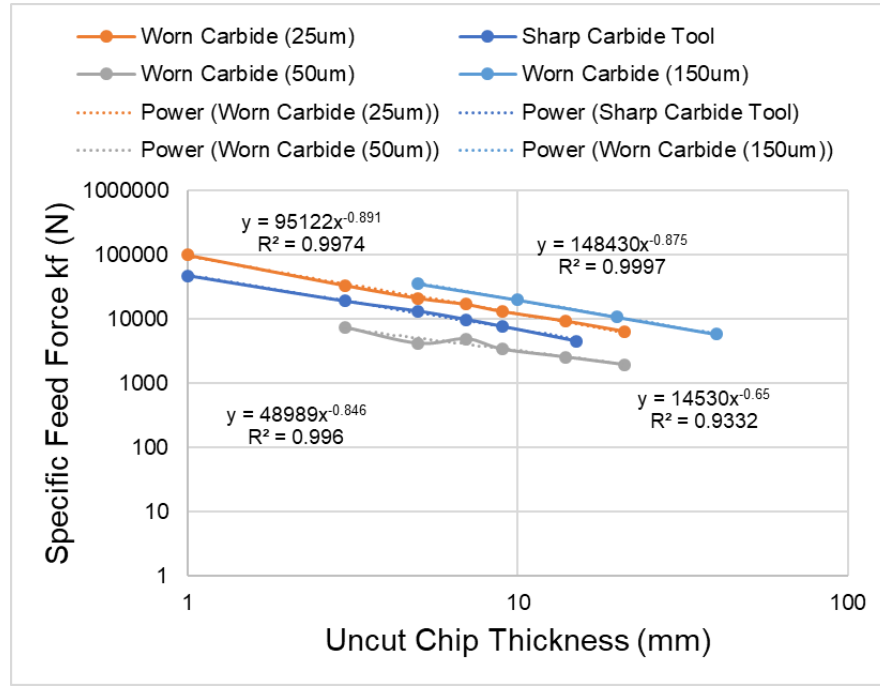
Figure 4-6. A plot of the specific feed force and chip thickness

The cutting force coefficient, k_{c1}; strain hardening coefficient, m_c as a function of flank wear (VB) is computed from the curve fitting is calculated by;

$$k_{c1} = 6058 \times VB^{0.4534} \tag{9}$$

$$m_c = 0.3043 \times VB^{0.1731} \tag{10}$$

$$K_{f1} = 6833 \times VB^{0.6312} \tag{11}$$

$$m_f = 0.5825 \times VB^{0.0956} \tag{12}$$
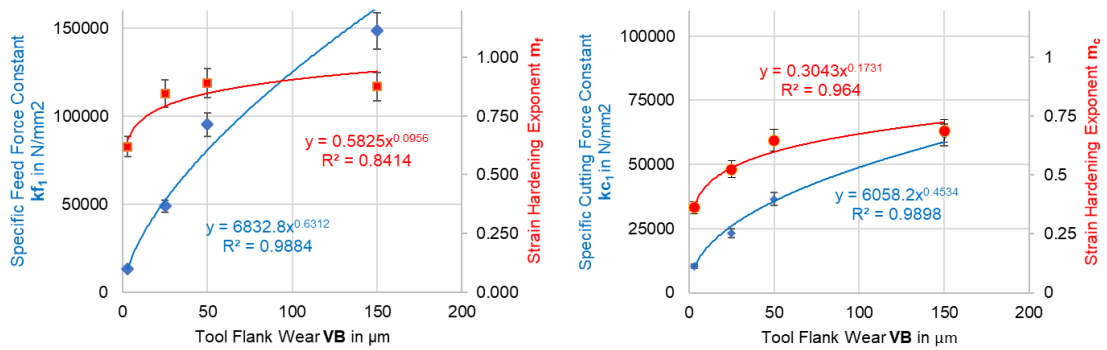
Figure 4-7. Plot of the specific feed and cutting force against the tool flank wear

To compute the sub-surface thermal distribution, a force model was developed for various uncut chip thicknesses, h; cutting speed, v_c; and dynamic tool flank wear condition, VB using the edge geometry calculations. The cutting, friction, and resultant force (F_c, F_f, F_r) are calculated as follows;

$$F_c = k_{c1} \times (h)^{-m_c} \times \left(\frac{100 - \gamma}{100}\right) \times w * 0.001 * h \tag{13}$$

$$F_f = k_{f1} \times (h)^{-m_f} \times \left(\frac{100 - \gamma}{100}\right) \times w * 0.001 * h \tag{14}$$

$$F_r = \sqrt{F_c^2 + F_f^2} \tag{15}$$

The final workpiece temperature was computed by first finding the workpiece heat partition estimate, HPE, as follows;

$$HPE = \frac{h_{min}}{F_r} \tag{16}$$

If $\frac{h_{min}}{F_r} > 1$, then $HPE = 1$, else,

$$HPE = \frac{h_{min}}{F_r} \tag{17}$$

Subsequently, the final workpiece cutting force, F_{cw}; is estimated by;

$$F_{cw} = F_c \times HPE \tag{18}$$

The shear plane length, l_s and maximum heat source extension (HSE are calculated for varying chip thickness as follows,

$$l_s = \frac{h_{min}}{\sin \emptyset} \tag{19}$$

Equivalent friction force as;

$$F_{r(eq.)} = HPE \times F_r \tag{20}$$

The approximate Peclet number of the chip is;

$$P_e = \frac{v_c \times l_s \times 10^{-6}}{4 \times \alpha_i} \tag{21}$$

The flash temperature is calculated as a function of cutting speed, uncut chip thickness, and Peclet number.

If $P_e > 5$

$$T_f = \frac{\pi * F_\beta * v_c}{k * \frac{w}{4}} * \sqrt{\frac{\kappa}{b * v_c}} \qquad (22)$$

If $P_e < 5$

$$T_f = \frac{\pi * C_4 * F_\beta * \kappa}{20 * k * w * b} \qquad (23)$$

The initial prediction of the flash temperature was computed using constant thermal properties. However, multiple iterations are needed, where properties are updated based on the previous prediction until convergence is achieved (typically three to five iterations). *(show convergence example graph)*
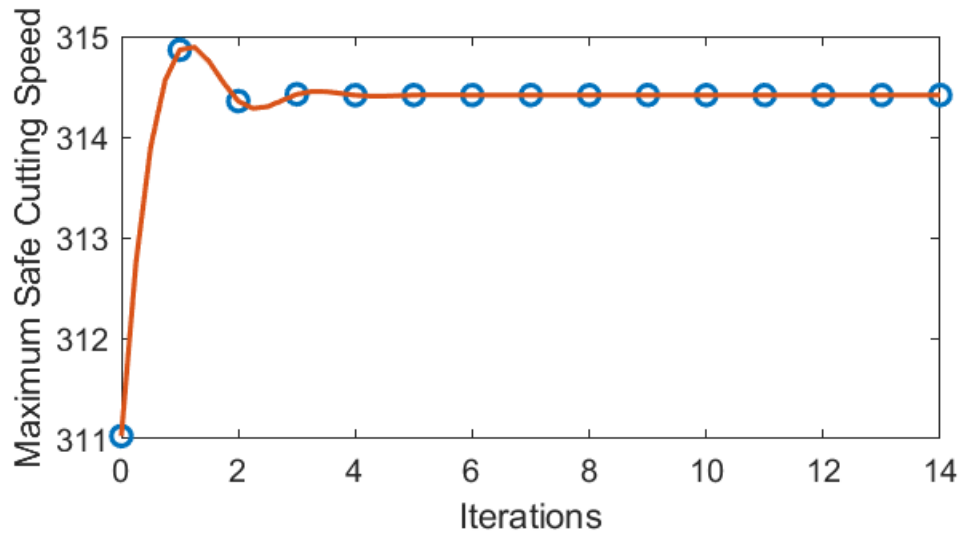
Figure 4-8. Maximum safe cutting speed against trial iteration plot

Based on graphs of flash temp vs. cutting speed, the maximum speed is determined at $T = T_{critical}$
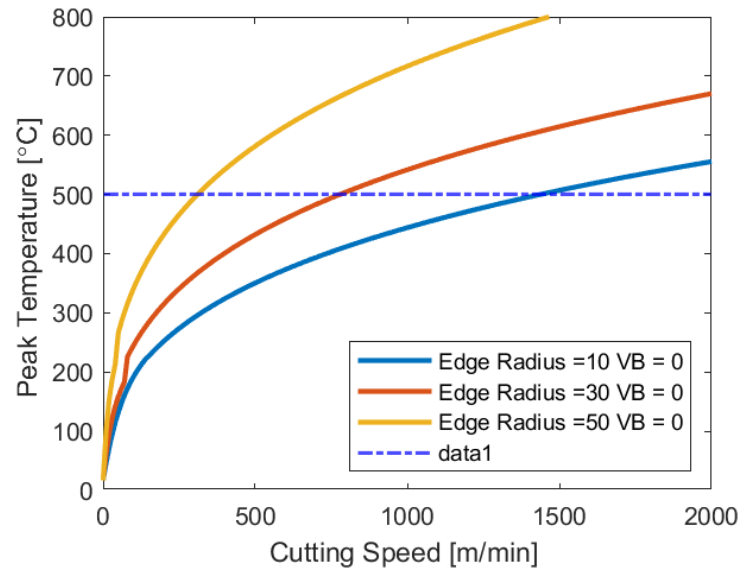
Figure 4-9. Peak temperature against cutting speed plot

4.2.4 Acoustic Emission

A KISTLER AE sensor, model 8152C with a 5125C AE coupler, 100–900 kHz bandwidth, and a National Instruments USB-6361 data acquisition system (DAQ) with a peak sampling rate of 2 Ms/ch were employed in this investigation. The AE sensor was incorporated into the cutting tool holder using a strong M6 screw connection following the manufacturer's specifications to ensure consistent signal attenuation while cutting. The AE sensor was roughly 20 mm away from the cutting tool tip, with the tungsten carbide cutting insert (NB2R geometry, K68 grade) separated from the AE sensor by the solid steel tool holder shank (grade AISI 4350). A major problem faced during AE signal analysis is the noise resulting from environmental conditions. These conditions are difficult to eliminate due to internal vibration generated by the servo motors while moving or holding position. To address this challenge, the extracted AE signals from the cuts must first undergo a denoising step before being analyzed. While there are several denoising approaches, the wavelet interval-dependent denoising technique in the MATLAB wavelet toolbox was adopted; however, an alternative Fourier transform approach could be applied so long as the extraneous signals do not vary over time.

Within the 1-D Wavelet Toolbox app, the reference wavelet of db2, or Daubechies 2, was used. It is a type of wavelet helpful in analyzing signals with sharp peaks that

typically occur during fracture events. Eight decomposition levels were used during signal processing, and the signal was then denoised. Threshold values for each of the eight decomposed levels were selected based on the signal acquired outside the testing region. The method for determining the threshold values can be summarized by selecting the 'lowest trough' for each level or the smallest signal amplitude. The eight levels range from lower to higher frequency content so that the various external signals can be filtered over the frequency ranges. After excluding the minimum acquired signal for each of the eight levels, the signal was cropped to the testing region. A later comparison between this method and reversing the order of denoising, then cropping showed little difference in the final output signal. However, the minimum threshold values were easier to spot when the tool was not engaged with the workpiece. The denoised signal can be further analyzed via scalograms through a convolutional neural network and traditional signal-analysis techniques. One observation made during this process is that the deeper and more aggressive the cut, the more the servo must operate to maintain the cutting depth and, therefore, more ringing and vibrations. This phenomenon causes the relative need for denoising to increase for a larger depth-of-cut.
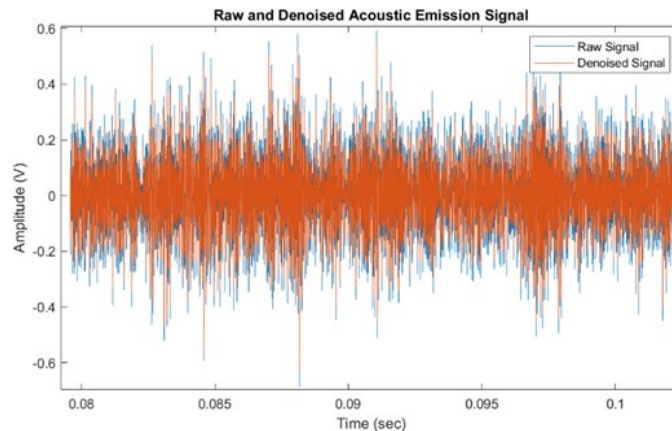
Figure 4-10. Raw and Denoised Acoustic Emission Signal

The denoised acoustic emission data plots show an increase in signal amplitude with respect to the chip thickness. This observation is due to an increase in the cutting force, and machine dynamics on the tool due to an increase in chip thickness. In the subsequent chapter, features such as mean, standard deviation, energy, and mean frequency

were extracted from the AE signal data with the intent that these features could help distinguish between different cutting modes to aid process monitoring and control.

4.3 SURFACE QUALITY MEASUREMENT

Surface crack formation is one of the prevalent drawbacks and challenges in *γ-TiAl* machining. In conventional machining practices, this problem is often solved or avoided by raising the process cutting temperature via an increase in cutting speeds, improving the alloy ductility, and reducing the chances of crack initiation. However, the downside of this approach is the concurrent increase in thermal load and accumulation at the cutting edge, which results in rapid tool wear or low tool life. Also, this approach is challenging to adopt in γ-*TiAl* machining since the cutting temperature must exceed the brittle-to-ductile transition temperature of 600°C - 700°C. The estimated cutting temperature at the cutting tool-workpiece interface using high-speed machining is around 420°C, which is below the brittle to ductile transition temperature expected in γ-*TiAl* machining. Uhlmann et al. (2009) proposed a workpiece preheating approach to overcome this limitation. They established that preheating the workpiece to about 300°C significantly reduced the size and density of surface cracks as to room temperature machining while increasing the preheat temperature to 700°C reduced the macro-cracks to micro-cracks and >800°C preheat temperature eliminated the surface cracks after machining.

The correlation between surface crack and tool wear was confirmed by Priarone et al. (2012a), showing that the ability of PCBN and diamond cutting tools to maintain a sharp cutting edge during cutting helps in reducing the crack density. A low crack density was also reported when low cutting forces were adopted in operations such as grinding (Beranoagirre and De Lacalle, 2013). It has been established that the cutting tool wears out concurrently as the surface defect occurs. Turning tests on titanium 45-2-2-0.8 alloy by Sharman et al. (2001a) showed that depth of cuts influenced the surface crack density by 67% when a low cutting speed and depth of cut between 0.05 and 0.1 mm were adopted. The least crack geometry (50 μm width and 5 μm depth) was observed in the smallest depth of cut (0.05mm), while the 0.1 mm depth of cut had a crack geometry of 150 μm width and 15 μm depth. Studies by Mantle and Aspinwall (1997) on gamma XD™ titanium aluminide

(*Ti-45Al-2Nb-2Mn-0.8% TiB₂*) turning at a low cutting speed of 25 m/min, 0.1 m/rev feed rate, and 0.7 mm depth of cut correlated the surface cracks to the flank wear and cutting time.

A custom coaxially illuminated microscope based on a Thorlabs ITL200 infini-ty-corrected tube lens was constructed using a Mitutoyo M-plan 10x long working distance objective lens for vertical surface analysis. Images were acquired using a View-Works VC-25MC 25 megapixel machine vision camera, Karbon-CL KBN-CL4-2.7-SP frame grabber, and Matlab image acquisition software. Three-dimensional scans of the machined surface morphology were captured using a ZYGO New View 7300 white light profilometer at 20x magnification. Three cutting modes were observed during the orthogonal cuts on the in-situ testbed, namely, ductile, brittle, or mixed cutting mode. The ductile cutting mode was observed between the range of 0-3 μm chip thickness, a mixed-mode between 3-5 μm, and brittle mode above 5 μm chip thickness, assuming a sharp cutting tool is used.

Figure 4-11 summarized the effect of the uncut chip thickness on the specific cutting forces while showing the top surface images of the machined sample.
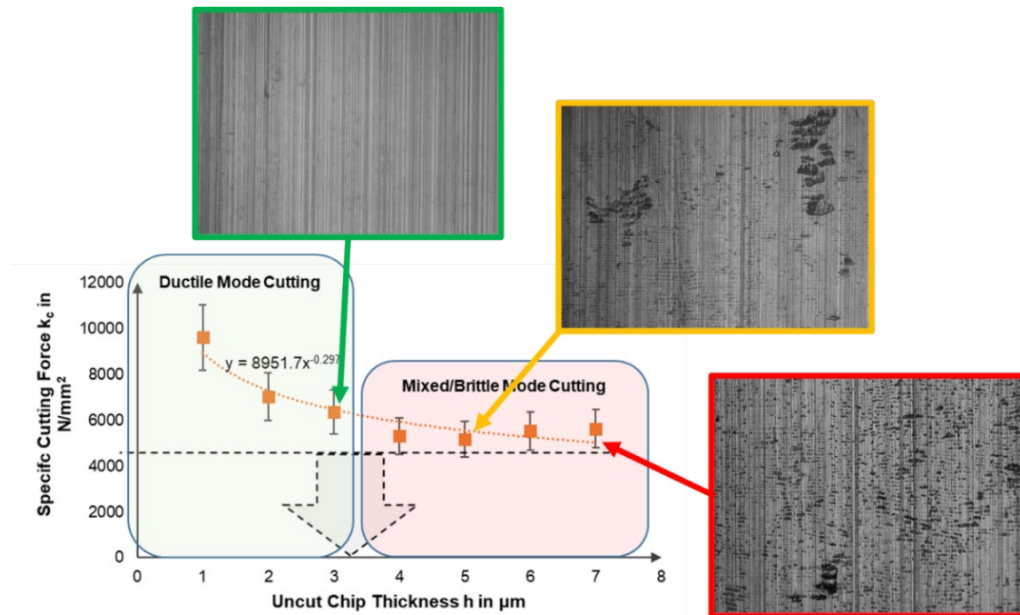
Figure 4-11. A plot of specific cutting force against uncut chip thickness and characteristic machined surface images.

Experimental trials show that for the same conditions (speed and depth of cut), the mode and morphology of surface fractures change between a sharp tool, mildly worn, and worn tool at the end of its useful life (as shown in Figure 4-12). Also, the type of surface cracks formed can be categorized either as mechanical cracks or thermal cracks. The mechanical cracks were mainly observed in sharp or slightly worn tools (1 - 25μm), while the thermal cracks were predominant in highly worn tools (50 - 150μm). This observation is due to the larger tool edge radius/ surface contact on worn tools, which increases the temperature.
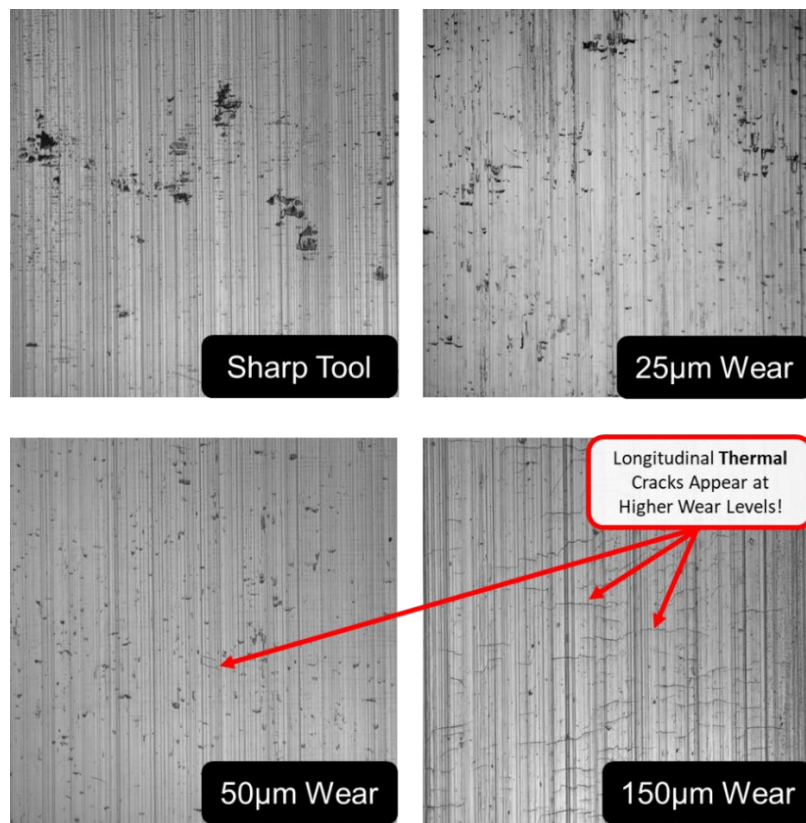
Figure 4-12. Surface images after machining using sharp and different worn tools

A MATLAB script evaluated the cracked machined surface area percentage by accounting for the black spots/cracks on the surface images. The algorithm converts the grayscale surface images captured by the upright Nikon microscope to black and white images using a specified threshold. The threshold value ranges between 0.27-0.32 depending on the image brightness and feed mark intensity, thereby manually adjusted as

needed. The algorithm computes the number of black pixels and divides them by the total number of image pixels, representing the gross crack percentage.

However, the gross crack percentage is not corrected for the feed marks, which sometimes have the same color intensity as the surface cracks. The crack algorithm processes a baseline surface image with zero cracks and uses the resulting crack percentage (due to feed marks) as a correction factor to account for feed marks. The baseline surface crack percentage is subtracted from subsequent images, thereby accounting for the feed marks. Figure 4-13 (a, b, and c) shows the surface crack output and the estimate algorithm's flowchart.
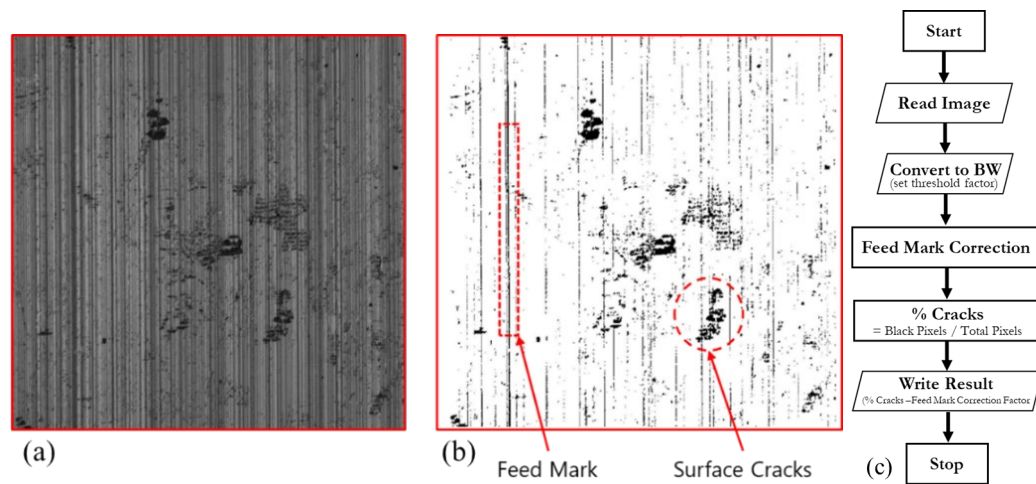
Figure 4-13. (a) Surface image with cracks at 21μm DOC using a sharp carbide tool (b) processed image output with MATLAB crack script (c) MATLAB script flowchart.

We captured data for six trials at each depth of cut. Due to camera limitations, the overall surface image from each of these cuts was divided into 50 segments. The surface images segments were processed with the developed MATLAB script, and the crack percentage of each segmented image was computed and averaged per depth. Figure 4-14 shows the plot of the average surface cracks against chip thickness (1, 3, 5, 7, 9, 14, 21 μm) for a sharp carbide tool cut at a 60 m/min cutting speed. The crack trend and representative surface images are captured in Figure 4-14, which shows that the surface crack percentage and measurement deviation tend to increase with the depth of cut. From observation, ductile cuts with few or no microcracks were recorded for cut depth less than

five microns, and the surface cracks from 5 μm upward exhibit a brittle cutting mode with pronounced micro and macro cracks. These cracks result from the mechanical effect on the surface during machining. The final surface quality from each trial was categorized into three groups: good, marginal, and poor quality, considering the average surface crack percentage shown in Figure 4-14. Data from trials with a surface crack percentage less than 2.5% are grouped as good quality. In comparison, trials with crack percentages above 2.5% but lower than 3.6% are grouped under marginal quality. The remaining trials with a higher crack percentage (above 3.6%) are grouped as poor quality.
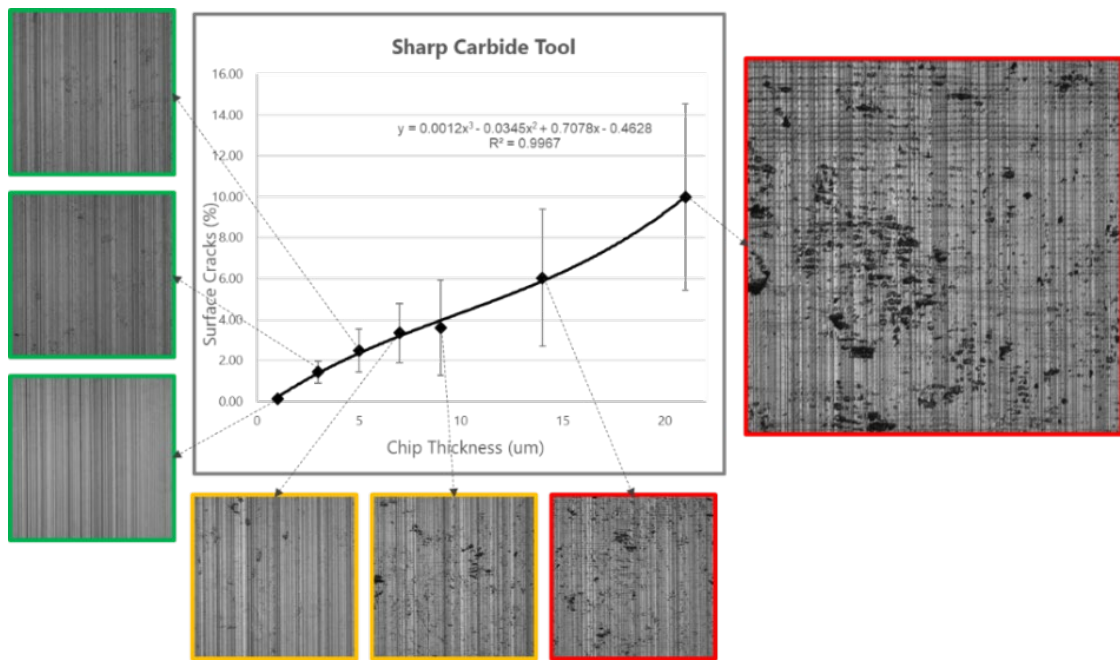
Figure 4-14. Average surface cracks against chip thickness plot with respective optical images using a sharp carbide tool.

4.4 MECHANICAL FRACTURE

During titanium aluminide machining, mechanical fractures are formed depending on the cutting tool geometry and parameters. This fracture type was predominant in sharp cutting tools with chip thickness of less than 21µm and slightly worn cutting tools less than 10µm. This phenomenon can be traced to the mechanical force load on the machined surface and lower cutting temperature under the above-specified cutting conditions.

Mechanical fractures are undesirable in the final machined surface due to their adverse effect on the fatigue life of these components during the use stage. In order to quantify the depth and severity of these fractures, three-dimensional scans of the machined surface morphology were captured using a ZYGO New View 7300 white light profilometer at 20x magnification. The surface scans were taken at five different locations. Their average values and deviations were reported for perfectly sharp tools, 25µm VB worn tools, and 50µm VB worn tools (all tools are made of tungsten carbide). Figure 4-15 shows sample 3D images for machined surfaces captured with Zygo3D profiler.
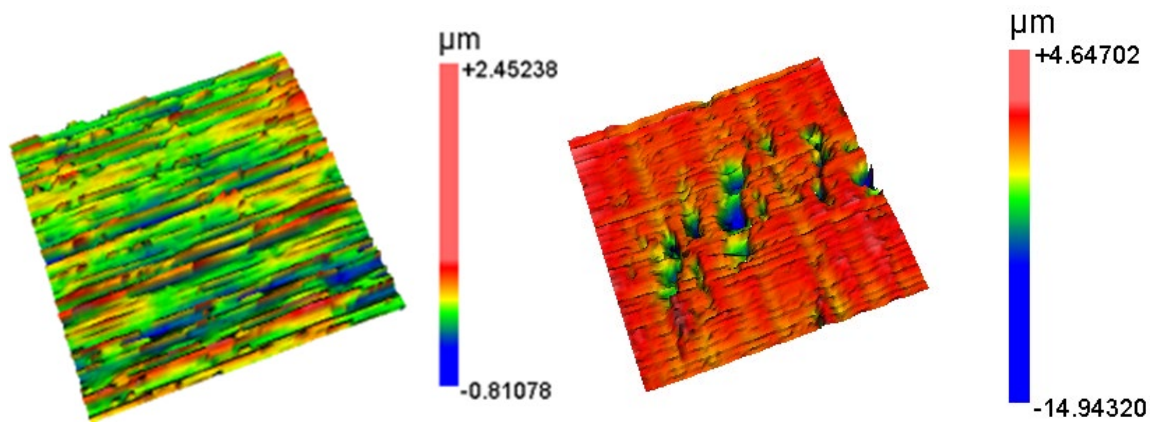
Figure 4-15. Sample 3D images for machined surfaces captured with Zygo3D profiler (a) ductile cut (b) brittle cut

From Figure 4-16, it can be seen that the fracture depth increases with the uncut chip thickness. A fracture depth of 3µm was observed with sharp tools; however, no significant fracture depth was recorded in worn tools at a chip thickness less than 5µm. This observation is due to the minimum chip thickness phenomenon of the ploughing or smearing effect synonymous with worn tools. The maximum value of the uncut chip thickness was constrained to 21µm due to the extreme surface damage to the machined surface at this value. Also, it can be observed that the maximum average fracture depth of approximately 15µm was recorded across the cutting tools.
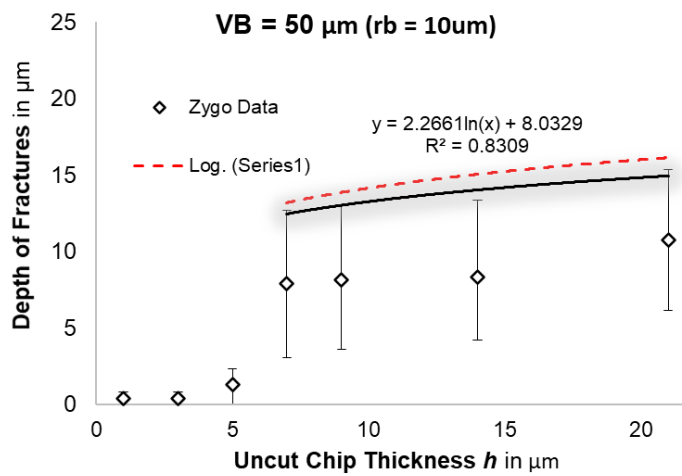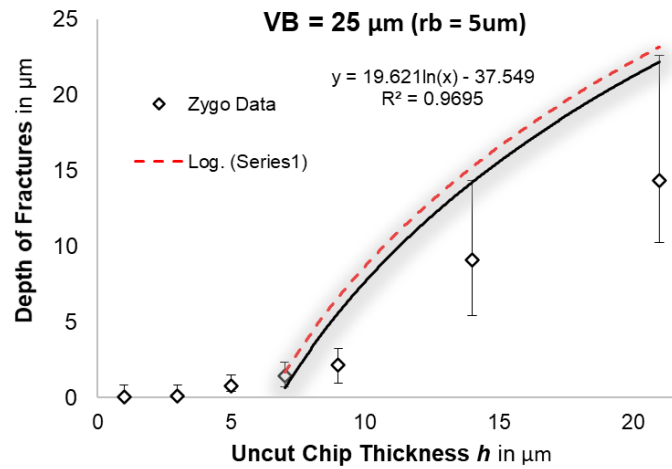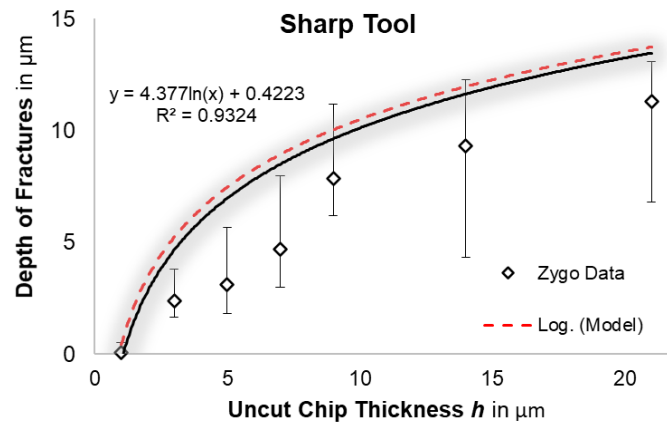
Figure 4-16. Plots of fracture depth against uncut chip thickness

Figure 4-17 summarizes the experimental fracture findings, showing that to avoid surface cracks, the maximum uncut chip thickness should be limited to 1µm for a sharp tool, 3µm chip thickness for a 25µm VB worn tool, and 5µm chip thickness for a 50µm VB worn carbide tool. Therefore, it can be concluded from Figure 4-17 that higher tool wear allows for higher uncut chip thickness. This finding also provides a conservative approach to achieving a good surface finish while machining titanium aluminide alloys.

Critical/Max Chip Thickness to Avoid Fracture

$$y = 0.0827x + 0.649$$
$$R^2 = 0.9934$$
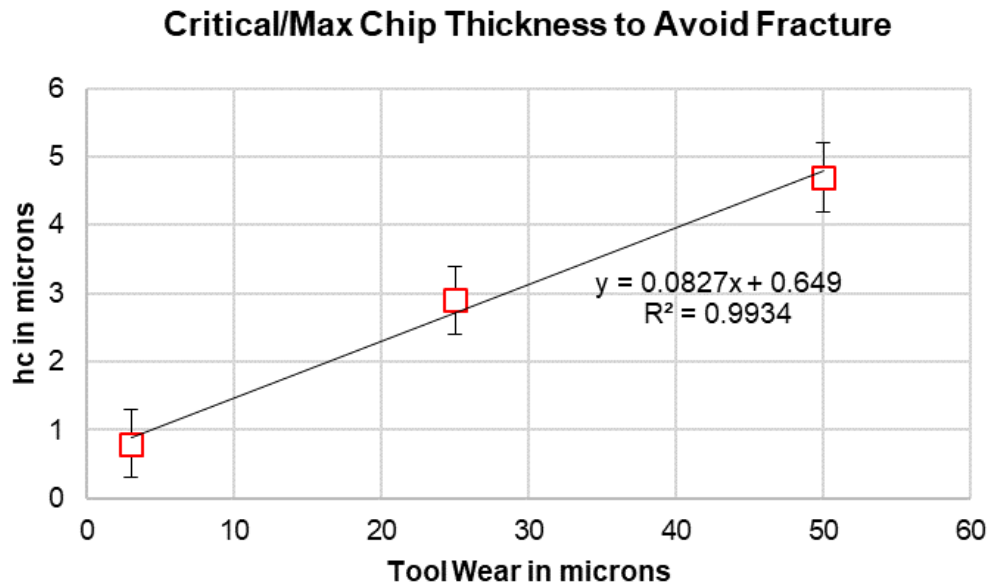
Figure 4-17. A plot of critical chip thickness beyond which fracture will occur as a function of tool wear

4.5   SUMMARY AND CONCLUSIONS

In this chapter, the high-speed imaging setup on the in-situ testbed made it possible to observe the machining process. An initial set of machining parameters for crack-free machining of titanium aluminide was established using a sharp and worn carbide cutting tool. In addition, mechanical fractures experienced during *TiAl* machining were captured using empirical models, and resulting conclusions were drawn:

- Captured high-speed images gave the capability for severe plastic deformation, sub-surface, strain, and strain rate characterization using Digital Image Correlation.
- Analysis showed (sub-) grain displacement/stress localization due to anisotropic material response to the thermo-mechanical loads of cutting. Grain pullout/cracking

occurred preferentially when *TiAl* lamellae were approximately perpendicular to the shear plane, i.e., mechanical loading was applied along the weakest direction of the microstructure.

- Experimental results show ductile cuts with few or no microcracks occur at chip thickness less than 5 microns, while chip thickness from 5 microns and upward shows a brittle cutting mode with prominent micro and macro cracks. This phenomenon can be traced to the mechanical forces acting on the surface while being machined.

- Both sharp carbide and PCBN tools have a similar data profile; their cutting force magnitude increases as the chip thickness and tool edge radius rise.

- The mechanical fracture depth increases with the uncut chip thickness; however, to achieve a crack-free surface using a conservative approach, the maximum uncut chip thickness should be limited to 1μm for a sharp tool, 3μm chip thickness for a 25μm VB worn tool, and 5μm chip thickness for a 50μm VB worn carbide tool. Therefore, it can be concluded that higher tool wear allows for higher uncut chip thickness.

- Efforts in this chapter have observed the machining of titanium aluminide alloys in real-time and have established safe boundaries for cutting parameters. These experiments have been conducted while looking at the machining process from a single plane with an optical microscope; however, the cracks formed during *TiAl* machining do not occur at a single plane but throughout the entire volume of the machined workpiece.

CHAPTER 5.

QUALITY MONITORING USING ACOUSTIC EMISSION SCALOGRAM

5.1   SCOPE AND INTRODUCTION

Efforts in this work thus far have focused on a single plane observation of the crack initiation and propagation during titanium aluminide machining; however, the cracks occur anywhere in the volume of the machined component and not just on the single plane of high-speed imaging. This chapter targeted efforts to achieve real-time monitoring of the entire crack propagation across the workpiece volume during *TiAl* machining. The formation of cracks in different materials has been accompanied by the stress wave generated from the rapid release of energy from localized sources (Kobayashi et al., 2015; Sun and Balk, 2008). An approach widely accepted for crack analysis across various literature is acoustic emission signal analysis. Studies have shown that sound emission occurs at the tool/workpiece/chip interface and is directly influenced by changes in the cutting process, making acoustic emission signal analysis an appropriate technique for process condition monitoring. Analyzing the AE signal extracted from the testbed, the crack signals formed were rapid and tended to occur at approximately 65 kHz. Conventional acoustic emission signal processing techniques involve manual extraction for signal statistical features such as mean, standard deviation, and root mean square values. However, this is tedious, and it is difficult to capture the best parameters that accurately describe the process with this approach. This study explores machine learning techniques (such as the convolutional neural network) to minimize the AE signal pre-processing and feature extraction steps. However, the AE signals collected were first examined for differences in pattern using principal component analysis.

Efficient integration of machine learning techniques with signal analysis often comprises a three-phase process: signal collection, feature selection/extraction, and model training (Fu et al., 2017). The signal collection phase involves a holistic experiment design, collection, and accurate labeling. The feature extraction phase involves detecting key signal characteristics and matching them with their corresponding data labels. The model training phase matches the extracted features with their respective process states. Manual feature

extraction involves a human selection of crucial data characteristics suitable for the problem. However, the features selected are only suitable for that specific problem and might not be relevant in a different scenario. Also, it might be challenging to decide between features of similar performance.

5.2   PATTERN RECOGNITION

Pattern recognition technique applies mathematical or machine learning algorithms on existing data to distinguish and categorize between process trends for process decision and control. It is essential to collect good and quality data to achieve efficient pattern recognition. The data must be filtered, classified, evaluated, and interpreted for AE signals. The collection of object characteristics is helpful in adequately describing the object. The features or characteristics, f, of an AE signal can be collected to form a vector, x in a dimensional space, d. The collection of all the vectors in a table represents the pattern matrix. The next step after a feature extraction is data pre-processing, where the collected data can be processed to a usable form for data comparison. This step involves feature calculation, selection, normalization, and transformation. Feature normalization is a common and important step in data preprocessing and pattern recognition, as it helps transform the multiple features to the same scale or range. For instance, extracted AE features such as amplitude, 0.8V, and frequency (200KV) can be normalized to the same range, e.g., 0 to 1. Other transformations, including zero mean or unit variance, are also applied during the normalization step. Once the data is pre-processed, the next step would be to find similarities between the collected data and a known database. The new data is categorized under the group whose pattern is similar. Pattern classification can be achieved by two main methods: unsupervised pattern recognition and supervised pattern recognition.

- Unsupervised pattern recognition is a technique in which data can be classified to the appropriate group without needing a prior or existing database. The data is classified using feature comparison and cluster generation.
- Supervised pattern recognition involves classifying data into the appropriate group by comparing the data/feature pattern to an existing database. This technique learns from example; hence the name supervised learning. Before applying this technique

103

to acoustic emission, it is essential to understand the possible classes or process conditions.

5.3 PRINCIPAL COMPONENT ANALYSIS

Principal component analysis (PCA) is a dimensionality reduction approach for large datasets; the reduction is achieved by transforming the large dataset with multiple features into a smaller dataset while still retaining most of the information in the large dataset. Having a smaller dataset makes data visualization, exploration, and analysis much easier and faster. Also, reducing the dataset variable is perfect for machine learning algorithms. While reducing the number of variables in data typically affects the accuracy, it is possible to maintain high accuracy and simplicity concurrently with PCA. In summary, PCA reduces the number of variables in a dataset while preserving as much information or minimizing variation.

The first step in PCA is to standardize or normalize the continuous range of the initial variable such that they are all on the same scale. Mathematically, this can be achieved by subtracting the variable mean from the original value and dividing it by the standard deviation for each variable.

$$z = \frac{value - mean}{standard\ deviation} \tag{24}$$

In the second step, the covariance matrix is calculated. This step aims to understand how the data values vary from the mean to each other and investigate any relationship between them. The covariance matrix helps to detect any form of correlation between the variables. Subsequently, in the third step, eigenvectors and eigenvalues are calculated from the covariance matrix to determine the data's principal components. Principal components are new variables constructed as a linear combination of the initial variables. These new variables are constructed such that they are uncorrelated and still contain a significant chunk of the original information. It is important to note that multiple principal components are formed. However, the maximum possible information is stored in the first principal component. For instance, if there are seven principal components, PCA stores most of the

data information in the first component and stores the following most important information in the second component.

In this work, thirteen features (minimum amplitude, maximum amplitude, mean, RMS, peak RMS, peak to peak, variance, standard deviation, kurtosis, energy, band power, power bandwidth, mean frequency) were extracted from the acoustic emission signal data collected during orthogonal milling of the titanium aluminide sample. These features were passed through a dimension reduction using principal component analysis, and Figure 5-1a and b show the 2D and 3D PCA plots. From the feature space on the plot, it can be seen that there is a distinction between the AE signal of the three strategies adopted. The thermal wear strategy tends to tilt to the right, while good quality and mechanical wear strategies tilt to the left and appear more similar. This similarity is most likely due to the intermittent formation of the cracks across the surface, while for most of the cut, they both have a similar data profile.
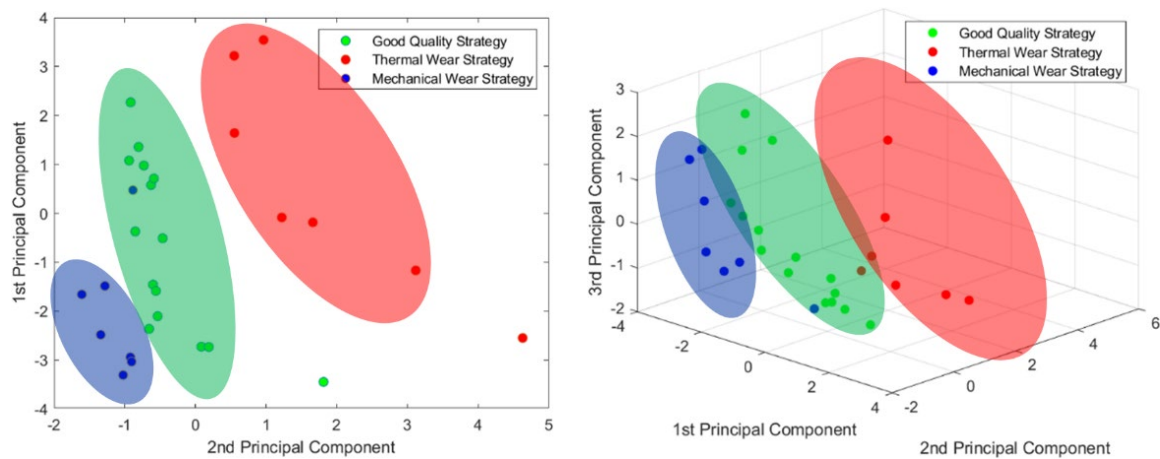
Figure 5-1. (a) 2D Principal component plot for different wear strategies (b) 3D Principal component plot for different wear strategies

5.4 CONTINUOUS WAVELET TRANSFORM

Fourier transform captures the frequency information over an entire signal using only sine and cosine basis functions. However, this approach is unsuitable for signals with short intervals of characteristic oscillations, such as in Electrocardiography (ECG). Wavelet transform can address this limitation by decomposing functions into sets of

infinite wavelets basis functions, which is ideal for non-stationary and non-linear signal analysis. Wavelet transform also has variable windows, giving more accurate signal data information (Neupane et al., 2021). Wavelets are wave-like oscillations localized in time. There are two types of wavelet transform; continuous and discrete wavelet transform. Continuous wavelet transforms (CWT) use all possible wavelets over various locations and scales, while discontinuous wavelet transforms (DWT) are defined to specific locations and scales. The difference between these two methods includes scale parameter discretization, transient localization of non-stationary signals, and the time resolution in the frequency band. CWT has better scale discretization and is more suitable for transient localization in non-stationary signals than DWT. CWT is displacement insensitive while DWT is displacement dependent; overall, CWT is the most suitable for non-stationary signals. CWT methods transform one-dimensional time signals to a two-dimensional time-frequency domain and are highly useful in time-frequency location multi-resolution of signals. They are mathematically represented as follows:

$$CWT(a, \tau) = \frac{1}{\sqrt{a}} \int_{-\infty}^{+\infty} s(t) \psi^* \left(\frac{t - \tau}{a} \right) dt \tag{25}$$

where a is the wavelet scale, ψ^* represents the mother wavelet (ψ) conjugate, τ is the wavelet time localization and $\frac{1}{\sqrt{a}}$ maintains the wavelet energy constant at varying scales. Signal representation with CWT allows better visualization and analysis of signal data extracted from machining processes. There are different types of CWT, of which Mexican, Morlet, and Gaussian wavelets are the most common. The Morlet wavelet is more suitable for wideband signals with time-based frequency and scale attributes (NajmiandSadowsky, 1997). In ths present study, a morlet based wavelet was adopted to generate acoustic emission scalograms. A spectrogram is the frequency spectrum representation of an audio signal as a function of time. It is generated when the signals are windowed with a constant length window adjusted in time and frequency. Similarly, the application of CWT on signals gives a 2D time-frequency spectrum known as scalograms. Scalograms represent a continuous wavelet transform (CWT), whose color code represents the wavelet coefficient magnitude, a dimensionless estimate that localizes the AE energy in both time and frequency. Scalograms are obtained from wavelets shifted in time and are

particularly useful for short sound signals with high frequency. The analytical morlet wavelet was used as the wavelet basis function for the scalogram generation of the AE signals.

5.5 CONVOLUTIONAL NEURAL NETWORK

Deep learning is a machine learning tool that uses deep architecture to extract high-level abstraction from data by combining several linear and non-linear processing units. Some of the deep learning techniques are auto-encoders, convolutional neural networks (CNNs), deep belief networks (DBNs), and multi-layer perceptrons. CNN is a deep learning technique explicitly designed for image classification. It comprises multi-layer perceptron variants that detect visual trends in images. An input image, feature extraction block (comprising convolution, activation, and pooling layers), fully connected layers, and a classification layer make up a typical CNN architecture. The convolutional layer is the most critical block in a CNN architecture because it performs most of the computation. It requires data, a feature detector (kernel or filter), and a feature map as inputs. The feature detector moves across the receptive fields of the image, searching for features, a process known as convolution. The dot product of the input pixels and the filter is computed, and the filter is applied to a specific image area. When the filter is finished, it shifts by a stride and repeats the process for other image areas until the entire image has been covered. Each stride's final output is passed to an output array, and the total output of this computation is referred to as a feature map or activation map.

The output depth is determined by the number of filters used; three filters would result in a depth of three (three feature maps). The fully connected layer classifies the images using features extracted from the previous layers and SoftMax activation filters. CNN architecture comes in various variants, including LeNet, AlexNet, GoogleNet, and ResNet. The pooling layer reduces the number of parameters that must be entered. Dimensionality reduction is a technique used to reduce the size of a dataset. It scans through the input with a filter in the same way that the convolutional layer does. The filters in the pooling layer, on the other hand, have no weight, and the final output array is simply the sum of values from each receptive field. The maximum value of each receptive field can

be sent to the output array, known as max pooling, or the average value, known as average pooling. Though the pooling layer can lose much information, it helps to reduce overfitting and complexity while also increasing efficiency.

AlexNet is a deep learning structure whose architecture consists of five convolutional layers, three max-pooling layers, two normalization layers, two fully connected layers, and one softmax layer. The AlexNet architecture was introduced in 2012, like the 1998 LeNEt architecture. However, it is a deeper structure and uses a ReLU activation instead of a sigmoid function. The first convolutional layer comprises an 11 x 11 window shape to capture the input image fully. This window is followed by a 5 x 5 window size in the second layer and a 3 x 3 windows size on the remaining convolutional layers. The choice of ReLU as the activation function in AlexNet makes the computation easier and model training easier when adopting different parameter initialization methods. AlexNet adopts a drop-out approach to control model complexity, while LeNet only uses weight decay.

Typically, AE signals are one-dimensional; however, recent research efforts have represented the 1D AE signals as 2D CWT images (Neupane et al., 2021; TranandLundgren, 2020). This method is often preferred as images represent information better than one-dimensional signal charts. The application of CNN extends across object tracking and recognition, text tracking and recognition, action recognition, and scene labeling. Following the acoustic emission signal denoising and pre-processing, the local time-frequency attributes or scalograms of the AE signals were generated using the wavelet time-frequency analysis, a unique class of analytic wavelets known as Morse wavelets in MATLAB. MATLAB used the cwtfilterbank to segment the time-bandwidth to 1.7 ms mini-signals and tune the Morse wavelet. The segmented signals were converted to scalogram images and grouped into their respective quality groups as described above. Figure 5-2 and Figure 5-3 show the 2D and 3D scalogram outputs for 1 and 21 μm depths of cut using a sharp carbide tool. The 2D scalograms show the signal frequency as high as 65 to 100 kHz. Figure 5-2 shows a low wavelet coefficient magnitude and high frequency for the 1 μm/ductile cut, while a higher magnitude at lower frequency was recorded for the 21 μm/brittle depth of cut, as shown in Figure 5-3. This difference in magnitude and shift

in frequency resulted from the cracks/fracture on the specimen surface at a higher depth of cut, as displayed in Figure 5-3c. The wavelet coefficient magnitude for the 1 µm cut with a fine surface finish is concentrated around 100 kHz, while the 21 µm cut with a poor surface finish is concentrated around the 20–55 kHz range, as shown in Figure 5-3a. The surface images in Figure 5-2c and Figure 5-3c have been time-matched to the scalograms to clearly show the workpiece surface state at the specific instance on the scalogram representation (Figure 5-3).
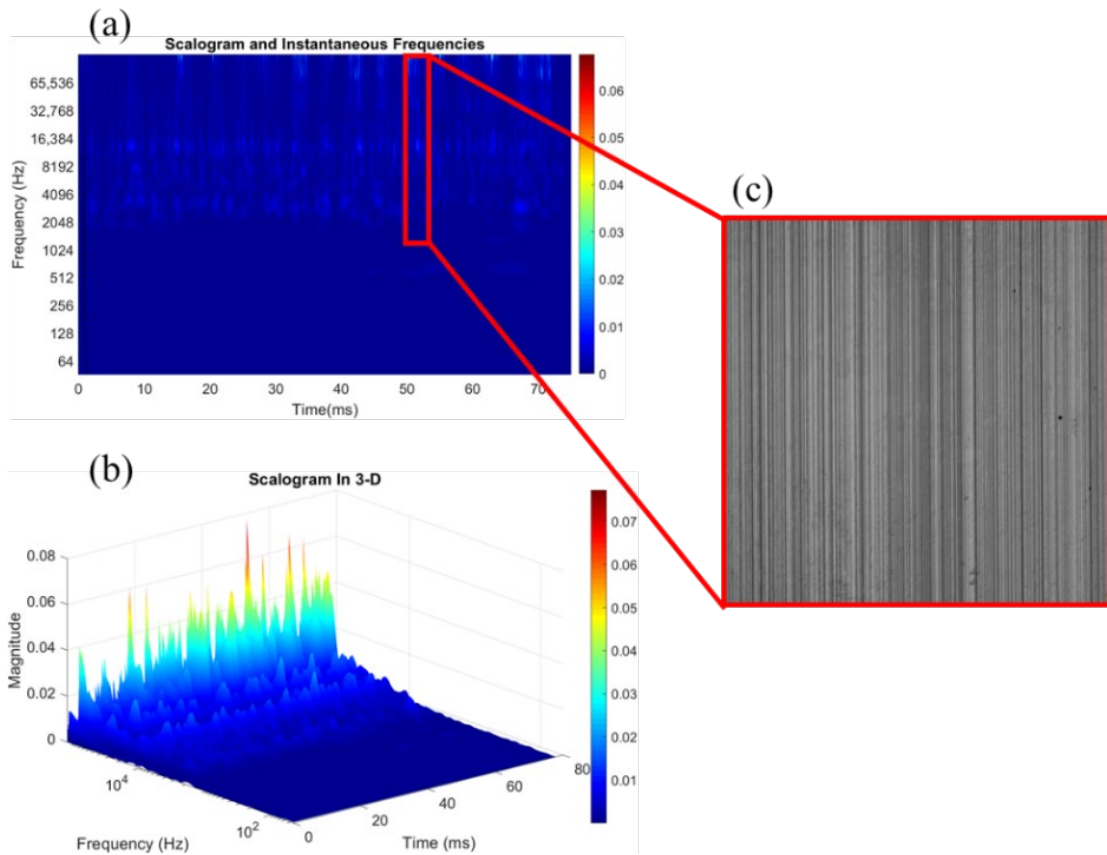
Figure 5-2. (a) 2D scalogram, (b) 3D scalogram, and (**c**) surface image for 1 µm depth of cut at 60 m/min (Source: Adeniji et al. (2022) with permission of CC BY 2.0)
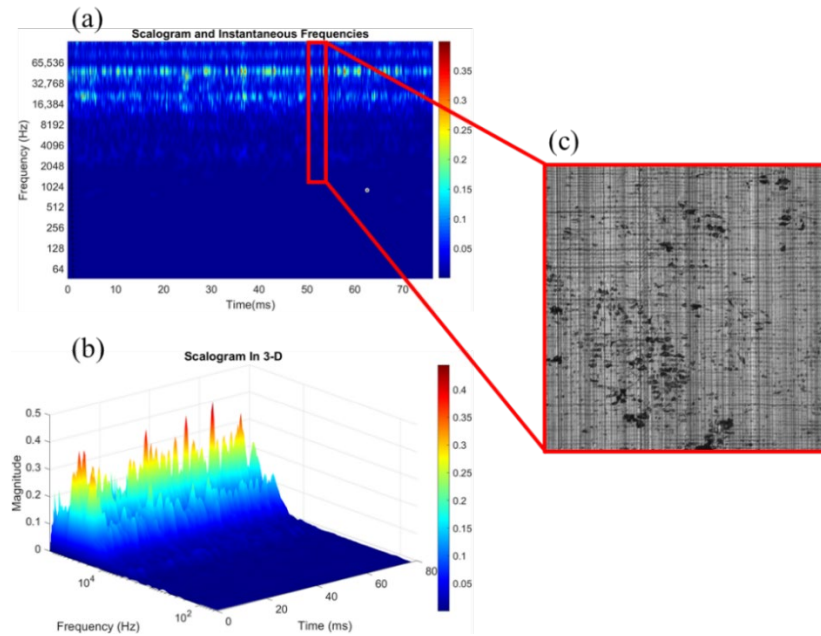
Figure 5-3. (a) 2D scalogram, (b) 3D scalogram, and (**c**) surface image for 21 um depth of cut at 60 m/min (Source: Adeniji et al. (2022) with permission of CC BY 2.0)

Figure 5-4 shows a pictorial representation of the acoustic emission wavelet analysis data observations, showing the ductile cutting mode with fewer surface cracks, high signal frequency, and low magnitude. The mixed/transition cutting mode is concurrent with the ductile and brittle cutting mode (BCM). The BCM occurs at a lower signal frequency with a higher magnitude.
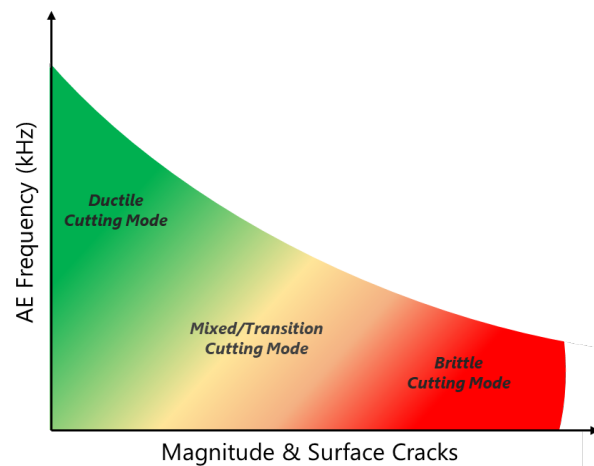
Figure 5-4. Qualitative illustration of the observed trend in $\gamma\text{-}TiAl$ cutting mode (Source: Adeniji et al. (2022) with permission of CC BY 2.0)

110

5.5.1 CNN for Fracture Detection (Feature Extraction and Classification)

In this section, the scalograms generated from the acoustic emission signals were passed through a convolutional neural network for image or signal classification. We created three data categories (good, marginal, and poor surface quality), considering the computed surface crack percentage of each cut. For instance, for the sharp tool cuts, the 1, 3, and 5 µm depths of cut comprising 18 AE signals were categorized as good quality, the 7 and 9 µm depths of cut comprising 12 AE signals as marginal quality, and the 14 and 21 µm depth of cut scalograms consisting of 12 AE signals as poor quality (selected samples shown in Figure 5-5). Since the same workpiece sample and cutting speed were used for these trials, each of the captured AE signals had a length of 80 ms. After converting the AE signal data, each trial dataset had only about 270 scalogram images of 227 x 227 pixels, displayed in Figure 5-6. Passing this small amount of data into CNN models would result in overfitting due to the small size. The features can be extracted by passing the scalogram images to a pre-trained deep neural network (DNN) to overcome this challenge. A pre-trained network is a CNN model trained on a large dataset whose learning can then be transferred to smaller datasets. The typical pre-trained architecture includes VGG, AlexNet, ResNet50, and InceptionV3. This work used VGG19 and ResNet50 architectures previously trained on more than a million images as the pre-trained network to extract the scalogram features. Using these three models for classification would help compare their respective performances and select the best classifier for further analysis. Table 5-1 shows the segmented scalogram images for each category and dataset.

Table 5-1. Number of segmented images for respective categories and datasets.

Categories	Dataset A		Dataset B		Dataset C	
	Training	Testing	Training	Testing	Training	Testing
Good	679	129	720	158	1035	332
Marginal	440	100	500	115	774	200
Poor	440	100	540	130	1041	558
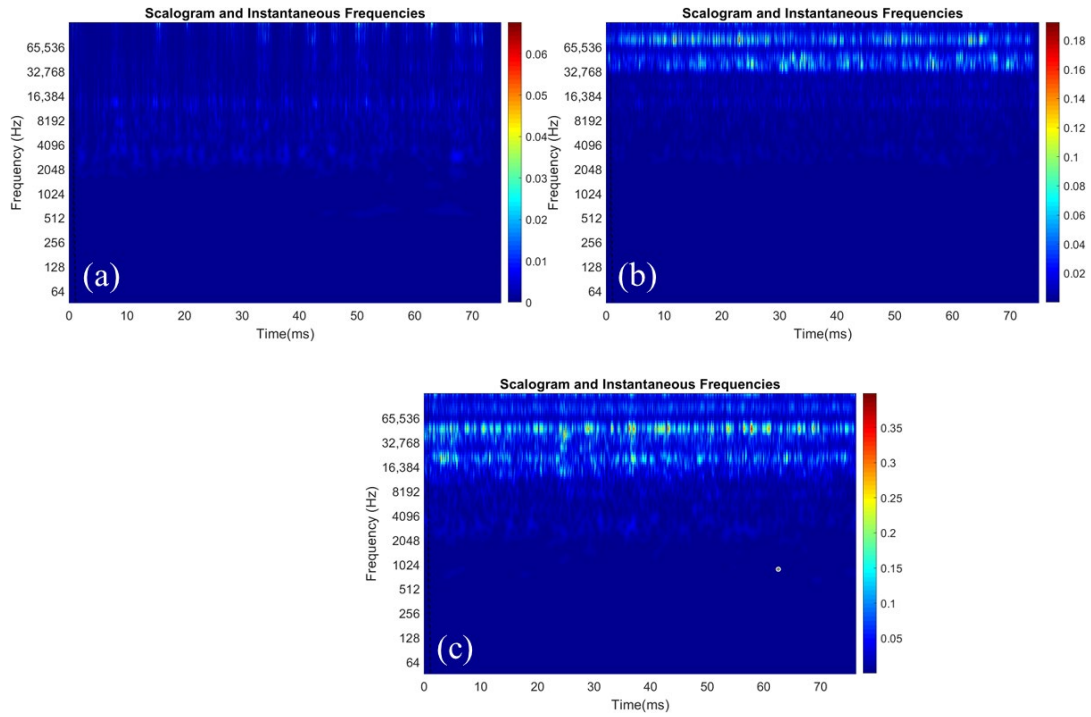
Figure 5-5. Typical scalogram image for (**a**) good surface quality, (**b**) marginal surface quality with minor cracks, and (**c**) poor surface quality (Source: Adeniji et al. (2022) with permission of CC BY 2.0)
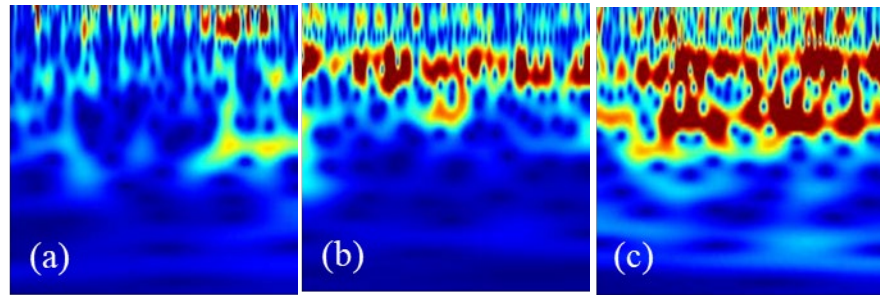
Figure 5-6. Typical CWT segmented scalograms for (**a**) good surface quality, (**b**) marginal surface quality with minor cracks, and (**c**) poor surface quality (Source: Adeniji et al. (2022) with permission of CC BY 2.0)

The experimental trials with a sharp tool were performed at 1m/s cutting speed for varying depths of cut: 1, 3, 5, 7, 9, 14, and 21 μm. The worn tool trials were captured at 0.2 and 1 m/s cutting speeds for only the 3 and 21 μm depths of cut. The worn tool chip thickness was limited to 21 μm due to the fatal surface damage (thermal and mechanical

cracks) observed above the 21 µm depth of cut. The extracted scalograms for both sharp and worn tool cuts were grouped into Dataset A, Dataset B, and Dataset C. Dataset A consists of only sharp tool scalograms, grouped into training and testing datasets. Dataset B consists of both sharp and worn tool scalograms; however, only the sharp tool scalograms are used for training, while the worn tool scalograms are used for testing. This approach evaluates whether the sharp tool cutting data can adequately predict the worn tool cutting condition. Similarly, Dataset C consists of all the scalograms, but the training and testing data include an adequate proportion of sharp and worn tool scalograms.

In this work, we adopted both the accuracy and F1 score to evaluate the performance of the proposed models. The accuracy indicates the correct classification rate. The F1-score is computed from precision and recall, representing the value of true positives divided by the cumulation of true and false positives. In contrast, recall is the value of true positives divided by aggregating true positives and false negatives. Table 5-2 shows the accuracy and F1 score of different classifiers. The result shows that a scalogram is an effective way of representing the acoustic emission signal. The lowest accuracy recorded for Dataset B is traceable because the models were trained with sharp tool scalograms and tested on worn tool scalograms. The poor performance in this dataset establishes the theory that machine/process dynamics differ and cannot be transferred between different tool geometries. The confusion matrix for the best models is shown in Tables 3 and 4 for Datasets A and C. The confusion matrix for Dataset B was excluded due to its poor performance. Table 5-2 shows that the accuracy of VGG19 makes it the best performing model across all datasets, with emphasis on Datasets A and C. The accuracy of the "good" surface quality signals had the highest performance in the confusion matrix in both datasets. It is also shown that there is repeated misclassification between the "marginal" surface quality scalograms and that of both good and poor category scalograms. The convergence of the training and validation process of VGG19 is shown in Figure 5-7. Convergence of the training and validation process of VGG19: (**a**) accuracy and (**b**) cross-entropy loss (Source: (Adeniji et al., 2022)

113

Table 5-2. The accuracy and F1-score of the selected models.

Classifier	Dataset A		Dataset B		Dataset C	
	Accuracy (%)	F1-Score	Accuracy (%)	F1-Score	Accuracy (%)	F1-Score
VGG19	76.78	0.75	39.27	0.33	80.83	0.78
ResNet50	78.64	0.78	51.64	0.40	50.92	0.60
AlexNet	75.00	0.70	46.25	0.35	60.52	0.65

Table 5-3. The confusion matrix of the best performing model (VGG19) for Dataset A.

Labels	Good (%)	Marginal (%)	Poor (%)
Good	93.02	6.98	0.00
Marginal	21.65	72.16	6.20
Poor	1.03	39.18	59.79

Table 5-4. The confusion matrix of the best-performing model (VGG19) for Dataset C.

Labels	Good (%)	Marginal (%)	Poor (%)
Good	89.76	3.61	6.63
Marginal	26.00	62.00	12.00
Poor	10.75	6.98	82.26
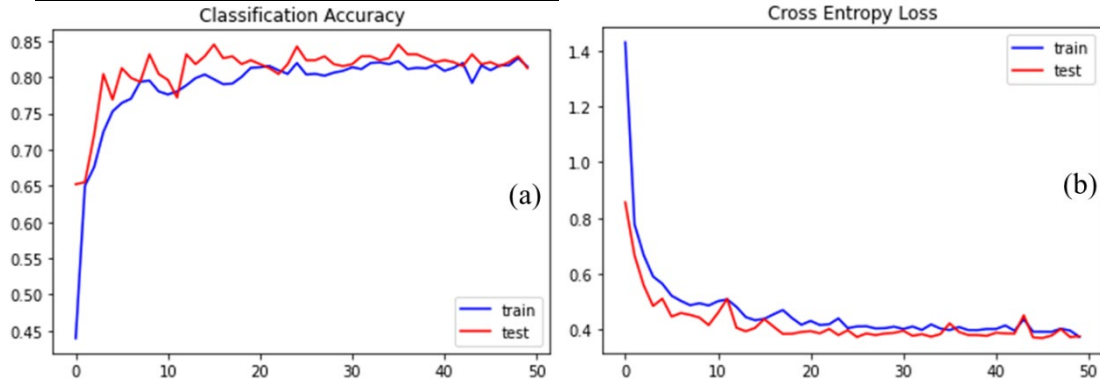
Figure 5-7. Convergence of the training and validation process of VGG19: (**a**) accuracy and (**b**) cross-entropy loss (Source: Adeniji et al. (2022) with permission of CC BY 2.0)

5.6 SUMMARY AND CONCLUSIONS

The main contribution of this chapter is the presentation of a novel approach for converting AE signals extracted during machining to time-frequency scalograms and executing further analysis with classification into different cutting modes using CNN models. This approach offers new possibilities for real-time, low-cost, and non-destructive

(NDE) quality monitoring of critical surface features when manufacturing high-value components.

- The CNN model developed in this work successfully classified the cutting mode during titanium aluminide into three different quality categories: good, marginal, and poor quality created using the crack depth information.
- A total of 42 AE signals of 80ms each were generated from seven different depths of cut (1, 3, 5, 7, 9, 14, 21 µm). These AE signals were then segmented into a sequence of 40 signals with 2ms each and converted to scalograms of 227 x 227pixels. These images were passed to the CNN algorithm and split using a ratio of 60:20:20 for the training, evaluation, and testing dataset, respectively.
- The results show that the scalogram-CNN model achieves a state-of-art accuracy. Also, the segmented scalogram and transfer learning approach give flexibility to the amount of data needed for adequate model training and validation.
- Ultimately, the wear condition during titanium aluminide machining can be estimated with acoustic emission and machine learning integration, with a predictive accuracy of 80.83%.

The adopted approach provides a straightforward but accurate monitoring and potential process control capability. While the present work dealt with second-generation *TiAl* alloys, our technique presented can be extended to future material variants of *TiAl* alloys, such as the third-generation alloys studied by Beranoagirre(Beranoagirre et al., 2019). It is worth noting that the future industrial implementation of the proposed paradigm will require custom sensor-integrated tool holders or fixtures to ensure consistent signal quality and attenuation. Nevertheless, the technique is not limited to monitoring surface finish during titanium aluminide machining. It could, in principle, be adopted for a wide variety of manufacturing processes and material systems that exhibit physical mechanisms (e.g., energy release during crack formation or tribological phenomena) that correlate with the quality and performance of the manufactured components. This furthermore includes potential future applications for use-stage asset condition monitoring, such as real-time detection of cracks during the operation of turbines.

CHAPTER 6.

METRICS-BASED PRODUCTION PERFORMANCE ANALYSIS

6.1 SCOPE AND INTRODUCTION

Metrics are used to evaluate a strategy, process, product, or system's efficiency, performance, progress, or quality. When several performance areas, such as economic, environmental, and social issues, must be reviewed for overall sustainability, a range of metrics will be required. They must be grouped into an effective structure to help improve decision-making. Thus, comprehensive frameworks and measurements must assess sustainable manufacturing performance at the product, process, and system levels (Huang and Badurdeen, 2018). According to Jawahir et al. (2020), the interconnection between machining process performance metrics makes developing predictive models limited and complex. Precise forecast factors compound this challenge for maximum productivity and quality under real-world situations. In this chapter, a simple case study was designed to test and compare the performance of the proposed DPT method to the existing state of process development, i.e., empirical modeling. While the precise values utilized in this research were not generated from actual production data, they were developed after extensive consultation with industry partners and *TiAl* machining specialists. Our research aims to assess the influence of apparently minor DPT improvements and trade-offs on the overall resource and energy efficiency of a low-pressure turbine (LPT) manufacturing process. The processing strategies and their performance were assessed for product quality, process time, cost, and material and energy consumption.

6.1.1 Analysis of Resource-Efficiency Metrics

A simple case study was designed to evaluate and compare the performance of the proposed DPT approach to the current process development status quo, i.e., empirical analysis. While the exact numbers used in this study were not derived from actual production data, they were developed after extensive consultation with industry partners and *TiAl* machining experts. Our analysis seeks to assess the impact of seemingly minor DPT improvements and trade-offs on the overall resource and energy efficiency of a

generic low-pressure turbine (LPT) manufacturing process. To accomplish this, the processing strategies and their performance were assessed in terms of product quality, process time, cost, and material and energy utilization.

6.1.1.1 *Product Quality and Material Utilization*

For LPT applications, product quality is of chief importance. Any surface damage (e.g., machining-induced cracks and grain pull-out) may lead to a turbine engine's catastrophic failure and must thus be avoided at any cost. As a result, thorough quality control (QC) is required, and parts are individually inspected utilizing tailored non-destructive evaluation techniques, such as fluorescent penetrant testing (RadkowskiandSep, 2014). The numbers are shown in Table 6-1. Quality performance overviews were generated for DPT model validation purposes and represent the outcomes of an experimental validation campaign. The results of the proposed DPT approach and the status quo manufacturing process of an undisclosed (proprietary) industry partner were contrasted.

It should be noted that these data are not directly representative of actual production metrics because no full production has been completed using the novel DPT approach to date. Instead, based on the frequency and magnitude of machining-induced surface defects, the authors used lab-scale results to obtain reasonable estimates of the likely QC Pass, Fixable, and Scrap Rates (e.g., cracking, smearing, grain deformation). The quality check pass rate for the currently status quo was estimated to be around 90% and that of the proposed DPT to be around 95%, while it was assumed that the fixable rate of the DPT will be substantially better than the status quo, due to the presence of few and shallow cracks if any at all. The scrap rate for DPT is envisioned to be better due to improved fixable rate. The difference in QC pass rate, fixable rate, and scrap rate between the status quo and the DPT-optimized *TiAl* machining process is depicted in Table 6-1. Quality performance overview below.

117

Table 6-1. Quality performance overview

	QC Pass Rate	Fixable Rate	Scrap Rate
Status quo	90%	70%	3%
DPT	95%	80%	1%
Improvement	+5%	+10%	-2%

The DPT setup is assumed to have a modest 5% quality check pass rate (QCPR) improvement and 10% fixable rate (FR) improvement over the current status quo of empirical process optimization. The scrap rate (SR) was calculated from the quality check failure rate (QCFR) and FR as shown in Eqn. 26 and 27:

$$QCFR = 1 - QCPR \tag{26}$$

$$SR = QCFR(1 - FR) \tag{27}$$

As shown in Table 1, even the seemingly small increase in as-produced product quality has a significant improvement of approximately 2% reduced scrap rate, resulting in significantly improved material and embodied energy utilization within the DPT processing strategy.

6.1.1.2 *Process Time*

To determine the total process time (TPT), the time for machining a single LPT Blade (MT), quality check (QCT), rework (RWT), and delay time due to queue (QT) were all taken into account, as shown in Eqn. 28 and 29. Also, the possible part per hour was calculated with Equation 30.

$$QT = QCT[(1 - QCPR - SR) + 2(1 - QCPR)] \tag{28}$$

$$TPT = MT + QCT + RWT(1 - QCPR - SR) + QT \tag{29}$$

$$\frac{\text{Parts}}{\text{hour}} = \frac{60}{\text{TPT}} \tag{30}$$

6.1.1.3 Cost

The total cost for the status-quo and DPT across possible stages was computed using Equations 31-33, which consider the costs associated with machining, quality control, rework, and scrap.

$$RWC = RWC_{mins} * RWT \tag{31}$$

$$QCC = QCC_{mins} * QCT \tag{32}$$

$$SC = RMC * SR \tag{33}$$

where RWC, RWC_{mins}, RWT, QCC, QCC_{mins}, QCT, SC, and RMC denote total rework cost, rework cost per min, total rework time, quality control cost, quality control cost per min, total quality control time, scrap cost, and raw material cost. Based on an integrated accounting of the various process costs, the total machining cost (MC) can be described by Eqn. 34 below:

$$MC = (1 - QCPR - SR) * \big((MT * MC_{min}) + TC_{min}(MT + QCT)\big) \tag{34}$$

where MC_{min}, TC_{min}, MT, MC represent machining cost per min, tooling cost per min, machining time, and total machining cost, respectively

6.1.1.4 Energy consumption and embodied energy

The machining, quality control, and rework operations were measured by considering the energy consumption per unit time for each of these, which was assumed to be an average of 300 kJ/min. The total energy consumption was determined by subsequently considering how long each component spends in each operation. Considering that each operation takes several minutes, the overall energy consumption per part was in single-digit MJ order. Treloar et al. (1997) defined embodied energy (EE) as the energy required to provide a product (both directly and indirectly) through all processes upstream (i.e., traceable backward from the finished product to consideration of raw materials). Based on a review of the literature, the embodied energy of the cutting tool (EEC) material (tungsten carbide) was taken as 15 MJ/tool (Kirsch et al., 2014) and 500 MJ/kg (Norgate et al., 2007) for the workpiece material (EEW) $TiAl$, with an assumed weight (W_{LPTB}) of 0.1 kg for each LPT component (i.e., 50 MJ/component). While cutting tools are consumed

at an approximately constant rate of a certain number of tools per hour (i.e., fixed tool-life), the loss of embodied energy from $TiAl$ LPT components is taken as the scrap rate, as well as any energy introduced during the machining and quality control stages (both of which are about an order of magnitude smaller than the overall embodied energy).

With energy per min (EPM) assumed to be 300kJ, the energy metrics were calculated as follows:

$$ECT = \big(QCPR + RWT(1 - QCPR - SR)\big) \tag{35}$$

$$PEP = ECT * EPM \tag{36}$$

$$PEH = \frac{Part}{hour} * \frac{PE}{part} \tag{37}$$

$$TEP = ECT * TL \tag{38}$$

$$TEH = \frac{parts}{hour} * TEP * EEC \tag{39}$$

$$EEH_{LPTB} = SR * EEW * \frac{Part}{hour} * W_{LPTB} \tag{40}$$

$$TEE = PEH + TEH + EEH_{LPTB} \tag{41}$$

where ECT, PEP, PEH, EPM, TEP, TEH, EEC, EEH_{LPTB}, EEW denotes energy-consuming time, process energy per part, process energy per hour, energy per min, tooling energy per part, tooling energy per hour, embodied energy per cutting tool, embodied energy per blade, and total embodied energy consumption, respectively.

6.2   SUMMARY AND CONCLUSIONS

Based on the energy metrics analysis approach laid out in the previous section, a comparative analysis of the DPT approach's relative performance against the current status quo was conducted. As shown in Figure 6-1, the DPT approach has about 161% improvement over the status quo regarding the embodied energy of each LPT blade produced. Approximately 107% reduction in tooling energy per hour and 19% reduction

in process energy. Also, the total embodied energy (TEE) is significantly reduced by 84%. These improvements can be traced to reducing scrap rate (from 3% to 1%).
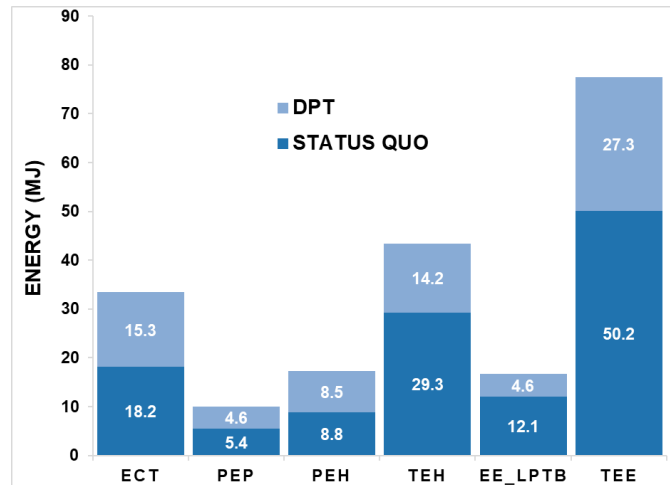
Figure 6-1. Energy performance for status quo & DPT

For respective operation time, the performance of a DPT approach is similar to the status quo as it pertains to the total machining time (MT), total quality time (QCT), and rework time (RWT), as shown in Figure 6-2. Also, it has about 93% queuing time and 15% total time improvement over the status quo. This performance improvement can be traced to a percentage increase in the LPT blades that passed the quality check at the first attempt with a DPT approach.
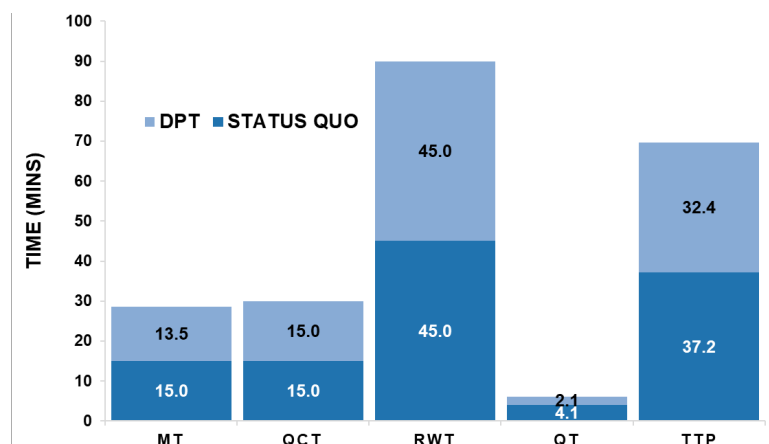
Figure 6-2. Time performance for status quo & DPT

Like the time metric result, the total machining cost, quality control cost, and total rework cost per part are almost identical. However, a DPT approach yielded a significant improvement of 93% in queuing cost and 2% in scrap cost, as shown in Figure 6-3.
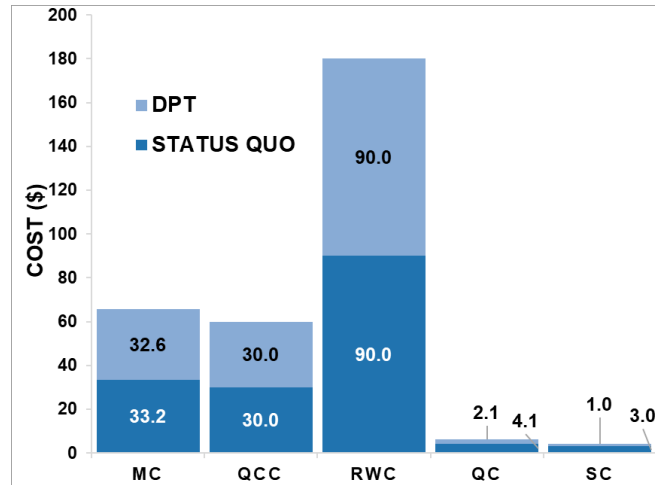
Figure 6-3. Cost performance for status quo & DPT

In this chapter, a novel process metric framework was proposed. Preliminary results showed an improvement of 84% in energy efficiency, 93% in process queuing time, 2% in scrap cost, and 93% in queuing cost compared with the low-pressure turbine blade finish machining status quo. In light of the need for more sustainable and resource-efficient manufacturing practices, the present work provides an example of how the proposed Digital Process Twin (DPT) methodology may enable transformative sustainability improvements at the process level. The DPT allows high-level consideration of various mutually interconnected metrics, as well as multi-objective optimization using artificial intelligence (AI) algorithms by tracking both environmental (energy, resources, etc.) and economic (costs, time, etc.) metrics. Future work will be needed to refine and validate specific sustainability metrics at the process level and consider the life-cycle implications of process-induced product quality (e.g., the impact of surface integrity on fatigue life or turbine energy consumption). Efforts are ongoing to expand their approach to a more comprehensive, system-level approach by considering both process and product performance, i.e., merging the DPT (manufacturing stage) and the Digital Twin (design and use stage) of turbine components.

CHAPTER 7.

CONCLUSIONS AND FUTURE WORK

7.1 SUMMARY OF MAJOR RESEARCH FINDINGS

The development and adoption of a digital process twin are envisioned to improve titanium aluminide alloys' machining/manufacturing process. However, to establish a machining DPT framework for titanium aluminide machining, different techniques such as in-situ process characterization, sensor technology, physics-based modeling, metrics-based production performance modeling, and data analytics have to be integrated. These components each have their unique contribution to the overall goal of creating a digital process twin for titanium aluminide machining. This research effort has focused mainly on implementing in-situ process characterization and data analytics techniques necessary for developing a DPT for machining processes. The characterization results covered in Chapter 4 of this work comprise high-speed video microscopy of the machining process, force data and acoustic emission extraction, post-mortem analysis of high-speed images for strain quantification, surface quality estimation, and mechanical fracture analysis of the machined surface captured on a high-speed testbed developed at the University of Kentucky. An initial set of parameters for crack-free machining of titanium aluminide was established using a sharp and worn carbide cutting tool with different edge geometry. The overall research summary is shown in Figure 7-1, however, the following conclusions were drawn from the in-situ characterization of the machining process:

- Captured high-speed images gave the capability for severe plastic deformation, sub-surface, strain, and strain rate characterization using Digital Image Correlation.
- This research discovered that the crack formation is microstructure dependent and that achieving a ductile cut in *TiAl* is possible. Experimental analysis showed (sub-) grain displacement/stress localization due to anisotropic material response to the thermo-mechanical loads of cutting. Grain pullout/cracking occurred preferentially when *TiAl* lamellae were approximately perpendicular to the shear plane, i.e., mechanical loading was applied along the weakest direction of the microstructure.

- When cutting brittle materials (such as *TiAl*), many researchers have observed a so-called 'critical uncut chip thickness' effect. When the value of the uncut chip exceeds this critical material-specific value, a fracture occurs. Experimental results show ductile cuts with few or no microcracks occur at chip thickness less than 5 microns, while chip thickness from 5 microns and upward shows a brittle cutting mode with prominent micro and macro cracks. Due to the critical uncut chip thickness, no significant fracture depth was recorded in worn tools at a chip thickness less than 5μm.

- To avoid surface cracks, the maximum uncut chip thickness should be limited to 1μm for a sharp tool, 3μm chip thickness for a 25μm VB worn tool, and about 5μm chip thickness for a 50μm VB worn carbide tool.

- Both sharp carbide and PCBN tools have a similar data profile; their cutting force magnitude increases as the chip thickness and tool edge radius rise. Critical uncut chip thickness characterization revealed that increasing tool-wear allows for increased feed rates. Fracture depths generally increase with increasing uncut chip thickness

- Also, *TiAl* needs to be machined at low cutting speeds (~30 m/min) to achieve reasonable tool-life and avoid thermal damage (transverse cracking due to thermal expansion/shock). Practically, *TiAl* needs to be machined at very low feed rates (~5-10 microns/rev) to remain below the single-digit critical uncut chip thickness threshold.

- Although industrial tool-life criteria are already relatively low (VB < 50 μm), in-situ characterization results show that a revised tool-life limit should be even lower to avoid thermal damage (e.g., less than 30 microns flank wear at 30 m/min)

In Chapter 5, the extracted acoustic emission signals were used for process monitoring via a scalogram-CNN approach. The transformation of extracted acoustic emission signals into scalograms was used to train a convolutional neural network for process feedback and monitoring. This approach provided an accurate process monitoring and potential process control capability, as described in Adeniji et al. (2022). It is worth noting that the future industrial implementation of this paradigm will require custom

sensor-integrated tool holders or fixtures to ensure consistent signal quality and attenuation. Nevertheless, the technique is not limited to monitoring surface finish during titanium aluminide machining. It could, in principle, be adopted for a wide variety of manufacturing processes and material systems that exhibit physical mechanisms (e.g., energy release during crack formation or tribological phenomena) that correlate with the quality and performance of the manufactured components. The DPT prospect further includes potential future applications for use-stage asset condition monitoring, such as real-time detection of cracks during the operation of turbines. In Chapter 6, the potential benefit of the proposed digital process twin paradigm against the industry's existing status quo for manufacturing a γ-*TiAl* low-pressure turbine blade. A DPT framework provides more sustainable and resource-efficient manufacturing practices, enabling transformative sustainability improvements at the process level. This was achieved by tracking environmental (energy, resources, etc.) and economic (costs, time, etc.) metrics. Future work to refine and validate specific sustainability metrics at the process level and consider life-cycle implications of process-induced product quality (e.g., surface integrity impacts on fatigue life or turbine energy consumption) will be required. Also, hile the present work dealt with second-generation *TiAl* alloys, the DPT technique presented can be extended to future variants of *TiAl* alloys and other difficult-to-machine materials.

Summary of Thesis Work

In-situ Process Sensors & Characterization
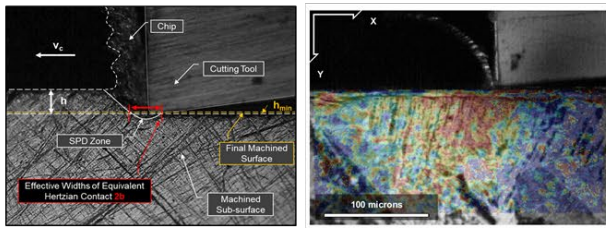
High-resolution machining microscopic images
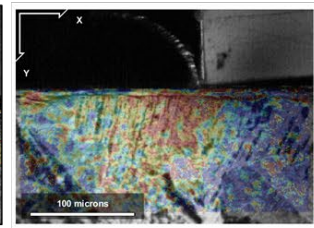
Sub-surface Characterization with Digital Image Correlation

Acoustic Emission Sensors

Surface Images of Machined Surface

Process Analysis

Tool-wear Effects on Process Performance
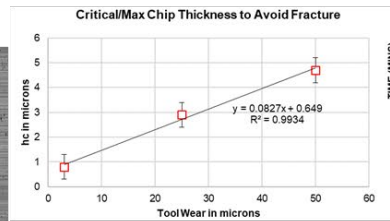
Mechanical Fracture Behavior
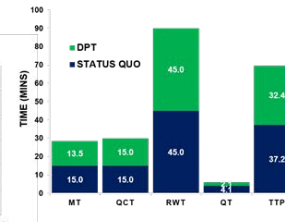
Metrics-Based Process Analysis

Data Analytics (ML)

Continuous Wavelet Transform

Scalograms
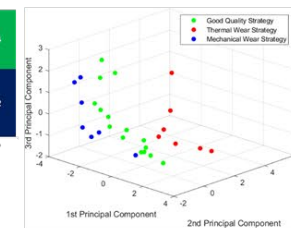
Principal Component Analysis
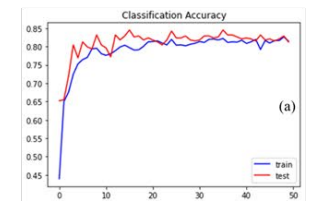
Convolutional Neural Network

Figure 7-1. Summary of thesis work

7.2   FUTURE WORK AND OUTLOOK

The adopted in-situ characterization approach provides a straightforward approach towards quickly developing a robust process understanding and enables the measurement of relevant model inputs to develop accurate predictive process models. When properly calibrated and validated, such models can run process simulations and generate sufficient data for a machine learning model. The computational models act significantly faster when arranged in a modular fashion since highly complex 'chip formation' simulations often predict various highly complex phenomena (e.g., chip serration) that may ultimately not be necessary to predict desired process metrics (e.g., surface cracking). The ML model must be carefully curated to account for process uncertainties while also learning from the simulated data in a converging manner. When these digital components of the DPT are appropriately integrated, the overall predictive capability will enable a future extension (extrapolation) to previously unforeseen scenarios, e.g., across a new range of process parameters.

While much work has been done in cyber-physical manufacturing systems and establishing a digital twin of manufactured components, much of these efforts fail to address the impact of unit manufacturing processes on a given component's physical properties (Leng et al., 2019; Uhlemann et al., 2017). A digital process twin framework, as identified by Ritto and Rochinha (2020), is created from the integration of three components (i) computational models and (ii) model calibration and validation using past and current process data (iii) process uncertainty quantification. Successful integration of these components provides a much-improved process planning, monitoring, and adjustment capability. However, the current effort to create an efficient and robust machining process model is plagued by a lack of realistic model inputs and a poor understanding of underlying process physics, as identified above. Also, traditional models are limited in accounting for varying process uncertainties. Therefore, to create a robust machining DPT, an efficient machining characterization setup, a simplified computational model, and real-time process deployment must be created.

In this context, this study proposes a new definition for a Digital Process Twin (DPT) as an accurate, fast, and efficient virtual process representation that considers the impact of a unit manufacturing process on the physical characteristics of a workpiece, fusing physically informed models and measured data to optimize a given process. This approach is intended to symbiotically augment the popular digital twin (DT) concept, which acts on a higher 'systems' level to digitally integrate the entire product life cycle. Thus, a DPT would be housed within the DT of a component and ultimately serve to inform design-stage optimization efforts, which are ultimately the key to improving the product, process, and system sustainability (Badurdeen et al.). Figure 7-2 illustrates the overall approach of calibrating the DPT with in-situ process characterization and leveraging AI to optimize process parameters across a wide range of process and resource efficiency metrics. The model input variables such as process forces, temperature, and material-specific data help calibrate pertinent process models. However, the models must be validated to ensure accuracy and robustness. The validated models simulate data for varying cutting conditions and train various ML algorithms. Integrated with the physics-based models would be a stochastic layer that helps to account for process uncertainties.
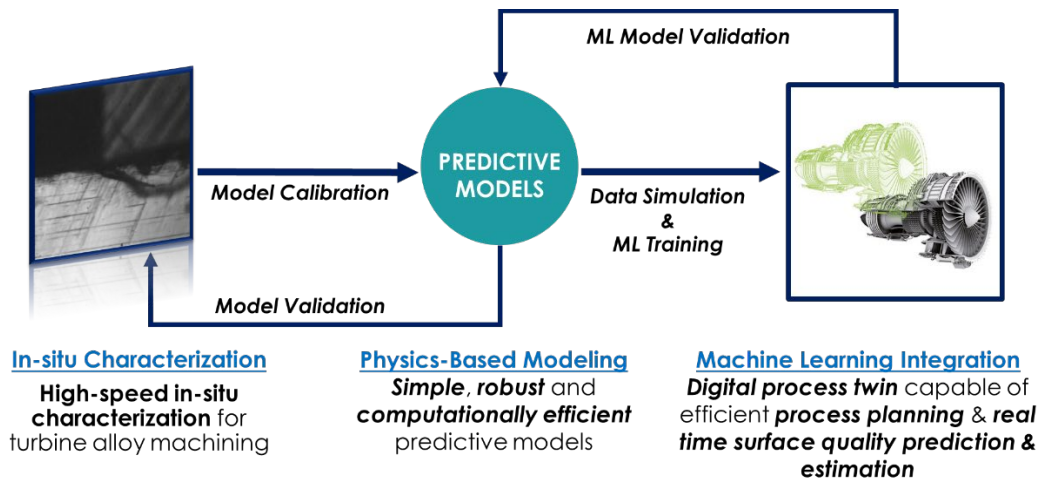
Figure 7-2. Proposed process schematic for a digital process twin of surface integrity in machining

In addition, a crucial and highly recommended improvement to the proposed AE-scalogram framework is the implementation and adoption of in-process custom sensor-

integrated tool holders or fixtures, which would help ensure consistent signal quality and attenuation in acoustic emission signal analysis. Also, while academic research in this field has recently gained ground (Suprock, 2011; Suprock et al., 2008; Xie et al., 2020), existing solutions are not driven by a process model and, in most cases, not affordable. It is recommended that the process model requirement determine which sensor should be integrated into the cutting tool. There is a range of brittle metals in which surface cracks and poor surface finish during machining are significant concerns. An excellent next step would be to evaluate the applicability of findings and framework from the present study to machining other difficult-to-machine alloys such as Inconel. The proposed DPT framework for machining may be an efficient means to achieve zero surface cracks, optimal productivity, and excellent surface finish in alloys preferred for aerospace applications. Lastly, the research approach in this study can be used to extract pertinent process models and develop functional physics based process models and DPT for other difficult-to-machine alloys.

APPENDIX

```python
#Data Manipulation Libraries
import numpy as np # linear algebra
import pandas as pd # data processing, CSV file I/O (e.g. pd.read_csv)
import re #regular expressions
from tqdm import tqdm
from datetime import datetime
#Read Images
import os
from skimage import io
from PIL import Image
import cv2
#Visualization
import matplotlib.pyplot as plt
import seaborn as sns
#Image copy
from shutil import copyfile
from random import seed
from random import random
import shutil
#Modelling
import tensorflow as tf
import sys
from matplotlib import pyplot
from keras.models import Sequential
from tensorflow.keras.utils import to_categorical
from keras.applications.vgg16 import VGG16
from keras.applications.vgg19 import VGG19
from tensorflow.keras.applications import EfficientNetB0
from tensorflow.keras import applications
from keras.layers import Conv2D,MaxPooling2D,Dense,Flatten,Dropout
from keras.models import Model
from tensorflow.keras.optimizers import SGD, Adam
from keras.preprocessing.image import ImageDataGenerator
from sklearn.metrics import  r2_score,roc_auc_score,f1_score,recall_score,precision_score,classification
_report, confusion_matrix,log_loss
```

```python
import random
# Image load
from keras.preprocessing.image import load_img
from keras.preprocessing.image import img_to_array
from keras.models import load_model
# Increase rows and columns visible on the notebook
pd.set_option('display.max_rows', 5000)
pd.set_option('display.max_columns', 200)
pd.set_option('max_colwidth', 100)
# import required libraries
import warnings
warnings.filterwarnings("ignore")

# Images in training directory
image_path = '../input/train-data-sharp/Train'
train_directories = os.listdir(image_path)
print("There are ",len(train_directories), " directories")
print(train_directories)

for category in train_directories:
    full_image_path = image_path + "/" +category + "/"
    print(category,len(os.listdir(full_image_path)))

image_categories = []
file_names =[]
image_names = []
# Loop across the directories having images.
for category in train_directories:
    #full_image_path = image_path +  category + "/" +category + "/"
    full_image_path = image_path + "/" +category + "/"
    # Retrieve the filenames from the all the  directories. OS package used.
    image_file_names = [os.path.join(full_image_path, f) for f in os.listdir(full_image_path)]
    # Read the labels and load them into an array
    for file in image_file_names:
        # Eliminate path from file name
        file_name = os.path.basename(file)
        image_categories.append(category)
        file_names.append(file)
        image_names.append(file_name)
```

131

```python
print("Images count ",len(file_names))
df = pd.DataFrame({'file_names': file_names, 'image_names': image_names,'image_categories':image_cate
gories}, columns=['file_names', 'image_names','image_categories'])
df.sample(5)

df.info()

#Function to upload and if need be resize the training images
def upload_train_images(image_path, categories ,height, width):
    images = []
    labels = []
    file_names =[]
    # Loop across the directories having images.
    for category in categories:
        # Append the  category directory into the main path
        full_image_path = image_path + "/" +category + "/"
        # Retrieve the filenames from the all the three wheat directories. OS package used.
        image_file_names = [os.path.join(full_image_path, f) for f in os.listdir(full_image_path)]
        # Read the images and load them into an array
        for file in image_file_names[0:100]:
            image=io.imread(file) #io package from SKimage package
            images.append(np.array(image))
            # Label for each image as per directory
            labels.append(category)
            file_names.append(file)


    return images, labels, file_names
height = 256
width = 256
train_images, train_categories, train_file_names  = upload_train_images(image_path,train_directories,heigh
t,width)
#Size and dimension of output image and labels
train_images = np.array(train_images)
train_categories = np.array(train_categories)
train_file_names = np.array(train_file_names)
#Check properties of uploaded images
print("Shape of training images is " + str(train_images.shape))
```

```python
print("Shape of training labels is " + str(train_categories.shape))
print("Shape of training labels is " + str(train_file_names.shape))
## Eliminate path from file name
# use regular expressions to extract the name of image
image_names = []
for i in train_file_names:
    fname = os.path.basename(i)
    image_names.append(fname)
#View images
image_names = np.array(image_names)
print(len(image_names))
image_names[0:5]
```

DISPLAY IMAGE

```python
import random
def show_train_images(images, train_categories, train_file_names,image_names,images_count):
    for i in range(images_count):
        index = int(random.random() * len(images))
        plt.axis('off')
        plt.imshow(images[index])
        plt.show()


        print("Size of this image is " + str(images[index].shape))
        print("Class of the image is " + str(train_categories[index]))
        print("Image path is " + str(train_file_names[index]))
        print("Image name is " + str(image_names[index]))
#Execute the function
print("Train images, sizes and class labels")
show_train_images(train_images, train_categories,train_file_names,image_names, 6)
```

Display A Batch of Images

```python
# show the image batch
def show_batch_train_images(images,train_categories,image_names):
    plt.figure(figsize=(20,15))
    for n in range(20):
        ax = plt.subplot(5,5,n+1)
        index = int(random.random() * len(images))
```

133

```python
        plt.imshow(images[index)
        title = train_categories[index],image_names[index]
        plt.title(title)
        plt.axis('off')
show_batch_train_images(train_images,train_categories,image_names)
plt.show()

#image categories
pd.Series(train_categories).value_counts().reset_index().values.tolist()

# some chart showing distribution
plt.figure(figsize = (15,8))
sns.countplot(df.image_categories)
plt.show()
```

Training And Validation Preparaation

```python
#Delete working directory if it already exists
def ignore_absent_file(func, path, exc_inf):
    except_instance = exc_inf[1]
    if isinstance(except_instance, FileNotFoundError):
        return
    raise except_instance
shutil.rmtree('/kaggle/working/David', onerror=ignore_absent_file)
# create training and validation directories
dataset_home = 'David/'
subdirs = ['train/', 'validation/']
for subdir in subdirs:
    # create label subdirectories
    for labldir in train_directories:
        newdir = dataset_home + subdir + labldir
        os.makedirs(newdir, exist_ok=True)
import random
seed = 1
val_ratio = 0.25
for index, row in df.iterrows():
    if row['image_categories'] != 'test':
        src = row['file_names']
        if random.random() < val_ratio:
```

```
        dst = '/kaggle/working/David/validation'+ '/' + row['image_categories'] + '/' +row['image_names']
    else:
        dst = '/kaggle/working/David/train'+ '/' + row['image_categories'] + '/' +row['image_names']
    copyfile(src, dst)


output_path = dst = '/kaggle/working/David/'
print("Validation images")
for category in train_directories[:20]:
    full_image_path = output_path +  'validation' + "/" +category + "/"
    print(category,len(os.listdir(full_image_path)))
print("Training images")
for category in train_directories[:20]:
    full_image_path = output_path +  'train' + "/" +category + "/"
    print(category,len(os.listdir(full_image_path)))
```

Modelling

Custom CNN with 3 layers

```
# define cnn model
def define_model():
    model = Sequential()
    model.add(Conv2D(32, (3, 3), activation='relu', kernel_initializer='he_uniform', padding='same', input_shape=(384, 512, 3)))
    model.add(MaxPooling2D((2, 2)))
    model.add(Dropout(0.2))
    model.add(Conv2D(64, (3, 3), activation='relu', kernel_initializer='he_uniform', padding='same'))
    model.add(MaxPooling2D((2, 2)))
    model.add(Dropout(0.2))
    model.add(Conv2D(128, (3, 3), activation='relu', kernel_initializer='he_uniform', padding='same'))
    model.add(MaxPooling2D((2, 2)))
    model.add(Dropout(0.2))
    model.add(Flatten())
    model.add(Dense(128, activation='relu', kernel_initializer='he_uniform'))
    model.add(Dropout(0.5))
    model.add(Dense(3, activation='softmax'))
    # compile model
    opt = SGD(lr=0.001, momentum=0.9)
```

```python
        #Compile the model
    model.compile(optimizer=opt, loss='categorical_crossentropy', metrics=['accuracy']) #sparse_categorical_crossentropy
    return model
# plot diagnostic learning curves
def summarize_diagnostics(history):
    # plot loss
    plt.subplot(211)
    plt.title('Cross Entropy Loss')
    plt.plot(history.history['loss'], color='blue', label='train')
    plt.plot(history.history['val_loss'], color='orange', label='test')
    # plot accuracy
    plt.subplot(212)
    plt.title('Classification Accuracy')
    plt.plot(history.history['accuracy'], color='blue', label='train')
    plt.plot(history.history['val_accuracy'], color='orange', label='test')
    # save plot to file
    filename = sys.argv[0].split('/')[-1]
    plt.savefig(filename + '_plot.png')
    plt.close()
# run the test harness for evaluating a model
def run_test_harness():
    # define model
    print("Define Model")
    model = define_model()
    # create data generator
    print("Creating Image Data Generator")
    datagen = ImageDataGenerator(rescale=1.0/255.0)
    # prepare iterators
    print("Preparing iterators")
    train_it = datagen.flow_from_directory('/kaggle/working/David/train', class_mode='categorical', batch_size=128, target_size=(384, 512)) #binary
    test_it = datagen.flow_from_directory('/kaggle/working/David/validation/', class_mode='categorical', batch_size=128, target_size=(384, 512))
    # fit model
    print("Fitting the model")
```

```python
    history = model.fit_generator(train_it, steps_per_epoch=len(train_it),validation_data=test_it, validation_
steps=len(test_it), epochs=50, verbose=1)
    model.save('baseline_marine.h5')
    class_dictionary = train_it.class_indices
    print("Testing the model")
    # evaluate model
    _, acc = model.evaluate_generator(test_it, steps=len(test_it), verbose=1)
    print('> %.3f' % (acc * 100.0))
    # learning curves
    summarize_diagnostics(history)
    return(history,class_dictionary)
#Execute the baseline model
#
model_history,class_dictionary = run_test_harness()

#plot Loss
plt.subplot(111)
plt.title('Cross Entropy Loss Plot')
plt.plot(model_history.history['loss'], color='blue', label='train')
plt.plot(model_history.history['val_loss'], color='red', label='test')
plt.legend()
plt.show()

#plot accuracy
plt.subplot(111)
plt.title('Classification Accuracy')
plt.plot(model_history.history['accuracy'], color='blue', label='train')
plt.plot(model_history.history['val_accuracy'], color='red', label='test')
plt.legend()
plt.show()
```

Add Augmentations

```python
# data augmentation on baseline we've  above.
# Create cnn model
def define_model():
    model = Sequential()
    model.add(Conv2D(32, (3, 3), activation='relu', kernel_initializer='he_uniform', padding='same', input_s
hape=(128, 128, 3)))
```

```python
    model.add(MaxPooling2D((2, 2)))
    model.add(Conv2D(64, (3, 3), activation='relu', kernel_initializer='he_uniform', padding='same'))
    model.add(MaxPooling2D((2, 2)))
    model.add(Flatten())
    model.add(Dense(64, activation='relu', kernel_initializer='he_uniform'))
    model.add(Dense(3, activation='sigmoid'))
    # compile model
    opt = SGD(lr=0.001, momentum=0.9)
    model.compile(optimizer=opt, loss='categorical_crossentropy', metrics=['accuracy'])
    return model
# plot diagnostic learning curves
def summarize_diagnostics(history):
    # plot loss
    pyplot.subplot(211)
    pyplot.title('Cross Entropy Loss')
    pyplot.plot(history.history['loss'], color='blue', label='train')
    pyplot.plot(history.history['val_loss'], color='orange', label='test')
    # plot accuracy
    pyplot.subplot(212)
    pyplot.title('Classification Accuracy')
    pyplot.plot(history.history['accuracy'], color='blue', label='train')
    pyplot.plot(history.history['val_accuracy'], color='orange', label='test')
    # save plot to file
    filename = sys.argv[0].split('/')[-1]
    pyplot.savefig(filename + '_plot.png')
    pyplot.close()
# run the test harness for evaluating a model
def run_test_harness():
    # define model
    model = define_model()
    # create data generators
    train_datagen = ImageDataGenerator(rescale=1.0/255.0, width_shift_range=0.1, height_shift_range=0.1,
horizontal_flip=True)
    test_datagen = ImageDataGenerator(rescale=1.0/255.0)

    # prepare iterators
```

```
train_it = train_datagen.flow_from_directory('/kaggle/working/David/train/',class_mode='categorical', ba
tch_size=64, target_size=(128, 128))
test_it = test_datagen.flow_from_directory('/kaggle/working/David/validation/',class_mode='categorical',
batch_size=64, target_size=(128, 128))
# fit model
history = model.fit(train_it, steps_per_epoch=len(train_it),validation_data=test_it, validation_steps=len(t
est_it), epochs=50, verbose=1) # Were 10 epochs earlier
# evaluate model
_, acc = model.evaluate(test_it, steps=len(test_it), verbose=1)
model.save('VGGmarine.h5')
print('> %.3f' % (acc * 100.0))
# learning curves
summarize_diagnostics(history)
return(history)
```

Augmentation Results

```
da_model_history = run_test_harness()

#Plot Cross Entropy Loss
plt.subplot(111)
plt.title('Cross Entropy Loss')
plt.plot(da_model_history.history['loss'], color='blue', label='train')
plt.plot(da_model_history.history['val_loss'], color='red', label='test')
plt.legend()
plt.show()

# plot accuracy
plt.subplot(111)
plt.title('Classification Accuracy')
plt.plot(da_model_history.history['accuracy'], color='blue', label='train')
plt.plot(da_model_history.history['val_accuracy'], color='red', label='test')
plt.legend()
plt.show()
```

Transfer Learning:VGG19

```
# Create cnn model
def vgg_model():
    # load model
```

```python
model = VGG19(include_top=False, input_shape=(224,224,3)) #weights='imagenet'. Crosscheck before
and after 384, 512 weights='imagenet',
    # mark loaded layers as not trainable
    for layer in model.layers:layer.trainable = False
    # add new classifier layers
    flat1 = Flatten()(model.layers[-1].output)
    class1 = Dense(128, activation='relu', kernel_initializer='he_uniform')(flat1)
    output = Dense(3, activation='softmax')(class1)
    # define new model
    model = Model(inputs=model.inputs, outputs=output)
    # compile model
    #opt = SGD(lr=0.001, momentum=0.9)
    opt = Adam(lr=0.001)
    model.compile(optimizer=opt, loss='categorical_crossentropy', metrics=['accuracy']) #sparse_categorica
l_crossentropy,
    return model
```

**Train on whole dataset and apply transfer learning and image augmentation model **

```python
#Delete directory if it exists.
# we create a combined directory with all the train and validation images used earlier for training.
#Then will need to do final training on all images
def ignore_absent_file(func, path, exc_inf):
    except_instance = exc_inf[1]
    if isinstance(except_instance, FileNotFoundError):
        return
    raise except_instance
shutil.rmtree('/kaggle/working/David/combined', onerror=ignore_absent_file)
#Create a directory combining both train and validation dataset
dataset_home = 'David/combined/'
# create label subdirectories
for labldir in train_directories:
    newdir = dataset_home + labldir
    os.makedirs(newdir, exist_ok=True)
# Copy files from input to combined directory.
for index, row in df.iterrows():
```

```python
    if row['image_categories'] != 'test':
        src = row['file_names']
        dst = '/kaggle/working/David/combined'+ '/' + row['image_categories'] + '/' +row['image_names']
        copyfile(src, dst)
# How many images in directories
output_path = dst = '/kaggle/working/David/combined'
for category in train_directories[:5]:
    full_image_path = output_path +   "/" +category + "/"
    print(full_image_path)
    print(category,len(os.listdir(full_image_path)))

model = vgg_model()
# create data generator
datagen = ImageDataGenerator(featurewise_center=True)
datagen.mean = [123.68, 116.779, 103.939]
# prepare iterator
train_it = datagen.flow_from_directory('/kaggle/working/David/combined/',class_mode='categorical', batch
_size=32, target_size=(224, 224))
print("Fitting the model")
# fit model
model.fit_generator(train_it, steps_per_epoch=len(train_it), epochs=100, verbose=1)
```

Resnet 50

```python
# Create cnn model
def resnet_model():
    # load model
    model = applications.resnet50.ResNet50(include_top=False, input_shape=(224,224,3)) #weights='image
net'. Crosscheck before and after 384, 512 weights='imagenet',
    # mark loaded layers as not trainable
    for layer in model.layers:layer.trainable = False
    # add new classifier layers
    flat1 = Flatten()(model.layers[-1].output)
    class1 = Dense(128, activation='relu', kernel_initializer='he_uniform')(flat1)
    output = Dense(3, activation='softmax')(class1)
    # define new model
    model = Model(inputs=model.inputs, outputs=output)
    # compile model
```

```python
#opt = SGD(lr=0.001, momentum=0.9)
opt = Adam(lr=0.001)
model.compile(optimizer=opt, loss='categorical_crossentropy', metrics=['accuracy']) #sparse_categorical_crossentropy,
    return model


model = vgg_model()
# create data generator
datagen = ImageDataGenerator(featurewise_center=True)
datagen.mean = [123.68, 116.779, 103.939]
# prepare iterator
train_it = datagen.flow_from_directory('/kaggle/working/David/combined/',class_mode='categorical', batch_size=32, target_size=(224, 224))
print("Fitting the model")
# fit model
model.fit_generator(train_it, steps_per_epoch=len(train_it), epochs=100, verbose=1)
```

APPLY NOW OUR MODELS IN TEST Data

```python
t_file_names =[]
t_file_path =[]
test_image_path = '../input/testmixed-sharp/Mixed'
test_image_file_names = [os.path.join(test_image_path, f) for f in os.listdir(test_image_path)] # Retrieve the filenames from the all the  directories. OS package used.
for tfile in test_image_file_names:          # Read the labels and load them into an array
    FILE = os.path.basename(tfile) ## Eliminate path from file name
    t_file_names.append(FILE)
    t_file_path.append(tfile)
#Create Test Dataframe
df_test = pd.DataFrame({'t_file_names': t_file_names,'t_file_path':t_file_path}, columns=['t_file_names','t_file_path'])
# load the image
test_images =[]
for index, row in df_test.iterrows():
    img = load_img(row['t_file_path'], target_size=(224, 224))
    img = img_to_array(img)
    img = img.reshape(1, 224, 224, 3)
```

```python
        test_images.append(np.array(img))

predictions =[]
for i in test_images:
    y_predict = model.predict(i,batch_size=8,verbose=0)
    predictions.append(y_predict)

def test_images():
    # load the image
    test_images =[]
    for index, row in df_test.iterrows():
        test_images.append(row['t_file_names'])
    return(test_images)
#Execute function
test_images = test_images()

column_names = []
labels = (train_it.class_indices)
dict_labels = dict((v,k) for k,v in labels.items())
for key, value in dict_labels.items():
    print(key, '->', value)
    column_names.append(value)
column_names.insert( 0, 'FILE');
column_names


df_FILE = pd.DataFrame(test_images)
df_FILE
print("predicted")
df_predicted = pd.DataFrame(np.concatenate(predictions))
df_predicted[:10]
print("submission")
submission = pd.concat([df_FILE, df_predicted], axis=1)
print("columns")
submission.columns =[column_names]
submission[:5]

submission['label']=submission[['Good','Marginal','Poor']].apply(lambda x: x.argmax(), axis=1)

submission.to_csv('s.csv',index=False)
submission=pd.read_csv('./s.csv')
```

```python
submission.info()

my_dict={0:'Good',1:"Marginal",2:'Poor'}

submission["label"] = submission["label"].apply(lambda x: my_dict[x])

#our prediction file

#can now prepare the actual labels from the test folder

# Images in training directory
image_path = '../input/test-data-sharp/Test'
test_directories = os.listdir(image_path)
print("There are ",len(test_directories), " directories")
print(test_directories)

# How many images in directories
for category in train_directories:
    full_image_path = image_path + "/" +category + "/"
    print(category,len(os.listdir(full_image_path)))

image_categories = []
file_names =[]
image_names = []
# Loop across the directories having images.
for category in test_directories:
    #full_image_path = image_path +  category + "/" +category + "/"
    full_image_path = image_path + "/" +category + "/"
    # Retrieve the filenames from the all the  directories. OS package used.
    image_file_names = [os.path.join(full_image_path, f) for f in os.listdir(full_image_path)]
    # Read the labels and load them into an array
    for file in image_file_names:
        # Eliminate path from file name
        file_name = os.path.basename(file)
        image_categories.append(category)
        file_names.append(file)
        image_names.append(file_name)
print("Images count ",len(file_names))
df = pd.DataFrame({'file_names': file_names, 'image_names': image_names,'image_categories':image_cate
gories}, columns=['file_names', 'image_names','image_categories'])
df

submission.rename(columns={'FILE':'image_names',inplace=True)
```

```python
submission=submission.sort_values(by=['image_names'])

df=df.sort_values(by=['image_names'])

#ACCURACY
def accuracy(y_true,y_pred):
    count=0
    for x,y in zip(y_true,y_pred):
        if x==y:
            count+=1
    return count/len(y_true)

from sklearn import metrics

accuracy(df['image_categories'],submission['label'])

metrics.accuracy_score(df['image_categories'],submission['label'])

metrics.f1_score(df['image_categories'],submission['label'],average='micro')

metrics.f1_score(df['image_categories'],submission['label'],average='macro')

metrics.precision_score(df['image_categories'],submission['label'],average='macro')

metrics.recall_score(df['image_categories'],submission['label'],average='micro')

from sklearn.metrics import confusion_matrix
from sklearn.metrics import ConfusionMatrixDisplay
confusion_matrix(df['image_categories'], submission['label'])
#disp=ConfusionMatrixDisplay(df['image_categories'], submission['label'])
```

REFERENCES

Abbasi, S. A., & Pingfa, F. (2015). Evaluating the effectiveness of PCD tools on machinability of titanium alloy Ti-6Al-4V in high speed end milling under various wet cutting conditions. In 2015 12th International Bhurban Conference on Applied Sciences and Technology (IBCAST),pp. 20-27.

Adaskina, A., Grigoriev, S., Vereschaka, A., Vereschaka, A., & Kashirtsev, V. (2013). Cemented carbides for machining of heat-resistant materials. Paper presented at the *Advanced Materials Research, 628*,pp. 37-42.

Adeniji, D., Oligee, K., & Schoop, J. (2022). A Novel Approach for Real-Time Quality Monitoring in Machining of Aerospace Alloy through Acoustic Emission Signal Transformation for DNN. *Journal of Manufacturing and Materials Processing, 6*(1),pp. 18.

Adeniji, D., & Schoop, J. (2022). In-Situ Calibrated Digital Process Twin Models for Resource Efficient Manufacturing. Journal of Manufacturing Science and Engineering, 144(4),p. 041008.

Administration, I., Group, E. P., Heginbotham, W., & Gogia, S. (1961). Metal cutting and the built-up nose. *Proceedings of the Institution of Mechanical Engineers, 175*(1),pp. 892-917.

Agarwal, H., Amaranath, A., Jamthe, Y., & Gururaja, S. (2015). An investigation of cutting mechanisms and strain fields during orthogonal cutting in CFRPs. *Machining Science and Technology, 19*(3),pp. 416-439.

Akhtar, W., Sun, J., Sun, P., Chen, W., & Saleem, Z. (2014). Tool wear mechanisms in the machining of Nickel based super-alloys: A review. *Frontiers of Mechanical Engineering, 9*(2),pp. 106-119.

Appel, F., Paul, J. D. H., & Oehring, M. (2011). *Gamma titanium aluminide alloys*: Wiley Online Library.

Arif, M., Rahman, M., & San, W. Y. (2013a). A study on the effect of tool-edge radius on critical machining characteristics in ultra-precision milling of tungsten carbide. *International Journal of Advanced Manufacturing Technology, 67*(5-8),pp. 1257-1265.

Arif, M., Xinquan, Z., Rahman, M., & Kumar, S. (2013b). A predictive model of the critical undeformed chip thickness for ductile-brittle transition in nano-machining of brittle materials. *International Journal of Machine Tools and Manufacture, 64*,pp. 114-122.

Arrazola, P., Özel, T., Umbrello, D., Davies, M., & Jawahir, I. S. (2013). Recent advances in modelling of metal machining processes. *CIRP Annals-Manufacturing Technology, 62*(2),pp. 695-718.

Arriola, I., Whitenton, E., Heigel, J., & Arrazola, P. (2011). Relationship between machinability index and in-process parameters during orthogonal cutting of steels. *CIRP Annals, 60*(1),pp. 93-96.

Aspinwall, D., Dewes, R., & Mantle, A. (2005). The machining of γ-TiAI intermetallic alloys. *CIRP Annals, 54*(1),pp. 99-104.

Attanasio, A., Umbrello, D., Cappellini, C., Rotella, G., & M'Saoubi, R. (2012). Tool wear effects on white and dark layer formation in hard turning of AISI 52100 steel. *Wear, 286*,pp. 98-107.

Axinte, D. A., & Dewes, R. C. (2002). Surface integrity of hot work tool steel after high speed milling-experimental data and empirical models. *Journal of Materials Processing Technology, 127*(3),pp. 325-335.

Badaloni, M., Rossi, M., Chiappini, G., Lava, P., & Debruyne, D. (2015). Impact of experimental uncertainties on the identification of mechanical material properties using DIC. *Experimental Mechanics, 55*(8),pp. 1411-1426.

Badurdeen, F., Srivastava, S., & Saunders, C. (2017). Predictive modeling for digitally-enabled, multi-criteria decision making for innovative product design & analysis for total lifecycle sustainability. In *DMDII-15-05-08 Quarterly Technical Review Report 4*.

Baizeau, T., Campocasso, S., Fromentin, G., & Besnard, R. (2017). Kinematic field measurements during orthogonal cutting tests via DIC with double-frame camera and pulsed laser lighting. *Experimental Mechanics, 57*(4),pp. 581-591.

Balcaen, R., Reu, P., Lava, P., & Debruyne, D. (2017). Stereo-DIC uncertainty quantification based on simulated images. *Experimental Mechanics, 57*(6),pp. 939-951.

Barile, C., Casavola, C., Pappalettera, G., & Vimalathithan, P. K. (2019). Characterization of adhesive bonded CFRP laminates using full-field digital image stereo-correlation and finite element analysis. *Composites Science and Technology, 169*,pp. 16-25.

Bartolotta, P. A., & Krause, D. L. (1999). Titanium aluminide applications in the high speed civil transport. National Aeronautics and Space Administration Technical Memorandum (NASA/TM−1999-209071).

Beberniss, T. J., & Ehrhardt, D. A. (2017). High-speed 3D digital image correlation vibration measurement: Recent advancements and noted limitations. *Mechanical Systems and Signal Processing, 86*,pp. 35-48.

Bentley, S., Mantle, A., & Aspinwall, D. (1999). The effect of machining on the fatigue strength of a gamma titanium aluminide intertmetallic alloy. *Intermetallics, 7*(8),pp. 967-969.

Beranoagirre, A., & de Lacalle, L. L. (2013). Grinding of gamma TiAl intermetallic alloys. *Procedia Engineering, 63*,pp. 489-498.

Beranoagirre, A., & Lopez de Lacalle, L. (2010). Optimising the milling of titanium aluminide alloys. *International Journal of Mechatronics and Manufacturing Systems, 3*(5-6),pp. 425-436.

Beranoagirre, A., Urbikain, G., Marticorena, R., Bustillo, A., & López de Lacalle, L. N. (2019). Sensitivity analysis of tool wear in drilling of titanium aluminides. *Metals, 9*(3),pp. 297.

Bewlay, B., Nag, S., Suzuki, A., & Weimer, M. (2016). TiAl alloys in commercial aircraft engines. *Materials at High Temperatures, 33*(4-5),pp. 549-559.

Bhattacharyya, A. (1964). Department of Applied Mechanics, Bengal Engineering College, Howrah. Journal of the Institution of Engineers (India).: Mechanical Engineering Division, 45,p. 262.

Bolcavage, A., Brown, P. D., Cedoz, R., Cooper, N., Deaton, C., Hartman, D. R., . . . Modgil, G. (2014). Integrated computational materials engineering from a gas turbine engine perspective. *Integrating Materials and Manufacturing Innovation, 3*(1),pp. 13.

Brinksmeier, E., Cammett, J., König, W., Leskovar, P., Peters, J., & Tönshoff, H. (1982). Residual stresses—measurement and causes in machining processes. *CIRP annals, 31*(2),pp. 491-510.

Brinksmeier, E., Klocke, F., Lucca, D. A., Sölter, J., & Meyer, D. (2014). Process Signatures–a new approach to solve the inverse surface integrity problem in machining processes. *Procedia CIRP, 13*,pp. 429-434.

Brinksmeier, E., Meyer, D., Heinzel, C., Lübben, T., Sölter, J., Langenhorst, L., . . . Kuschel, S. (2018). Process Signatures-The Missing Link to Predict Surface Integrity in Machining. *Procedia CIRP, 71*,pp. 3-10.

Brinksmeier, E., Schneider, E., Theiner, W., & Tönshoff, H. (1984). Nondestructive testing for evaluating surface integrity. *CIRP Annals, 33*(2),pp. 489-509.

Brown, R., & Komanduri, R. (1973). *An investigation of the performance of a quick-stop device for metal cutting studies.* Paper presented at the Proceedings of the Thirteenth International Machine Tool Design and Research Conference,p. 225.

Cai, S., Chen, Y., Ye, G., Jiang, M., Wang, H., & Dai, L. (2015). Characterization of the deformation field in large-strain extrusion machining. *Journal of Materials Processing Technology, 216*,pp. 48-58.

Calamaz, M., Coupard, D., & Girot, F. (2012). Strain field measurement in orthogonal machining of a titanium alloy. Paper presented at the *Advanced Materials Research, 498*,pp. 237-242.

Caprino, G., Nele, L., & Santo, L. (1996). Effect of tool wear on cutting forces in the orthogonal cutting of unidirectional glass fibre-reinforced plastics. *Composites Part A: Applied Science and Manufacturing, 27*(5),pp. 409-415.

Castellanos, S., Cavaleiro, A., Jesus, A. d., Neto, R. d., & Alves, J. L. (2019). Machinability of titanium aluminides: a review. *Proceedings of the Institution of Mechanical Engineers, Part L: Journal of Materials: Design and Applications, 233*(3),pp. 426-451.

Celik, O. N., Sert, A., Gasan, H., & Ulutan, M. (2018). Effect of cryogenic treatment on the microstructure and the wear behavior of WC-Co end mills for machining of

Ti6Al4V titanium alloy. *The International Journal of Advanced Manufacturing Technology, 95*(5),pp. 2989-2999.

Che-Haron, C. H. (2001). Tool life and surface integrity in turning titanium alloy. *Journal of Materials Processing Technology, 118*(1-3),pp. 231-237.

Chen, J., Yu, W., Zuo, Z., Li, Y., Chen, D., An, Q., . . . Chen, M. (2021). Tribological properties and tool wear in milling of in-situ TiB2/7075 Al composite under various cryogenic MQL conditions. *Tribology International, 160*,pp. 107021.

Cheng, W., Outeiro, J., Costes, J.-P., M'Saoubi, R., Karaouni, H., & Astakhov, V. (2019). A constitutive model for Ti6Al4V considering the state of stress and strain rate effects. *Mechanics of Materials, 137*,pp. 103103.

Childs, T. (1971). A new visio-plasticity technique and a study of curly chip formation. *International Journal of Mechanical Sciences, 13*(4),pp. 373-387.

Clemens, H., & Mayer, S. (2013). Design, processing, microstructure, properties, and applications of advanced intermetallic TiAl alloys. *Advanced Engineering Materials, 15*(4),pp. 191-215.

Clemens, H., & Mayer, S. (2014). Development status, applications and perspectives of advanced intermetallic titanium aluminides. Paper presented at the *Materials Science Forum, 783*,pp. 15-20.

Clemens, H., & Mayer, S. (2016). Intermetallic titanium aluminides in aerospace applications–processing, microstructure and properties. *Materials at High Temperatures, 33*(4-5),pp. 560-570.

Davis, B., Dabrow, D., Ifju, P., Xiao, G., Liang, S. Y., & Huang, Y. (2018). Study of the shear strain and shear strain rate progression during titanium machining. *Journal of Manufacturing Science and Engineering, 140*(5),p. 051007.

Denkena, B., Boehnke, D., & de Leon, L. (2008). Machining induced residual stress in structural aluminum parts. *Production Engineering, 2*(3),pp. 247-253.

Denkena, B., Krödel, A., & Beblein, S. (2021). A novel approach to determine the velocity dependency of the friction behavior during machining by means of digital particle image velocimetry (DPIV). *CIRP Journal of Manufacturing Science and Technology, 32*,pp. 81-90.

Denkena, B., & Meyer, R. (2009). An approach to reduce the influence of tool wear on workpiece properties during hard turning. *International Journal of Microstructure and Materials Properties, 4*(5-6),pp. 605-614.

Devillez, A., Schneider, F., Dominiak, S., Dudzinski, D., & Larrouquere, D. (2007). Cutting forces and wear in dry machining of Inconel 718 with coated carbide tools. *Wear, 262*(7-8),pp. 931-942.

Dhananchezian, M., Kumar, M. P., & Sornakumar, T. (2011). Cryogenic Turning of AISI 304 Stainless Steel with Modified Tungsten Carbide Tool Inserts. *Materials and Manufacturing Processes, 26*(5),pp. 781-785.

Dimiduk, D., Martin, P., & Dutton, R. (2003). *Accelerated insertion of materials: Gamma alloys pose challenges, but are really not unique.* Paper presented at the Proceeding of the 2003 TMS Annual Meeting & Exhibition: 3rd International Symposium on Gamma Titanium Aluminides, San Diego, CA, USA,pp. 2-6.

Doetz, M., eun Lee, J., Dambon, O., Klocke, F., Langenbach, E., & Faehnle, O. (2018). Process window analysis of ductile mode machining of binderless tungsten carbide molds. In *Optical Manufacturing and Testing XII, 10742*,p. 107420F.

Dogra, M., Sharma, V., & Dureja, J. (2011). Effect of tool geometry variation on finish turning-A Review. *Journal of Engineering Science & Technology Review, 4*(1),pp. 1-13.

Ee, K., Li, P., Balaji, A., Jawahir, I., & Stevenson, R. (2006). Performance-based predictive models and optimization methods for turning operations and applications: part 1—tool wear/tool life in turning with coated grooved tools. *Journal of Manufacturing Processes, 8*(1),pp. 54-66.

Efe, M., Moscoso, W., Trumble, K. P., Compton, W. D., & Chandrasekar, S. (2012). Mechanics of large strain extrusion machining and application to deformation processing of magnesium alloys. *Acta Materialia, 60*(5),pp. 2031-2042.

El-Wardany, T., Kishawy, H., & Elbestawi, M. (2000). Surface integrity of die material in high speed hard machining, Part 2: microhardness variations and residual stresses. *J. Manuf. Sci. Eng., 122*(4),pp. 632-641.

Ellis, J., Kirk, R., & Barrow, G. (1969). The development of a quick-stop device for metal cutting research. *International Journal of Machine Tool Design and Research, 9*(3),pp. 321-339.

Ezugwu, E. O. (2005). Key improvements in the machining of difficult-to-cut aerospace superalloys. *International Journal of Machine Tools & Manufacture, 45*(12-13),pp. 1353-1367.

Fang, N., & Jawahir, I. S. (2002). An analytical predictive model and experimental validation for machining with grooved tools incorporating the effects of strains, strain-rates, and temperatures. *CIRP Annals - Manufacturing Technology, 51*(1),pp. 83-86.

Field, M. & Kahles, J.F. (1971). Review of Surface Integrity of Machined Components. *Annals of the CIRP, 20*(2),pp. 153-162.

Field, M., Kahles, J.F. & Cammett, J.T. (1972). Review of measuring methods for surface integrity', *Annals of the CIRP, 21*,pp.219–238.

Fu, Y., Zhang, Y., Gao, Y., Gao, H., Mao, T., Zhou, H., & Li, D. (2017). Machining vibration states monitoring based on image representation using convolutional neural networks. *Engineering Applications of Artificial Intelligence, 65*,pp. 240-251.

George, E., Yamaguchi, M., Kumar, K., & Liu, C. (1994). Ordered intermetallics. *Annual Review of Materials Science, 24*(1),pp. 409-451.

Ghosh, R., Dillon Jr, O., & Jawahir, I. (1998). An investigation of 3-D curled chip in machining-Part 1: A mechanics-based analytical model. *Machining Science and Technology, 2*(1),pp. 91-116.

Glaessgen, E., & Stargel, D. (2012). *The digital twin paradigm for future NASA and US Air Force vehicles.* Paper presented at AAIA 53rd Structures, Structural Dynamics, and Materials Conference, Honolulu, Hawaii,p. 1818.

Gnanamanickam, E. P., Lee, S., Sullivan, J. P., & Chandrasekar, S. (2009). Direct measurement of large-strain deformation fields by particle tracking. *Measurement Science and Technology, 20*(9),pp. 095710.

Grieves, M. (2014). Digital twin: manufacturing excellence through virtual factory replication. *White paper, 1*,pp. 1-7.

Grzesik, W. (2008). Influence of tool wear on surface roughness in hard turning using differently shaped ceramic tools. *Wear, 265*(3-4),pp. 327-335.

Guo, Y., Compton, W. D., & Chandrasekar, S. (2015). In situ analysis of flow dynamics and deformation fields in cutting and sliding of metals. *J Proc. R. Soc. A, 471*(2178),pp. 20150194.

Guo, Y., Efe, M., Moscoso, W., Sagapuram, D., Trumble, K., & Chandrasekar, S. (2012). Deformation field in large-strain extrusion machining and implications for deformation processing. *Scripta Materialia, 66*(5),pp. 235-238.

Haidar, J., Gnanarajan, S., & Dunlop, J. B. (2009). Direct production of alloys based on titanium aluminides. *Intermetallics, 17*(8),pp. 651-656.

Harzallah, M. (2018). *Caractérisation in-situ et modélisation des mécanismes et couplages thermomécaniques en usinage: application à l'alliage de titane Ti-6Al-4V* (Doctoral dissertation, Ecole des Mines d'Albi-Carmaux).

Harzallah, M., Pottier, T., Gilblas, R., Landon, Y., Mousseigne, M., & Senatore, J. (2018). A coupled in-situ measurement of temperature and kinematic fields in Ti-6Al-4V serrated chip formation at micro-scale. *International Journal of Machine Tools and Manufacture, 130*,pp. 20-35.

Hastings, W. (1967). A new quick-stop device and grid technique for metal cutting research. *Annals of CIRP, 15*,pp. 109-116.

Helfrick, M. N., Niezrecki, C., Avitabile, P., & Schmidt, T. (2011). 3D digital image correlation methods for full-field vibration measurement. *Mechanical Systems and Signal Processing, 25*(3),pp. 917-927.

Herbert, E. G. (1928). Cutting tools research committee: report on machinability. *Proceedings of the Institution of Mechanical Engineers, 115*(1),pp. 775-825.

Hijazi, A., & Madhavan, V. (2008). A novel ultra-high speed camera for digital image processing applications. *Measurement Science and Technology, 19*(8),pp. 085503.

Houchuan, Y., Zhitong, C., & ZiTong, Z. (2015). Influence of cutting speed and tool wear on the surface integrity of the titanium alloy Ti-1023 during milling. *The*

International Journal of Advanced Manufacturing Technology, 78(5-8),pp. 1113-1126.

Hoult, N. A., Take, W. A., Lee, C., & Dutton, M. (2013). Experimental accuracy of two dimensional strain measurements using digital image correlation. *Engineering Structures, 46*,pp. 718-726.

Hua, J., Umbrello, D., & Shivpuri, R. (2006). Investigation of cutting conditions and cutting edge preparations for enhanced compressive subsurface residual stress in the hard turning of bearing steel. *Journal of Materials Processing Technology, 171*(2),pp. 180-187.

Huang, A., & Badurdeen, F. (2018). Metrics-based approach to evaluate sustainable manufacturing performance at the production line and plant levels. *Journal of Cleaner Production, 192*,pp. 462-476.

Huang, Y., Lee, K.-M., Ji, J., & Li, W. (2020). Digital Image Correlation based on Primary Shear Band Model for Reconstructing Displacement, Strain and Stress Fields in Orthogonal Cutting. *IEEE/ASME Transactions on Mechatronics,25*(4),pp. 2088-2099.

Jaspers, S. P. F. C., & Dautzenberg, J. H. (2002). Material behaviour in conditions similar to metal cutting: flow stress in the primary shear zone. *Journal of Materials Processing Technology, 122*(2–3),pp. 322-330.

Jawahir, I., Schoop, J., Kaynak, Y., Balaji, A., Ghosh, R., & Lu, T. (2020). Progress Toward Modeling and Optimization of Sustainable Machining Processes. *ASME Journal of Manufacturing Science and Engineering, 142*(11),p. 110811.

Jawahir, I., & Wang, X. (2007). Development of hybrid predictive models and optimization techniques for machining operations. *Journal of Materials Processing Technology, 185*(1-3),pp. 46-59.

Jawahir, I. S., Brinksmeier, E., M'Saoubi, R., Aspinwall, D. K., Outeiro, J. C., Meyer, D., . . . Jayal, A. D. (2011). Surface integrity in material removal processes: Recent advances. *CIRP Annals - Manufacturing Technology, 60*(2),pp. 603-626.

Jones, D., Snider, C., Nassehi, A., Yon, J., & Hicks, B. (2020). Characterising the Digital Twin: A systematic literature review. *CIRP Journal of Manufacturing Science and Technology, 29*,pp. 36-52.

Kececioglu, D. (1958). *Shear-strain rate in metal cutting and its effects on shear-flow stress.* Transactions of the American Society of Mechanical Engineers, 80(1),pp. 158-167.

Kim, D.-H., Kim, T. J. Y., Wang, X., Kim, M., Quan, Y.-J., Oh, J. W., . . . Ahn, S.-H. (2018). Smart Machining Process Using Machine Learning: A Review and Perspective on Machining Industry. *International Journal of Precision Engineering and Manufacturing-Green Technology, 5*(4),pp. 555-568.

Kim, J., & Hwangbo, H. (2018). Sensor-based real-time detection in vulcanization control using machine learning and pattern clustering. Sensors, 18(9),p. 3123.

Kim, Y.-W. (1989). Intermetallic alloys based on gamma titanium aluminide. *Jom, 41*(7),pp. 24-30.

Kirsch, B., Effgen, C., Büchel, M., & Aurich, J. (2014). Comparison of the embodied energy of a grinding wheel and an end mill. *Procedia CIRP, 15,*pp. 74-79.

Kishawy, H., & Elbestawi, M. (2001). Tool wear and surface integrity during high-speed turning of hardened steel with polycrystalline cubic boron nitride tools. *Proceedings of the Institution of Mechanical Engineers, Part B: Journal of Engineering Manufacture, 215*(6),pp. 755-767.

Kobayashi, H., Konda, N., Sutep, J.-A. K., Horikawa, K., & Yamauchi, T. (2015). Fatigue crack extension in four-point bending test for steels imitated heat affected zone. *Zairyo/Journal of the Society of Materials Science, Japan, 64*(4),pp. 323-329.

Komanduri, R., Schroeder, T., Hazra, J., Von Turkovich, B. F., & Flom, D. G. (1982). On the catastrophic shear instability in high-speed machining of an AISI 4340 steel. pp. 121-131

Lapin, J. (2009). TiAl-based alloys: Present status and future perspectives. In *Conference proceedings METAL* (Vol. 19, No. 21.5, p. 2009).

Lazoglu, I., Ulutan, D., Alaca, B., Engin, S., & Kaftanoglu, B. (2008). An enhanced analytical model for residual stress prediction in machining. *CIRP Annals, 57*(1),pp. 81-84.

Lee, J., Noh, S. D., Kim, H. J., & Kang, Y. S. (2018). Implementation of cyber-physical production systems for quality prediction and operation control in metal casting. Sensors, 18(5), p.1428.

Lee, S., Hwang, J., Shankar, M. R., Chandrasekar, S., & Compton, W. D. (2006). Large strain deformation field in machining. *Metallurgical and Materials Transactions A, 37*(5),pp. 1633-1643.

Leng, J., Zhang, H., Yan, D., Liu, Q., Chen, X., & Zhang, D. (2019). Digital twin-driven manufacturing cyber-physical system for parallel controlling of smart workshop. *Journal of Ambient Intelligence and Humanized Computing, 10*(3),pp. 1155-1166.

Li, K. M., & Liang, S. Y. (2005). Predictive models for flank wear in near dry machining. In *ASME International Mechanical Engineering Congress and Exposition* (Vol. 42231, pp. 49-57).

Li, M., Li, S., & Yang, X. (2020). The influence of machining processes on strain distribution and progressive failure characteristics when producing holes in CFRP. *Composite Structures, 238,*pp. 111994.

Li, W., Guo, Y., Barkey, M., & Jordon, J. (2014). Effect tool wear during end milling on the surface integrity and fatigue life of Inconel 718. *Procedia CIRP, 14,*pp. 546-551.

Liang, S., & Su, J.-C. (2007). Residual stress modeling in orthogonal machining. *CIRP Annals, 56*(1),pp. 65-68.

Liang, S. Y., Hanna, C. R., & Chao, R.-M. (2008). *Achieving machining residual stresses through model-driven planning of process parameters.* Paper presented at the Transactions of the North American Manufacturing Research Institution of SME,pp. 445-452.

List, G., Sutter, G., Bi, X., Molinari, A., & Bouthiche, A. (2013). Strain, strain rate and velocity fields determination at very high cutting speed. *Journal of Materials Processing Technology, 213*(5),pp. 693-699.

Liu, C., & Barash, M. (1976). The mechanical state of the sublayer of a surface generated by chip-removal process—Part 1: Cutting with a sharp tool. *Journal of Engineering for Industry, 98*(4),pp. 1192-1199.

Liu, F., Lin, X., Huang, C., Song, M., Yang, G., Chen, J., & Huang, W. (2011). The effect of laser scanning path on microstructures and mechanical properties of laser solid formed nickel-base superalloy Inconel 718. *Journal of Alloys and Compounds, 509*(13),pp. 4505-4509.

Liu, K., & Li, X. (2001). Ductile cutting of tungsten carbide. *Journal of Materials Processing Technology, 113*(1),pp. 348-354.

M'saoubi, R., Outeiro, J. C., Chandrasekaran, H. O. W. D., Dillon Jr, O. W., & Jawahir, I. S. (2008). A review of surface integrity in machining and its impact on functional performance and life of machined products. International Journal of Sustainable Manufacturing, 1(1-2), pp. 203-236.

Mantle, A., & Aspinwall, D. (1997). Surface integrity and fatigue life of turned gamma titanium aluminide. *Journal of Materials Processing Technology, 72*(3),pp. 413-420.

Mantle, A. L., & Aspinwall, D. K. (2000). Cutting force evaluation when high speed end milling a gamma titanium aluminide intermetallic alloy. *Intermetallics and superalloys, 10*,pp. 209-215.

Matsuda, Y., Fujiwara, Y., & Fujii, Y. (2018). Strain analysis near the cutting edge in orthogonal cutting of hinoki (Chamaecyparis obtusa) using a digital image correlation method. *Journal of Wood Science, 64*(5),pp. 566-577.

McGee, F. J. (1961). Machining tungsten with carbides. *Engineers' Digest, 22*(1),pp. 90105.

McKinley, P., Sinha, A., & Kamke, F. A. (2019). Understanding the effect of weathering on adhesive bonds for wood composites using digital image correlation (DIC). *Holzforschung, 73*(2),pp. 155-164.

Meinhart, C. D., Wereley, S. T., & Santiago, J. G. (1999). PIV measurements of a microchannel flow. *Experiments in fluids, 27*(5),pp. 414-419.

Melkote, S. N., Grzesik, W., Outeiro, J., Rech, J., Schulze, V., Attia, H., . . . Saldana, C. (2017). Advances in material and friction data for modelling of metal machining. *CIRP Annals - Manufacturing Technology, 66*(2),pp. 731-754.

Muñoz-Sánchez, A., Canteli, J., Cantero, J., & Miguélez, M. (2011). Numerical analysis of the tool wear effect in the machining induced residual stresses. *Simulation Modelling Practice and Theory, 19*(2),pp. 872-886.

Najmi, A.-H., & Sadowsky, J. (1997). The continuous wavelet transform and variable resolution time-frequency analysis. *Johns Hopkins APL Technical Digest, 18*(1),pp. 134-140.

Neupane, D., Kim, Y., & Seok, J. (2021). Bearing Fault Detection Using Scalogram and Switchable Normalization-Based CNN (SN-CNN). IEEE Access, 9, pp. 88151-88166.

Norgate, T., Jahanshahi, S., & Rankin, W. (2007). Assessing the environmental impact of metal production processes. *Journal of Cleaner Production, 15*(8-9),pp. 838-848.

Oh, D., & Jo, Y. (2019). *EMG-based hand gesture classification by scale average wavelet transform and CNN.* Paper presented at the 2019 19th International Conference on Control, Automation and Systems (ICCAS),pp. 533-538.

Osorio-Pinzon, J. C., Abolghasem, S., & Casas-Rodriguez, J. P. (2019). Predicting the Johnson Cook constitutive model constants using temperature rise distribution in plane strain machining. *The International Journal of Advanced Manufacturing Technology, 105*(1),pp. 279-294.

Outeiro, J., Kandibanda, R., Pina, J., Dillon Jr, O., & Jawahir, I. (2010). Size-effects and surface integrity in machining and their influence on product sustainability. *International Journal of Sustainable Manufacturing, 2*(1),pp. 112-126.

Oxley, P. (1961). Mechanics of metal cutting. *International Journal of Machine Tool Design and Research, 1*(1-2),pp. 89-97.

Özel, T., Sima, M., Srivastava, A., & Kaftanoglu, B. (2010). Investigations on the effects of multi-layered coated inserts in machining Ti–6Al–4V alloy with experiments and finite element simulations. *CIRP Annals, 59*(1),pp. 77-82.

Özel, T., & Zeren, E. (2006). A methodology to determine work material flow stress and tool-chip interfacial friction properties by using analysis of machining. *Journal of Manufacturing Science and Engineering, 128*(1),pp. 119-129.

Özel, T., & Zeren, E. (2007). Finite element modeling the influence of edge roundness on the stress and temperature fields induced by high-speed machining. *The International Journal of Advanced Manufacturing Technology, 35*(3-4),pp. 255-267.

ÖZER, A., & Bahceci, E. (2009). Machinability of AISI 410 martensitic stainless steels depending on cutting tool and coating. *Journal of the Faculty of Engineering and Architecture of Gazi University*, 24(4),pp. 693-698.

Palanca, M., Brugo, T. M., & Cristofolini, L. (2015). Use of digital image correlation to investigate the biomechanics of the vertebra. *Journal of Mechanics in Medicine and Biology, 15*(02),pp. 1540004.

Palanca, M., Tozzi, G., & Cristofolini, L. (2016). The use of digital image correlation in the biomechanical area: a review. *International biomechanics, 3*(1),pp. 1-21.

Palmer, W., & Oxley, P. (1959). Mechanics of orthogonal machining. *Proceedings of the Institution of Mechanical Engineers Part C-Journal of Mechanical Engineering Science, 173*(1),pp. 623-654.

Pan, B. (2011). Recent progress in digital image correlation. *Experimental Mechanics, 51*(7),pp. 1223-1235.

Pervaiz, S., Rashid, A., Deiab, I., & Nicolescu, M. (2014). Influence of tool materials on machinability of titanium- and nickel-based alloys: A review. *Materials and Manufacturing Processes, 29*(3),pp. 219-252.

Philip, P. (1971). Study of the performance characteristics of an explosive quick-stop device for freezing cutting action. *International Journal of Machine Tool Design and Research, 11*(2),pp. 133-144.

Pottier, T., Germain, G., Calamaz, M., Morel, A., & Coupard, D. (2014). Sub-millimeter measurement of finite strains at cutting tool tip vicinity. *Experimental Mechanics, 54*(6),pp. 1031-1042.

Priarone, P. C., Klocke, F., Faga, M. G., Lung, D., & Settineri, L. (2016). Tool life and surface integrity when turning titanium aluminides with PCD tools under conventional wet cutting and cryogenic cooling. *The International Journal of Advanced Manufacturing Technology, 85*(1),pp. 807-816.

Priarone, P. C., Rizzuti, S., Rotella, G., & Settineri, L. (2012a). Tool wear and surface quality in milling of a gamma-TiAl intermetallic. *The International Journal of Advanced Manufacturing Technology, 61*(1),pp. 25-33.

Priarone, P. C., Rizzuti, S., Settineri, L., & Vergnano, G. (2012b). Effects of cutting angle, edge preparation, and nano-structured coating on milling performance of a gamma titanium aluminide. *Journal of Materials Processing Technology, 212*(12),pp. 2619-2628.

Pu, Z., Outeiro, J. C., Batista, A. C., Dillon Jr, O. W., Puleo, D. A., & Jawahir, I. S. (2012). Enhanced surface integrity of AZ31B Mg alloy by cryogenic machining towards improved functional performance of machined components. *International Journal of Machine Tools and Manufacture, 56*(0),pp. 17-27.

Pujana, J., Arrazola, P., & Villar, J. (2008). In-process high-speed photography applied to orthogonal turning. *Journal of Materials Processing Technology, 202*(1-3),pp. 475-485.

Pusavec, F., Deshpande, A., Yang, S., M'Saoubi, R., Kopac, J., Dillon Jr, O. W., & Jawahir, I. S. (2014). Sustainable machining of high temperature Nickel alloy - Inconel 718: Part 1 - Predictive performance models. *Journal of Cleaner Production, 81*,pp. 255-269.

Radkowski, G., & Sep, J. (2014). Surface quality of a milled gamma titanium aluminide for aeronautical applications. *Management and Production Engineering Review, 5*(2),pp. 60-65.

Ramesh, A., & Melkote, S. N. (2008). Modeling of white layer formation under thermally dominant conditions in orthogonal machining of hardened AISI 52100 steel. *International Journal of Machine Tools and Manufacture, 48*(3-4),pp. 402-414.

Ranganath, S., Guo, C., & Hegde, P. (2009). A finite element modeling approach to predicting white layer formation in nickel superalloys. *CIRP annals, 58*(1),pp. 77-80.

Rao, B., Dandekar, C. R., & Shin, Y. C. (2011). An experimental and numerical study on the face milling of Ti–6Al–4V alloy: Tool performance and surface integrity. *Journal of Materials Processing Technology, 211*(2),pp. 294-304.

Ritto, T. G., & Rochinha, F. A. (2021). Digital twin, physics-based model, and machine learning applied to damage detection in structures. Mechanical Systems and Signal Processing, 155,p. 107614.

Rosenhain, W., & Sturney, A. (1925). Cutting Tools Research Committee. Report on Flow and Rupture of Metals during Cutting. *Proceedings of the Institution of Mechanical Engineers, 108*(1),pp. 141-174.

Rotella, G., & Umbrello, D. (2014). Finite element modeling of microstructural changes in dry and cryogenic cutting of Ti6Al4V alloy. *CIRP Annals - Manufacturing Technology, 63*(1),pp. 69-72.

Roth, R., & Oxley, P. L. B. (1972). Slip-line field analysis for orthogonal machining based upon experimental flow fields. *Journal of Mechanical Engineering Science, 14*(2),pp. 85-97.

Sadeghifar, M., Sedaghati, R., Jomaa, W., & Songmene, V. (2018). A comprehensive review of finite element modeling of orthogonal machining process: chip formation and surface integrity predictions. *The International Journal of Advanced Manufacturing Technology, 96*(9-12),pp. 3747-3791.

Salio, M., Berruti, T., & De Poli, G. (2006). Prediction of residual stress distribution after turning in turbine disks. *International Journal of Mechanical Sciences, 48*(9),pp. 976-984.

Schleich, B., Anwer, N., Mathieu, L., & Wartzack, S. (2017). Shaping the digital twin for design and production engineering. *CIRP annals, 66*(1),pp. 141-144.

Schoop, J. (2020). U.S. Patent Application No. 16/856,533.

Schoop, J. (2021). *In-Situ Calibrated Modeling of Residual Stresses Induced in Machining under Various Cooling and Lubricating Environments*. Lubricants, 9(3), p. 28.

Schoop, J., Adeniji, D., & Brown, I. (2019). Computationally efficient, multi-domain hybrid modeling of surface integrity in machining and related thermomechanical finishing processes. Procedia CIRP, 82, pp. 356-361.

Schoop, J. M. (2020). U.S. Patent Application No. 16/798,007.

Schwerd, F. (1935). Filmaufnahmen des Ablaufenden Spans bei Ueblichen und bei Selir Hohen Schnittgeschwindigkeiter. *Zeitschrift VDI, 80*,pp. 119.

Sharif, S., & Rahim, E. (2007). Performance of coated-and uncoated-carbide tools when drilling titanium alloy—Ti–6Al4V. *Journal of Materials Processing Technology, 185*(1-3),pp. 72-76.

Sharman, A., Aspinwall, D., Dewes, R., & Bowen, P. (2001a). Workpiece surface integrity considerations when finish turning gamma titanium aluminide. *Wear, 249*(5-6),pp. 473-481.

Sharman, A., Aspinwall, D., Dewes, R., Clifton, D., & Bowen, P. (2001b). The effects of machined workpiece surface integrity on the fatigue life of γ-titanium aluminide. *International Journal of Machine Tools and Manufacture, 41*(11),pp. 1681-1685.

Sharman, A., Hughes, J., & Ridgway, K. (2006). An analysis of the residual stresses generated in Inconel 718™ when turning. *Journal of Materials Processing Technology, 173*(3),pp. 359-367.

Sharman, A., Hughes, J., & Ridgway, K. (2015). The effect of tool nose radius on surface integrity and residual stresses when turning Inconel 718™. *Journal of Materials Processing Technology, 216*,pp. 123-132.

Shokrani, A., Dhokia, V., & Newman, S. T. (2012). *Study of the effects of cryogenic machining on the machinability of Ti-6Al-4V titanium alloy.* Paper presented at the 12th International Conference of the European Society for Precision Engineering and Nanotechnology, EUSPEN 2012, June 4, 2012 - June 7, 2012, Stockholm, Sweden,pp. 283-286.

Siebert, T., Becker, T., Splitthof, K., Neumann, I., & Krupka, R. (2007). High-speed digital image correlation: error estimations and applications. *Optical Engineering, 46*(5),pp. 051004.

Simoneau, A., Ng, E., & Elbestawi, M. (2007). Grain size and orientation effects when microcutting AISI 1045 steel. *CIRP Annals, 56*(1),pp. 57-60.

Sommer, A., & Keijzers, G. (2003). Gamma TiAl and the engine exhaust valve. *Gamma Titanium Aluminides 2003*,pp. 3-7.

Spaans, C. (1971). The fundamentals of three-dimensional chip curl, chip breaking and chip control. Ph.D. Dissertation, Delft University of Technology, Delft, South Holland, Netherlands.

Stevenson, M., & Oxley, P. (1969). An experimental investigation of the influence of speed and scale on the strain-rate in a zone of intense plastic deformation. *Proceedings of the Institution of Mechanical Engineers, 184*(1),pp. 561-576.

Su, H., Liu, P., Fu, Y., & Xu, J. (2012). Tool Life and Surface Integrity in High-speed Milling of Titanium Alloy TA15 with PCD/PCBN Tools. *Chinese Journal of Aeronautics, 25*(5),pp. 784-790.

Sun, Y., & Balk, T. J. (2008). Evolution of structure, composition, and stress in nanoporous gold thin films with grain-boundary cracks. *Metallurgical and Materials Transactions a-Physical Metallurgy and Materials Science, 39A*(11),pp. 2656-2665.

Sun, Y., Huang, B., Puleo, D. A., & Jawahir, I. S. (2015). Enhanced Machinability of Ti-5553 Alloy from Cryogenic Machining: Comparison with MQL and Flood-cooled Machining and Modeling. *Procedia CIRP, 31*,pp. 477-482.

Suprock, C. A. (2011). *Wireless Sensor Integrated Tool for Characterization of Machining Dynamics in Milling*. Ph.D. Dissertation, University of New Hampshire, Durham.

Suprock, C. A., Fussell, B. K., Hassan, R. Z., & Jerard, R. B. (2008). *A low cost wireless tool tip vibration sensor for milling.* Paper presented at the International Manufacturing Science and Engineering Conference, 48517,pp. 465-474.

Sutter, G., & List, G. (2013). Very high speed cutting of Ti–6Al–4V titanium alloy–change in morphology and mechanism of chip formation. *International Journal of Machine Tools and Manufacture, 66*,pp. 37-43.

Sutton, M., & Hild, F. (2015). Recent advances and perspectives in digital image correlation. *Experimental Mechanics, 55*(1),pp. 1-8.

Tao, F., Cheng, J., Qi, Q., Zhang, M., Zhang, H., & Sui, F. (2018). Digital twin-driven product design, manufacturing and service with big data. *The International Journal of Advanced Manufacturing Technology, 94*(9),pp. 3563-3576.

Tausendfreund, A., Stöbener, D., & Fischer, A. (2018). Precise in-process strain measurements for the investigation of surface modification mechanisms. *Journal of Manufacturing and Materials Processing, 2*(1),pp. 1-11.

Tausendfreund, A., Stöbener, D., & Fischer, A. (2020). In-process workpiece displacement measurements under the rough environments of manufacturing technology. *Procedia CIRP, 87*,pp. 409-414.

Terchi, A., & Au, Y. (2001). Acoustic emission signal processing. *Measurement and Control, 34*(8),pp. 240-244.

Thakur, A., & Gangopadhyay, S. (2016). State-of-the-art in surface integrity in machining of nickel-based super alloys. *International Journal of Machine Tools and Manufacture, 100*,pp. 25-54.

Thimm, B., Steden, J., Reuber, M., & Christ, H.-J. (2019). Using Digital Image Correlation Measurements for the Inverse Identification of Constitutive Material Parameters applied in Metal Cutting Simulations. *Procedia CIRP, 82*,pp. 95-100.

Tong, J. (2018). Full‑field characterisation of crack tip deformation and fatigue crack growth using digital image correlation—a review. *Fatigue & Fracture of Engineering Materials & Structures, 41*(9),pp. 1855-1869.

Tönshoff, H., & Brinksmeier, E. (1980). Determination of the mechanical and thermal influences on machined surfaces by microhardness and residual stress analysis. *CIRP Annals, 29*(2),pp. 519-530.

Topac, O. T., Gozluklu, B., Gurses, E., & Coker, D. (2017). Experimental and computational study of the damage process in CFRP composite beams under low-velocity impact. *Composites Part A: Applied Science and Manufacturing, 92*,pp. 167-182.

Tran, T., & Lundgren, J. (2020). Drill Fault Diagnosis Based on the Scalogram and Mel Spectrogram of Sound Signals Using Artificial Intelligence. *IEEE Access, 8*,pp. 203655-203666.

Treloar, G. J. (1997). Extracting embodied energy paths from input–output tables: towards an input–output-based hybrid energy analysis method. *Economic Systems Research, 9*(4),pp. 375-391.

Tung, S.-H., Shih, M.-H., & Kuo, J.-C. (2010). Application of digital image correlation for anisotropic plastic deformation during tension testing. *Optics and Lasers in Engineering, 48*(5),pp. 636-641.

Ucun, I., Aslantas, K., & Bedir, F. (2013). An experimental investigation of the effect of coating material on tool wear in micro milling of Inconel 718 super alloy. *Wear, 300*(1-2),pp. 8-19.

Uhlemann, T. H.-J., Lehmann, C., & Steinhilper, R. (2017). The digital twin: Realizing the cyber-physical production system for industry 4.0. *Procedia CIRP, 61*,pp. 335-340.

Uhlmann, E., Frommeyer, G., Herter, S., Knippscheer, S., & Lischka, J. (2004). *Studies on the Conventional Machining of TiAl-Based Alloys.* Paper presented at the Ti-2003, 10th World Conference on Titanium,pp. 2293-2300.

Uhlmann, E., Herter, S., Gerstenberger, R., & Roeder, M. (2009). Quasi-static chip formation of intermetallic titanium aluminides. *Production Engineering, 3*(3),pp. 261-270.

Ulsoy, A. G., & Koren, Y. (1993). Control of machining processes. ASME Journal of Dynamic Systems, Measurement and Control, Special 50th Anniversary Issue, Vol. 115, No. 2(B), pp. 301-308.

Ulutan, D., Alaca, B. E., & Lazoglu, I. (2007). Analytical modelling of residual stresses in machining. *Journal of Materials Processing Technology, 183*(1),pp. 77-87.

Umbrello, D., & Filice, L. (2009). Improving surface integrity in orthogonal machining of hardened AISI 52100 steel by modeling white and dark layers formation. *CIRP Annals - Manufacturing Technology, 58*(1),pp. 73-76.

Umbrello, D., Hua, J., & Shivpuri, R. (2004). Hardness-based flow stress and fracture models for numerical simulation of hard machining AISI 52100 bearing steel. *Materials Science and Engineering: A, 374*(1-2),pp. 90-100.

Umbrello, D., Micari, F., & Jawahir, I. S. (2012). The effects of cryogenic cooling on surface integrity in hard machining: A comparison with dry machining. *CIRP Annals - Manufacturing Technology, 61*(1),pp. 103-106.

Umbrello, D., Pu, Z., Caruso, S., Outeiro, J. C., Jayal, A. D., Dillon Jr, O. W., & Jawahir, I. S. (2011). The effects of cryogenic cooling on surface integrity in hard machining. *Procedia Engineering, 19*,pp. 371-376.

Venkatachalam, S., Khaja Mohiddin, S., & Murthy, H. (2018). Determination of damage evolution in CFRP subjected to cyclic loading using DIC. *Fatigue & Fracture of Engineering Materials & Structures, 41*(6),pp. 1412-1425.

Venugopal, K., Tawade, R., Prashanth, P., Paul, S., & Chattopadhyay, A. (2003). Turning of titanium alloy with TiB2-coated carbides under cryogenic cooling. *Proceedings of the Institution of Mechanical Engineers, Part B: Journal of Engineering Manufacture, 217*(12),pp. 1697-1707.

Wang, W., Mottershead, J. E., Siebert, T., & Pipino, A. (2012a). Frequency response functions of shape features from full-field vibration measurements using digital image correlation. *Mechanical Systems and Signal Processing, 28*,pp. 333-347.

Wang, X., Da, Z., Balaji, A., & Jawahir, I. (2007). Performance-based predictive models and optimization methods for turning operations and applications: Part 3—optimum cutting conditions and selection of cutting tools. *Journal of Manufacturing Processes, 9*(1),pp. 61-74.

Wang, Y., Jiang, J., Wanintrudal, C., Du, C., Zhou, D., Smith, L., & Yang, L. (2010). Whole field sheet‑metal tensile test using digital image correlation. *Experimental Techniques, 34*(2),pp. 54-59.

Wang, Y., Lava, P., Coppieters, S., De Strycker, M., Van Houtte, P., & Debruyne, D. (2012b). Investigation of the uncertainty of DIC under heterogeneous strain states with numerical tests. *Strain, 48*(6),pp. 453-462.

Wanigarathne, P., Kardekar, A., Dillon, O., Poulachon, G., & Jawahir, I. (2005). Progressive tool-wear in machining with coated grooved tools and its correlation with cutting temperature. *Wear, 259*(7-12),pp. 1215-1224.

Wattrisse, B., Chrysochoos, A., Muracciole, J.-M., & Némoz-Gaillard, M. (2001). Analysis of strain localization during tensile tests by digital image correlation. *Experimental Mechanics, 41*(1),pp. 29-39.

Williams, J., Smart, E., & Milner, D. (1970). Metallurgy of machining. Pt. 1. Basic considerations and the cutting of pure metals. *Metallurgia, 81*(483),pp. 3-10.

Wu, D., & Matsumoto, Y. (1990). The effect of hardness on residual stresses in orthogonal machining of AISI 4340 steel. *ASME Journal of Manufacturing Science and Engineering, 112*,pp. 245-252

Wu, X., Liu, Y., Zhou, X., & Mou, A. (2019). Automatic Identification of Tool Wear Based on Convolutional Neural Network in Face Milling Process. *Sensors (Basel), 19*(18),p. 3817.

Xie, Z., Lu, Y., & Chen, X. (2020). A multi-sensor integrated smart tool holder for cutting process monitoring. *The International Journal of Advanced Manufacturing Technology, 110*(3),pp. 853-864.

Xiong, Y., Wang, W., Jiang, R., Lin, K., & Song, G. (2016). Tool wear mechanisms for milling in situ TiB2 particle-reinforced Al matrix composites. *The International Journal of Advanced Manufacturing Technology, 86*(9),pp. 3517-3526.

Yang, X., & Liu, C. R. (2002). A new stress-based model of friction behavior in machining and its significant impact on residual stresses computed by finite element method. *International Journal of Mechanical Sciences, 44*(4),pp. 703-723.

Zappa, E., Mazzoleni, P., & Matinmanesh, A. (2014). Uncertainty assessment of digital image correlation method in dynamic applications. *Optics and Lasers in Engineering, 56*,pp. 140-151.

Zhang, C. (2019). *Quantitative kinematic and thermal full fields measurement.* (Doctoral dissertation, Université de Lyon).

Zhang, D., Zhang, X.-M., & Ding, H. (2018a). Hybrid digital image correlation–finite element modeling approach for modeling of orthogonal cutting process. *Journal of Manufacturing Science and Engineering, 140*(4),p. 040118.

Zhang, D., Zhang, X.-M., & Ding, H. (2018b). Inverse identification of material plastic constitutive parameters based on the DIC determined workpiece deformation fields in orthogonal cutting. *Procedia CIRP, 71*,pp. 134-139.

Zhang, D., Zhang, X.-M., Nie, G.-C., Yang, Z.-Y., & Ding, H. (2021). Characterization of material strain and thermal softening effects in the cutting process. *International Journal of Machine Tools and Manufacture, 160*,pp. 103672.

Zhang, D., Zhang, X.-M., Xu, W.-J., & Ding, H. (2017). Stress field analysis in orthogonal cutting process using digital image correlation technique. *Journal of Manufacturing Science and Engineering, 139*(3),p. 031001.

Zhang, S., Li, J., Sun, J., & Jiang, F. (2010). Tool wear and cutting forces variation in high-speed end-milling Ti-6Al-4V alloy. *The International Journal of Advanced Manufacturing Technology, 46*(1-4),pp. 69-78.

Zhang, S., Li, J., & Wang, Y. (2012). Tool life and cutting forces in end milling Inconel 718 under dry and minimum quantity cooling lubrication cutting conditions. *Journal of Cleaner Production, 32*,pp. 81-87.

Zhang, W., Reddy, B., & Deevi, S. (2001). Physical properties of TiAl-base alloys. *Scripta Materialia, 45*(6),pp. 645-651.

Zhang, X.-M., Zhang, K., Zhang, D., Outeiro, J., & Ding, H. (2019). New In Situ Imaging-Based Methodology to Identify the Material Constitutive Model Coefficients in Metal Cutting Process. *Journal of Manufacturing Science and Engineering, 141*(10),p. 101007.

Zhou, J., Bushlya, V., Peng, R. L., Johansson, S., Avdovic, P., & Stahl, J. (2011). Effects of tool wear on subsurface deformation of nickel-based superalloy. *Procedia Engineering, 19*,pp. 407-413.

Zouabi, H., Calamaz, M., Wagner, V., Cahuc, O., & Dessein, G. (2021). Kinematic Fields Measurement during Orthogonal Cutting Using Digital Images Correlation: A Review. *Journal of Manufacturing and Materials Processing, 5*(1),p. 7.

VITA

David Adeniji was born in Ibadan, Oyo State, Nigeria. He completed his high school in 2008 at African Church Grammar School, Apata, Ibadan. He gained admission to pursue a Bachelor of Engineering in Mechanical Engineering at the Federal University of Agriculture, Abeokuta and graduated in January 2014. Following his graduation in 2014, David garnered professional experience from engineering firms in Nigeria: Mikano International, Richardson Oil and Gas Limited, and Flour Mills of Nigeria Plc between September 2015 and August 2018.

He moved to the United States in August 2018 to pursue a Ph.D. in Mechanical Engineering at the University of Kentucky (Institute for Sustainable Manufacturing) in Lexington, KY, USA. He later joined Dr. Julius Schoop's lab. in December 2018. Under the mentorship of Dr. Schoop, David was published five (5) times and interned at Intel Corporation (Chandler, AZ Campus) as a Test R&D Mechanical Engineer in the summer of 2021. He will be re-joining the Test Tooling Team by June 2022.

PUBLICATIONS

1. Adeniji, David, Kyle Oligee, and Julius Schoop. *"A Novel Approach for Real-Time Quality Monitoring in Machining of Aerospace Alloy through Acoustic Emission Signal Transformation for DNN."* Journal of Manufacturing and Materials Processing 6, no. 1 (2022): 18.
2. Adeniji, David, and Julius Schoop. *"In-Situ Calibrated Digital Process Twin Models for Resource Efficient Manufacturing."* Journal of Manufacturing Science and Engineering 144, no. 4 (2022).
3. Schoop, Julius, Hasan A. Poonawala, David Adeniji, and Benton Clark. *"AI-enabled dynamic finish machining optimization for sustained surface integrity."* Manufacturing Letters 29 (2021): 42-46.
4. Adeniji, David, Julius Schoop, Shehan Gunawardena, Craig Hanson, and Muhammad Jahan. *"Characterization and modeling of surface roughness and burr formation in slot milling of polycarbonate."* Journal of Manufacturing and Materials Processing 4, no. 2 (2020): 59.
5. Schoop, Julius, David Adeniji, and Ian Brown. *"Computationally efficient, multi-domain hybrid modeling of surface integrity in machining and related thermomechanical finishing processes."* Procedia CIRP 82 (2019): 356-361.